INVESTIGATIONS OF THE ELECTROCALORIC EFFECT IN THE POLYCRYSTALLINE $0.9Pb(Mg_{1/3}Nb_{2/3})O_3$-$0.1PbTiO_3$ RELAXOR FERROELECTRIC

Marko Vrabelj

Doctoral Dissertation
Jožef Stefan International Postgraduate School
Ljubljana, Slovenia

Supervisor: Prof. Dr. Barbara Malič, Electronic Ceramics Department – K5, Jožef Stefan Institute, Jamova cesta 39, 1000 Ljubljana, Slovenia

Co-Supervisor: Prof. Dr. Zdravko Kutnjak, Condensed Matter Physics – F5, Jožef Stefan Institute, Jamova cesta 39, 1000 Ljubljana, Slovenia

Evaluation Board:

Assoc. Prof. Dr. Tadej Rojac, Chair, Electronic Ceramics Department – K5, Jožef Stefan Institute, Jamova cesta 39, 1000 Ljubljana, Slovenia

Prof. Dr. Matjaž Valant, Member, Materials Research Laboratory, University of Nova Gorica, Vipavska 13, 5000 Nova Gorica

Assoc. Prof. Dr. Klaus Reichmann, Member, Institute for Chemistry and Technology of Materials, Graz University of Technology, Stremayrgasse 9, 8010 Graz, Austria

MEDNARODNA PODIPLOMSKA ŠOLA JOŽEFA STEFANA
JOŽEF STEFAN INTERNATIONAL POSTGRADUATE SCHOOL



Marko Vrabelj

INVESTIGATIONS OF THE ELECTROCALORIC EFFECT IN THE POLYCRYSTALLINE $0.9Pb(Mg_{1/3}Nb_{2/3})O_3$-$0.1PbTiO_3$ RELAXOR FERROELECTRIC

Doctoral Dissertation

RAZISKAVE ELEKTROKALORIČNEGA POJAVA V POLIKRISTALINIČNEM RELAKSORSKEM FEROELEKTRIKU $0{,}9Pb(Mg_{1/3}Nb_{2/3})O_3$-$0{,}1PbTiO_3$

Doktorska disertacija

Supervisor: Prof. Dr. Barbara Malič

Co-Supervisor: Prof. Dr. Zdravko Kutnjak

Ljubljana, Slovenia, June 2016

To all who inspired me and encouraged me to go my own way. . .

Acknowledgments

This work would not have been possible without the support of many people, who helped me over the years.

First and foremost, I would like to thank to Prof. Dr. Barbara Malič for her guidance, support, patience, enthusiasm, and for numerous suggestions and scientific discussions. She far exceeded all her duties as my research mentor and enabled me to learn a lot in these three and a half years.

I would like to acknowledge Prof. Dr. Barbara Malič and the late Prof. Dr. Marija Kosec for accepting me in the Electronic Ceramics Department – K5 at the Jožef Stefan institute already as an undergraduate student.

I would like to thank to Prof. Dr. Zdravko Kutnjak, my co-mentor, for numerous pieces of advice and discussions related to electrocaloric materials and measurements. I am also grateful to him for allowing me to use all the equipment in the ″electrocaloric lab″ at Condensed Matter Physics Department – F5 at the Jožef Stefan institute.

My special thanks go to all my co-workers from the Electronic Ceramics Department, especially to Silvo Drnovšek for teaching me the ″lab-skills″ and for help during the experiments, Dr. Hana Uršič for support and helping me to write the seminars and scientific papers, Jena Cilenšek for different experiments, Brigita Kmet for support with the SEM and the sample preparation for TEM, Lovro Fulanović for the support with the dielectric measurements, Assist. Prof. Dr. Andreja Benčan for the TEM analyses, Assist. Prof. Dr. Tadej Rojac, Dr. Katarina Vojisavljević, and Dr. Jurij Koruza for answering all kinds of questions and to the student Kristijan Kuhar who helped me with the laboratory work.

My special thanks are extended to Dr. Julian Walker, my office-mate for most of the time, for all the scientific discussions, grammar corrections, advice and jokes that made my PhD study easier and more pleasant.

In addition I would like to thank to Dr. Brigita Rožič, Maja Trček and Dr. Georgios Kordogiannis, the electrocaloric group from F5, for their support during the direct electrocaloric measurements. All the measurements would be trickier without you. Special thanks go to Dr. Brigita Rožič, who taught me how to use the high-resolution calorimeter.

Assoc. Prof. Dr. Vid Bobnar is acknowledged for the support with the dielectric spectroscopy and for all the dielectric-related advice.

I would like to thank to Uroš Plaznik and his advisor Assoc. Prof. Dr. Andrej Kitanovski from the University of Ljubljana, Faculty of Mechanical Engineering for their collaboration and for proving that our EC materials are truly useful in applications ☺. Special thanks go to Uroš for numerous discussions related to electrocalorics during the work as well as in our free time.

I would also like to thank Maja Koblar from the Center of Electron Microscopy and Microanalysis at the Jožef Stefan institute for the advice related to the SEM and WDXS analysis.

I would like to thank to Dr. Sebastjan Glinšek for helping me to solve the problems with the dielectric spectroscopy.

I am also taking this opportunity to express my gratitude to the Slovenian Research Agency for funding and to the Centre of Excellence NAMASTE for enabling the use of laboratory equipment.

Most importantly, I thank my girlfriend Tanja for her love, support and for all the patience during my PhD, and to my parents, brother, his girlfriend, and to all my friends, who unconditionally supported me all these years.

Abstract

The electrocaloric (EC) effect is the change in entropy and, consequently, in temperature of a dielectric material due to the electric-field-induced changes in the polar states. The (1-x)$Pb(Mg_{1/3}Nb_{2/3})O_3$-x$PbTiO_3$ (PMN-100xPT) solid solution with x≤0.35 has been widely studied for its excellent dielectric and piezoelectric properties, and recent studies have also shown that the compositions exhibiting the dielectric permittivity maximum close to room temperature, such as PMN-10PT, exhibit a great potential for EC applications. Although it has been generally accepted that the microstructure crucially influences the dielectric properties of ferroelectric and relaxor ferroelectric ceramics, the correlations between the microstructure and EC phenomena have not yet been explored.

We show that a substantial enhancement of the EC effect is achieved by a properly engineered ceramic microstructure. Single-phase perovskite ceramic materials with relative densities exceeding 95 % and with grain sizes ranging from 2.8 µm to 9.4 µm were prepared by sintering of mechanochemically synthesized powder compacts. The largest EC coefficient, i.e., the ratio of the EC temperature change (ΔT_{EC}) and electric field amplitude, is obtained for the ceramics with 5.8-µm grains, i.e., a more than 10 % higher value than for the materials with finer or coarser grains, as a consequence of its larger saturation polarization. The EC response of a material is limited by its dielectric breakdown strength, which increases with an increasing density and decreasing grain size.

For the material with an ~98 % relative density and 3.6-µm grains, the ΔT_{EC} of 3.45 °C is achieved at an electric field amplitude of 160 kV/cm. This ΔT_{EC} is the highest reported so far for Pb-based perovskites and it is comparable to the best results obtained by multi-critical-point enhancement.

The PMN-10PT ceramics with similar densities and grain sizes of ~5 µm prepared from the powders obtained by the mechanochemical and columbite synthesis routes are compared. Despite the very similar EC coefficients, the mechanochemically derived ceramic displays a much larger ΔT_{EC} of 2.37 °C than the columbite-derived ceramic (1.39 °C) due to the higher dielectric breakdown strength (115 kV/cm vs. 57 kV/cm). The difference is ascribed to different levels of chemical homogeneity and trace contaminants introduced during the powder synthesis, which are reflected in the different domain sizes and dielectric properties of the respective materials.

In the last part we analyze the energy-efficiency of an EC cooling system in view of the polarization – electric field ($P-E$) hysteresis losses of the EC materials, and recovering the electric energy that is consumed for inducing the EC effect (electric-energy recovery). The energy efficiency of the materials with large hysteresis losses, i.e., PMN-100xPT compositions close to the morphotropic phase boundary, is significantly reduced as compared to the PMN-rich relaxor compositions. Therefore, we propose that the EC materials with low $P-E$ hysteresis losses, such as PMN-100xPT with x≤0.1, and a high-degree of the electric-energy recovery should be implemented in an EC cooling system in order to achieve a high energy efficiency.

Povzetek

Elektrokalorični (EK) pojav je pretvorba električne energije v toploto in je definiran kot sprememba temperature zaradi spremembe dipolarnih stanj v materialu pod vplivom zunanjega električnega polja. Kompleksni perovskiti (1-x)Pb($Mg_{1/3}Nb_{2/3}$)O_3-x$PbTiO_3$ (PMN-100xPT) s sestavo x≤0,35 predstavljajo skupino materialov z odličnimi dielektričnimi in piezoelektričnimi lastnostmi, v zadnjem času pa se je izkazalo, da imajo sestave z vrhom dielektričnosti blizu sobne temperature, kot na primer PMN-10PT, dobre EK lastnosti. Čeprav je znano, da mikrostruktura kritično vpliva na dielektrične lastnosti feroelektrične in relaksorsko-feroelektrične keramike, povezave med mikrostrukturo in EK pojavom še niso bile raziskane.

V okviru doktorske disertacije smo pokazali, da lahko z načrtovanjem mikrostrukture občutno povečamo EK odziv keramike PMN-10PT. Pripravili smo volumensko keramiko z relativno gostoto nad 95 % in povprečno velikostjo zrn od 2,8 µm do 9,4 µm s sintranjem vzorcev, pripravljenih z mehanokemijsko sintezo. Keramika s 5,8 µm zrni izkazuje največji EK koeficient, to je razmerje med EK spremembo temperature (ΔT_{EC}) in amplitudo električnega polja. Slednji je za 10 % večji kot pri fino- in grobozrnati keramiki, kar pripisujemo najvišji nasičeni polarizaciji vzorca s 5,8 µm zrni. EK odziv materiala je omejen s prebojno trdnostjo, ki narašča z naraščajočo gostoto in s padajočo velikostjo zrn. V keramiki s ~98 % relativno gostoto in 3,6 mikronskimi zrni smo dosegli ΔT_{EC} 3,45 °C pri amplitudi električnega polja 160 kV/cm. To je do sedaj največja objavljena vrednost v vseh svinčevih perovskitih in je bila dosežena daleč od multikritične točke.

Keramiko PMN-10PT z relativno gostoto ≥96% in velikostjo zrn ~5 µm smo pripravili s sintranjem vzorcev, pripravljenih z mehanokemijsko in s kolumbitno sintezo. Oba materiala sta izkazovala podobna EK koeficienta, vendar je mehanokemijsko pripravljena keramika dosegla veliko večjo ΔT_{EC} kot material, pripravljen po kolumbitnem postopku, kot posledica večje dielektrične prebojne trdnosti: 2,37 °C pri polju 115 kV/cm v primerjavi z 1,39 °C pri polju 57 kV/cm. Razliko pripisujemo različnim stopnjam kemijske homogenosti ter možnemu vplivu nečistoč, ki so neizogibna posledica priprave keramike, kar se odraža v različnih velikostih domen in dielektričnih lastnostih obeh materialov.

Analizirali smo energijsko učinkovitost EK hladilnega sistema, pri čemer smo se osredotočili na vpliv regeneracije električne energije in histereznih izgub, ki jih izkazujejo obravnavani EK materiali. Energijska učinkovitost materiala z velikimi histereznimi izgubami, v našem primeru trdnih raztopin v bližini morfotropne fazne meje, kot PMN-35PT, je izrazito manjša od relaksorskih sestav, bogatih na PMN. Na osnovi analiz smo pokazali, da EK material z nizkimi histereznimi izgubami, na primer PMN-100xPT z x≤0,1, in z visoko stopnjo regeneracije električne energije predstavlja osnovo za učinkovit EK hladilni sistem.

Contents

List of Figures **xvii**

List of Tables **xxi**

Abbreviations **xxiii**

Symbols **xxv**

1 Introduction **1**
1.1 Polar Oxides ... 1
1.1.1 Dielectric Polarization ... 1
1.1.2 Ferroelectric Materials ... 2
1.1.3 Relaxor Ferroelectric Materials ... 3
1.2 Electrocaloric Effect ... 5
1.2.1 Thermodynamics of the Electrocaloric Effect ... 6
1.2.2 Electrocaloric Cycle ... 7
1.2.3 Measuring the Electrocaloric Effect ... 8
1.2.3.1 Indirect EC Measurements Using Thermodynamic Approach ... 8
1.2.3.2 Direct Measurements of the EC Effect Using High-Resolution Calorimetry ... 9
1.2.4 Importance of the Dielectric Breakdown Strength in Electrocaloric Materials ... 10
1.2.5 Energy Efficiency of Electrocaloric Materials ... 11
1.3 (1-x)Pb($Mg_{1/3}Nb_{2/3}$)O_3-x$PbTiO_3$ Solid Solution ... 13
1.3.1 Phase Diagram ... 13
1.3.2 Role of the Grain Size and Chemical Homogeneity of (1-x)Pb($Mg_{1/3}Nb_{2/3}$)O_3-x$PbTiO_3$ Ceramics ... 14
1.3.3 Synthesis of the (1-x)Pb($Mg_{1/3}Nb_{2/3}$)O_3-x$PbTiO_3$ Ceramics ... 17
1.3.3.1 Columbite Synthesis ... 17
1.3.3.2 Mechanochemical Synthesis ... 17
1.4 Electrocaloric Effect in (1-x)Pb($Mg_{1/3}Nb_{2/3}$)O_3-x$PbTiO_3$ Perovskite Ceramics ... 19

2 Aims and Hypothesis **25**

3 Materials and Methods **27**
3.1 Sample Preparation ... 27
3.1.1 Synthesis of the 0.9Pb($Mg_{1/3}Nb_{2/3}$)O_3-0.1$PbTiO_3$ Powders ... 27
3.1.1.1 Mechanochemical Synthesis of PMN-10PT ... 28
3.1.1.2 Columbite Synthesis of PMN-10PT ... 28
3.1.2 Sintering and Preparation for the Electrical Measurements ... 29
3.2 Characterization Methods ... 30
3.2.1 Thermogravimetric Analysis ... 30

3.2.2 Particle Size and Particle Size Distribution Analysis 30
3.2.3 X-Ray Diffraction 30
3.2.4 Inductively Coupled Plasma Spectroscopy 30
3.2.5 Dynamic Sintering Curves 30
3.2.6 Specific Heat Capacity 31
3.2.7 Density Measurements 31
3.2.8 Microstructural Analysis 31
3.2.9 Dielectric Spectroscopy 32
3.2.10 Domain Structure Investigations 32
3.2.11 Electrocaloric Measurements 32
3.2.11.1 Indirect Electrocaloric Measurements 32
3.2.11.2 Direct Electrocaloric Measurements 33
3.2.12 Study of the Energy Efficiency of the EC Cooling System Employing the $xPb(Mg_{1/3}Nb_{2/3})O_3$-(1-x)$PbTiO_3$ Ceramics 34

4 Results and Discussion 35
4.1 Electrocaloric Response of the Mechanochemically Synthesized $0.9Pb(Mg_{1/3}Nb_{2/3})O_3$-$0.1PbTiO_3$ Ceramics with Different Grain Sizes 35
4.1.1 Phase Composition and Microstructure 35
4.1.2 Dielectric Properties 40
4.1.3 Electrocaloric Properties 42
4.1.4 Summary 47
4.2 Electrocaloric Properties of $0.9Pb(Mg_{1/3}Nb_{2/3})O_3$-$0.1PbTiO_3$ Ceramics Prepared by Columbite Synthesis 48
4.2.1 Phase Composition and Microstructure 48
4.2.2 Dielectric Properties 51
4.2.3 Electrocaloric Properties 52
4.2.4 Summary 54
4.3 Comparison of the $0.9Pb(Mg_{1/3}Nb_{2/3})O_3$-$0.1PbTiO_3$ Ceramics, Prepared by Mechanochemical and Columbite Synthesis 55
4.3.1 Powders and Ceramics 55
4.3.2 Dielectric and EC Properties 58
4.3.3 Summary 63
4.4 Energy Efficiency of an Electrocaloric Cooling System with (1-x)$Pb(Mg_{1/3}Nb_{2/3})O_3$-x$PbTiO_3$ Ceramics 64
4.4.1 Electrocaloric Material in a Thermodynamic Cycle 64
4.4.2 Energy Efficiency of the EC Cooling System Employing PMN-100xPT (x=0, 0.1 and 0.35) 68
4.4.3 Summary 71

5 Summary, Conclusions and Outlook 73

Appendix A Dielectric Breakdown Phenomena 77
A.1 Dielectric Breakdown Experiment 77
A.2 Mechanisms of Dielectric Breakdown Phenomena 78
A.2.1 Intrinsic Breakdown 78
A.2.2 Thermal Breakdown 79
A.2.3 Discharge Breakdown 79
A.3 Factors Affecting Dielectric Breakdown Strength 79
A.3.1 Influence of the Microstructure on the Dielectric Breakdown Strength .. 79

A.3.1.1 Influence of the Grain Size on the Dielectric Breakdown Strength....80
A.3.1.2 Influence of the Porosity on the Dielectric Breakdown Strength 80
A.3.1.3 Influence of the Sample Geometry on the Dielectric Breakdown Strength....81
A.3.1.4 Influence of the Working Temperature on the Dielectric Breakdown Strength....82

Appendix B Specific Heat Capacity of the PMN-100xPT Ceramics 85

References 87

Bibliography 97

Biography 101

List of Figures

Figure 1.1: Unit cell of (a) cubic and (b) tetragonal ABO_3 structure 2
Figure 1.2: (a) The $P-E$ hysteresis loop of a $BaTiO_3$ single crystal, measured at room temperature (T_{room}) [6] and (b) the temperature dependence of ε' of $BaTiO_3$ ceramics with an average grain size of 13 µm 3
Figure 1.3: (a) the $P-E$ hysteresis loop at 1 kHz and (b) temperature dependence of ε' of PMN ceramics 4
Figure 1.4: Phase diagram of the PMN single crystal 5
Figure 1.5: Schematic presentation of the EC cycle 7
Figure 1.6: (a) $P-E$ hysteresis loops obtained at different temperatures. (b) Temperature dependence of the indirectly determined ΔT_{EC} at different electric fields 8
Figure 1.7: Schematic representation of the EC measurements 9
Figure 1.8: Dielectric breakdown strength E_b vs. dielectric premittivity ε' for different materials 10
Figure 1.9: EC efficiency η as a function of the absorbed Q for some ceramic and polymer thin films 12
Figure 1.10: Temperature dependence of the dielectric permittivity ε' for different PMN-PT compositions 13
Figure 1.11: Phase diagram of the PMN-PT system 14
Figure 1.12: The grain-size dependence of the dielectric permittivity ε' as a function of temperature 15
Figure 1.13: The $P-E$ hysteresis loops of the PMN-35PT ceramics 16
Figure 1.14: Quantities of individual phases as a function of the milling time for a powder mixture with a stoichiometry corresponding to PMN 18
Figure 1.15: The EC temperature change ΔT_{EC} vs. E and T for (a, b) PMN and (c, d) PMN-30PT ceramics 23
Figure 3.1: The FE-SEM images of the constituent oxides used for the PMN-10PT synthesis 28
Figure 3.2: Schematic presentation of the (a) mechanochemical and (b) columbite synthesis 29
Figure 3.3: (a) Schematic representation of the prepared sample for direct EC measurements. (b) Mounted sample in the calorimeter's head. 33
Figure 3.4: Applied electric signal during the $P(E)$ measurements of PMN-PT ceramics 34
Figure 4.1: XRD pattern of the PMN-10PT powder after 96 h of high-energy milling 35
Figure 4.2: (a) FE-SEM micrograph and (b) particle size distribution of the PMN-10PT powder, prepared by mechanochemical synthesis, after attrition milling 36
Figure 4.3: Dynamic sintering curve of the mechanochemically synthesized PMN-10PT powder compact 37

Figure 4.4: (a) XRD patterns and (b) relative densities (RD) of the sintered PMN-10PT ceramics, prepared from the mechanochemically synthesized powder 37
Figure 4.5: FE-SEM micrographs of the polished (left) and thermally etched (middle) surfaces together with the grain-size distributions and cumulative curves (right) of the PMN-10PT ceramics sintered at selected temperatures and times. 38
Figure 4.6: HR-TEM images of a grain boundary (GB) for the ceramics with an average grain size of (a) 3.6 µm and (b) 9.4 µm..... 39
Figure 4.7: Dielectric permittivity ε' at 1 kHz as a function of temperature for the PMN-10PT ceramics 40
Figure 4.8: Temperature dependence of ε' and $tan\delta$ for PMN-10PT ceramics with an average grain size of 3.6 µm 41
Figure 4.9: (a) The $P-E$ hysteresis loops of the PMN-10PT ceramics with average grain size of 5.8 µm, measured at 1 Hz within the temperature interval from 40 °C to 130 °C with a step of 5 °C. (b-e) Intermediate results of the indirect EC evaluation, extracted from the $P-E$ hysteresis loops, from which the final (e) ΔT_{EC} as a function of temperature at selected electric field amplitudes is calculated. 42
Figure 4.10: (a-e) The ΔT_{EC} of the PMN-10PT ceramics sintered at (a) 1150 °C for 2 h, (b) 1200 °C for 2 h, (c) 1200 °C for 16 h, (d) 1250 °C for 8 h and (e) 1250 °C for 16 h 44
Figure 4.11: The ε' at the applied dc electric field of 25 kV/cm and at 1 kHz and ΔT_{EC} at 28 kV/cm as a function of temperature for the 3.6-µm-grain-sized sample 45
Figure 4.12: (a) The ΔT_{EC} and (b) $\Delta T_{EC}/E$ (solid stars) and P_s (open circles) vs. the average grain size of the PMN-10PT ceramics 46
Figure 4.13: The XRD pattern of the columbite precursor after calcination..... 48
Figure 4.14: XRD pattern (red line) of the PMN-10PT powder after the second calcination step..... 49
Figure 4.15: (a) FE-SEM micrographs and (b) particle size distribution of the PMN-10PT powder, prepared by the columbite synthesis..... 49
Figure 4.16: (a) Dynamic sintering curve of the PMN-10PT powder compact. 50
Figure 4.17: FE-SEM micrographs of the (a) polished and (b) thermally etched surfaces..... 50
Figure 4.18: Temperature dependence of the ε' and $tan\delta$ at 0.1, 1, and 10 kHz for different applied dc electric fields of the columbite-derived PMN-10PT ceramics..... 52
Figure 4.19: (a) The $P-E$ hysteresis loops of the PMN-10PT ceramics, prepared by columbite synthesis, and with an average grain size of 5.0 µm. 52
Figure 4.20: The ΔT_{EC} of the PMN-10PT ceramics (GS = 5.0 µm), prepared by the columbite synthesis 53
Figure 4.21: The XRD patterns of the Mech (blue) and Col (red) powders 55
Figure 4.22: (a) The particle size distributions and (b) the dynamic sintering curves of the Mech (blue) and Col (red) powders..... 56
Figure 4.23: The FE-SEM micrographs of the thermally etched surfaces for (a) Mech and (b) Col ceramics with comparable grain sizes. 56
Figure 4.24: Deviation of the concentration for individual elements with regard to their average concentrations 57
Figure 4.25: Temperature dependence of the ε' at 0.1, 1, and 10 kHz for the Mech (blue circles) and Col (red stars) ceramics 58

Figure 4.26: The polarization-electric field hysteresis loops for the Mech (blue line) and Col (red line) ceramics.....59
Figure 4.27: The topography images (above) and the out-of-plane amplitude PFM images (below) of the as-sintered Mech and Col ceramics.....60
Figure 4.28: The out-of-plane amplitude PFM images, before and after poling for the (a) Mech and (b) Col ceramics.....61
Figure 4.29: The $\Delta T_{EC}(T)$ at a few selected electric fields for the Mech and Col ceramics.....62
Figure 4.30: Schematic representation of a simple EC cooling system.....64
Figure 4.31: Schematic representation of the thermodynamic cycle to which the EC material is subjected in the EC cooling system.....65
Figure 4.32: The $P-E$ hysteresis loops for the PMN, PMN-10PT and PMN-35PT ceramics.....68
Figure 4.33: $P-E$ curves for the PMN, PMN-10PT and PMN-35PT ceramics.....69
Figure 4.34: The exergy efficiency ξ of the system under investigation.....70
Figure 5.1: The measured ΔT_{EC} versus electric field amplitude.....74

Figure A.1: Typical current-voltage characteristics of dielectric materials.....77
Figure A.2: (a) PMN-10PT ceramics partially covered with Cr/Au electrodes after breakdown at 115 kV/cm. (b) Surface and (c) cross section of the crater in the PMN-10PT material after dielectric breakdown.....78
Figure A.3: The average grain size (GS) vs. dielectric breakdown strength E_b for $BaTiO_3$ ceramics.....80
Figure A.4: (a) The effect of the amount of pores on E_b for PZT ceramics.....81
Figure A.5: (a) Dielectric breakdown strength E_b and breakdown voltage V_b vs. thickness d for PZT ceramics.....81
Figure A.6: Cross-sections of disk specimens for measurements of the dielectric strength;.....82
Figure A.7: Thickness dependence of the dielectric breakdown strength for $BaTiO_3$ ceramics.....82
Figure B.1: The temperature dependence of the specific heat capacity c_E of the PMN-100xPT (x = 0, 0.1 and 0.35) ceramics.....85

List of Tables

Table 1.1: Microstructure and dielectric properties of the hot-pressed PMN-35PT samples (HP; at 950 °C) and the samples subsequently annealed at 1150 °C.....15
Table 1.2: Some reported EC data for PMN-PT bulk ceramics. 20
Table 1.3: Some reported EC data for PMN-PT thick films. 21
Table 1.4: Some reported EC data for PMN-PT thin films.....21
Table 3.1: Chemicals used during the synthesis of the PMN-10PT powders.....27
Table 3.2: The particle sizes of consituent oxides used for the PMN-10PT synthesis. ...27
Table 4.1: Concentrations of contaminants in the PMN-10PT powder due to the wear of the milling bodies, determined by the ICP spectrometry.....36
Table 4.2: Chemical composition with the standard deviation (STDEV) of the PMN-10PT ceramics with the average grain sizes of 3.6 µm and 9.4 µm.....40
Table 4.3: Summary of the relevant findings presented in the current section.....47
Table 4.4: Chemical composition with the standard deviation (STDEV) of the PMN-10PT ceramics with the average grain sizes of 5.0 µm ± 2.6 µm obtained by WDXS. 51
Table 4.5: Summary of the relevant findings presented in the current section.....54
Table 4.6: Chemical composition and the standard deviation (STDEV) of the Mech and Col ceramics.....57
Table 4.7: The exergy efficieny ξ of the EC cooling system 70

Abbreviations

AFM	... atomic force microscope
ac	... alternating current
C	... cubic phase
Cer	... ceramics
CHX	... cold heat-exchanger
CNR	... chemically ordered region
CP	... critical point
Col	... PMN-10PT, prepared by the columbite synthesis
DSC	... differential scanning calorimetry
dc	... direct current
EC	... electrocaloric
EDXS	... energy-dispersive X-ray spectroscopy
FE-SEM	... field-emission scanning electron microscope
FE	... ferroelectric phase
GB	... grain boundary
GS	... grain size
HHX	... hot heat-exchanger
HP	... hot pressed
HR-TEM	... high-resolution transmission electron microscope
ICP	... inductively coupled plasma
IPA	... isopropanol
M_B	... monoclinic phase – space group Cm
M_C	... monoclinic phase – space group Pm
PE	... paraelectric phase
PFM	... piezoresponse mode
PMN	... $Pb(Mg_{1/3}Nb_{2/3})O_3$
PNR	... polar nanoregion
PT	... $PbTiO_3$
Py	... pyrochlore phase
PZT	... $Pb(Zr_xTi_{1-x})O_3$
R	... rhombohedral phase
RD	... relative density
Mech	... PMN-10PT, prepared by the mechanochemical synthesis
MPB	... morphotropic phase boundary
WC	... tungsten carbide
WDXS	... wavelength-dispersive X-ray spectroscopy
XRD	... X-ray powder diffraction
YSZ	... ZrO_2 stabilized with Y_2O_3

Symbols

A	... surface area of the sample
a	... fitting parameter
C	... capacitance
c_E	... specific heat capacity at constant electric field
c_E^a	... specific heat capacity at constant electric field of the active component
c_E^i	... specific heat capacity at constant electric field of the passive component
$c_E^{standard}$	... specific heat capacity at constant electric field of the standard
COP	... coefficient of performance
COP_C	... coefficient of performance of the Carnot heat pump
D	... dielectric displacement
DSC^{sample}	... DSC curve of the sample
$DSC^{standard}$	... DSC curve of the standard sample
d	... thickness
d_{10}, d_{50}, d_{90}	... particle size reached by 10 %, 50 % and 90 % of the particles
E	... electric field
E_b	... dielectric breakdown strength
E_b^{dense}	... dielectric breakdown strength of a completely dense material
E_{dipole}	... electric field of a dipole
E_{loc}	... local electric field
E_T	... threshold electric field
G	... Gibbs free-energy density
l_i	... initial dimension of a sample at room temperature
l_T	... dimension of a sample at a selected temperature
$\Delta l/l$	... relative shrinkage
m^a	... mass of the active component
m^i	... mass of the passive component
n	... degree of the electric-energy recovery
P	... dielectric polarization
P_{IRR}	... irreversible polarization function
P_s	... saturated polarization
p_e	... pyroelectric coefficient
Q	... heat density
Q_C	... heat density that is transferred from the heat source to the system
Q_H	... heat density that is transferred from the system to the heat sink
q	... heat flow
S	... entropy density
ΔS_H	... entropy density change due to hysteresis losses
ΔS_P	... dipolar entropy density change
T	... temperature
$T_{ambient}$	... ambient temperature

T_{bath} ... bath temperature
T_B ... Burns temperature
T_c ... Curie point
T_f ... freezing temperature
T_m ... temperature of the dielectric permittivity maximum
T_{room} ... room temperature
T_s ... sintering temperature
T_{sample} ... temperature of the sample
T_{sur} ... surface temperature
ΔT_{EC} ... electrocaloric temperature change
$\Delta T_{EC}^{hyst.}$ ... electrocaloric temperature change of a material without any hysteresis losses
$\Delta T_{EC}/E$ ... electrocaloric coefficient
$tan\delta$ ... dielectric losses
t_s ... sintering time
V ... voltage
V_b ... breakdown voltage
X ... stress
x ... strain
W ... work density
W_N ... net work density, done on the system
$W_{N,R}$ ... net work density done on the system, when a n-degree of the electric-energy is recovered
w_{ac} ... power generated in the sample by an ac current
α ... heat-transfer coefficient
ε_r ... relative dielectric permittivity
ε'_{max} ... maximum value of the real part of the dielectric permittivity
ε_0 ... dielectric permittivity of vacuum
ε^* ... complex dielectric permittivity
ε' ... real part of the complex dielectric permittivity
ε'' ... imaginary part of the complex dielectric permittivity
η ... electrocaloric efficiency
ν ... frequency
ξ ... exergy efficiency
ρ ... density

Chapter 1

Introduction

The Introduction chapter provides a brief literature overview relevant to the topic of this thesis. It begins with the basic definitions of dielectric polarization and introduces the ferroelectric and relaxor ferroelectric materials. The second section of this chapter is focused on the electrocaloric effect, cycle and measurements. The third section addresses the phase diagram, properties and synthesis of the (1-x)Pb($Mg_{1/3}Nb_{2/3}$)O_3-x$PbTiO_3$ solid solution, while the last section includes an overview of the reported electrocaloric data for this material.

1.1 Polar Oxides

1.1.1 Dielectric Polarization

A dielectric material is an electrically insulating material that is polarized by an applied external electric field (E). The induced dielectric polarization (P) is defined as the relative shift of the barycenters of positive and negative charges in opposite directions within the dielectric material. It is given by:

$$P = \varepsilon_0(\varepsilon_r - 1)E, \tag{1.1}$$

where ε_0 and ε_r are the dielectric permittivity of a vacuum and of the material, respectively.

The total surface charge density that is induced in the material by the applied field is given by the dielectric displacement (D):

$$D = \varepsilon_0 E + P, \tag{1.2}$$

Equations (1.1) and (1.2) give the relation:

$$D = \varepsilon_0 \varepsilon E. \tag{1.3}$$

In a dielectric material the local electric field (E_{loc}) is not equal to the applied electric field E due to the electrostatic interaction between the electric dipoles. The E_{loc} at the position of a particular dipole is given by the superposition of the applied electric field E and the field of all the other dipoles and is given by [1], [2]:

$$E_{loc} = E + \sum E_{dipole}, \tag{1.4}$$

where E_{dipole} is the electric field of an individual dipole. The local electric field of a material with a known ε_r is expressed as [3], [4]:

$$E_{loc} = \frac{\varepsilon_r + 2}{3} E. \tag{1.5}$$

If an alternating voltage is applied, the charge stored in a dielectric material has both real (in-phase; ε') and imaginary (out-of-phase; ε'') components, and thus the relative permittivity is expressed as:

$$\varepsilon^* = \varepsilon' - i\varepsilon''. \tag{1.6}$$

The dielectric losses ($tan\delta$) are expressed as the relationship between ε'' and ε' [1]:

$$tan\delta = \frac{\varepsilon''}{\varepsilon'}. \tag{1.7}$$

1.1.2 Ferroelectric Materials

All crystals are divided into 32 crystal classes. Of these, 21 do not possess a center of symmetry and are therefore referred to as the non-centrosymmetric crystals, and 20 of them exhibit the piezoelectric effect. These materials develop an electric charge on their surface when a mechanical stress is exerted on them (direct piezoelectric effect), while the application of an external electric field causes an elastic strain (inverse piezoelectric effect). Among these 20 crystal classes 10 are permanently polarized within a given temperature range, and are referred to as pyroelectric materials. Unlike the piezoelectrics, the pyroelectrics develop their polarization spontaneously and form permanent dipoles in the structure. This polarization also changes with temperature – hence the term pyroelectricity [1].

There is a subgroup within these 10 crystal classes that possesses at least two equilibrium orientations of the spontaneous polarization in the absence of the electric field, which can be switched by the electric field. These materials are ferroelectrics. Since the origin of the above-mentioned properties lies in the crystal structure, the ferroelectrics are categorized by their unit-cell structure [1], [2]. The perovskite group with the ABO_3 unit-cell is the most important and $BaTiO_3$ is its prototype representative [5].

Above 130 °C $BaTiO_3$ is cubic and it is in the paraelectric state. The Ti^{4+} ion is positioned in the center of the unit cell, as schematically shown in Figure 1.1 (a).

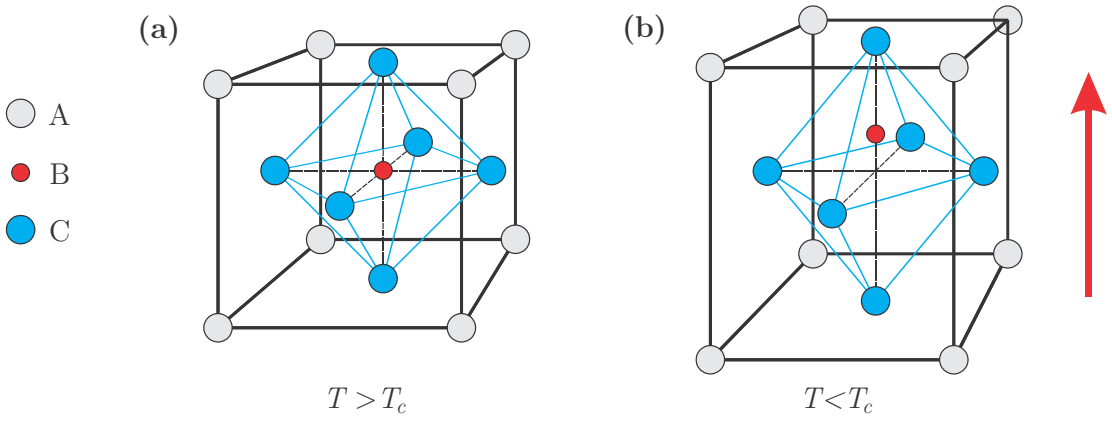


Figure 1.1: Unit cell of (a) cubic and (b) tetragonal ABO_3 structure. The arrow schematically indicates a possible displacement of the central B ion during the transition from cubic to the tetragonal ferroelectric phase that leads to a spontaneous polarization. After [2].

If the temperature is decreased below 130 °C a tetragonal lattice distortion occurs, resulting in the appearance of spontaneous polarization as a consequence of the displacement of the central Ti^{4+} ion (Figure 1.1 b).The temperature at which a ferroelectric material undergoes a structural phase transition to a state where the spontaneous polarization vanishes is defined as the Curie point (T_c) [5].

Below the T_c the $BaTiO_3$ displays the hysteretic dependence of P vs. E (Figure 1.2 a). Upon further cooling below the Curie point the $BaTiO_3$ undergoes two phase transitions, from the tetragonal to the orthorhombic phase at 0 °C, and from the orthorhombic to the rhombohedral phase at -90 °C. Note that only the transition temperature from the paraelectric phase into the first ferroelectric phase is called the Curie point. As shown in Figure 1.2 (b), these structural changes are observed as changes in ε' vs. temperature (T), and at T_c the ε' value reaches a sharp maximum [5]. As a characteristic property of ferroelectrics, the magnitude and the position of this maximum do not, or only slightly, depend on the measurement frequency (ν).

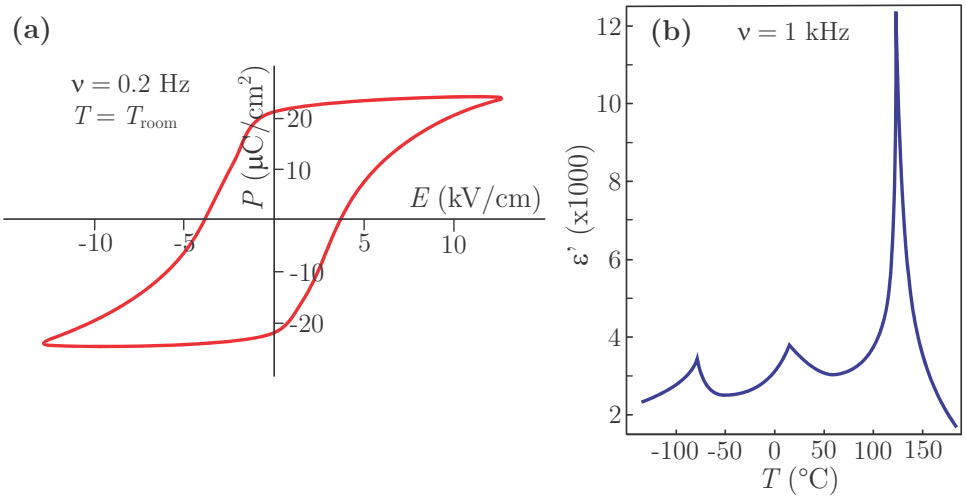


Figure 1.2: (a) The $P-E$ hysteresis loop of a $BaTiO_3$ single crystal, measured at room temperature (T_{room}) [6] and (b) the temperature dependence of ε' of $BaTiO_3$ ceramics with an average grain size of 13 µm [7].

1.1.3 Relaxor Ferroelectric Materials

Unlike classical ferroelectrics, relaxor ferroelectrics (or briefly relaxors) show a strong frequency dependence of the dielectric permittivity maximum and a slim hysteresis loop. No long-range ferroelectric phase is developed and the average symmetry remains cubic down to very low temperatures.[1] The described behavior is typical for materials in which the A, B, or both sites in the ABO_3 unit cell are occupied by different ions. The $Pb(Mg_{1/3}Nb_{2/3})O_3$ (PMN) is a prototype relaxor [9], [10].

It was found that in the PMN the B-site ions have a random and disordered distribution; however, the charge neutrality is preserved due to the average fractions of Mg^{2+} and Nb^{5+} of 1/3 and 2/3 for, respectively. This chemical (also called compositional) disorder of B-ions in the PMN is the essential structural characteristic since no relaxor behavior is found in completely chemically ordered materials. In PMN the disordered state cannot be changed by any heat treatment due to the too long (infinite) relaxation times of the B-site-ion ordering [9]–[11]. On the other hand, in some other relaxors, such as

[1] $Pb(Mg_{1/3}Nb_{2/3})O_3$ remains cubic to approximately -220 °C [8].

$Pb(Sc_{1/2}Nb_{1/2})O_3$, the compositional order can be changed by heat treatment. Namely, if the $Pb(Sc_{1/2}Nb_{1/2})O_3$ is annealed above 1200 °C, it is chemically disordered and it behaves as a relaxor. In contrast, annealing at ~1000 °C results in a chemically ordered $Pb(Sc_{1/2}Nb_{1/2})O_3$, which behaves as a classical ferroelectric [12]–[14].

Although the chemical disorder in PMN is fixed (″quenched″), the analysis with high-resolution transmission electron microscopy (HR-TEM) revealed that in PMN also small chemically ordered regions, denoted as chemical nanoregions (CNR) exist [15]. These ~2–5-nm-large CNR do not change in size within a broad temperature interval (from around -250 to over 1000 °C) and have the 1:1-ordered B-sites. As compared to the nominal composition of $Pb(Mg_{1/2}Nb_{1/2})O_3$ they are rich in Mg^{2+} and they represent regions with a relative deficiency of positive charge. In contrast to CNR, there exist Nb^{5+}-rich regions with a surplus of positive charge, which are located around the CNR so that the overall chemical composition and charge equilibrium in PMN are preserved [15], [16]. It is believed that the CNR appear because they reduce the total free energy of the system, but they cannot grow due to the difference in composition and the lack of charge equilibrium. [15].

At very high temperatures the PMN exists in a non-polar paraelectric phase, similar to conventional ferroelectrics above the Curie point T_c. Upon cooling below the Burns temperature (T_B), polar nanoregions (PNR), embedded in a paraelectric matrix, form in PMN, and the material transforms into an ergodic relaxor [9], [17], [18]. It was initially believed that the Burns temperature in inorganic relaxors is located at ~330 °C [17], [19]. However, Bobnar et al. [20] later showed that PNR in the PMN are present at least up to ~530 °C[2], and suggested that T_B exists above ~530 °C or that T_B is not a well-defined temperature transition and PNR are formed continuously across a broad temperature range. The formation of PNR in the PMN below T_B is presumably correlated with the presence of random local electric fields, which originate from the afore-described chemical inhomogeneity of PMN. Dielectric dipoles in PNR can be oriented by an external electric field, but after the field's removal they return to the initial state, i.e., the state where the polarization of PNR is random and the macroscopic spontaneous polarization is zero [21].

Due to the PNR, the PMN in the ergodic state shows a specific relaxor behavior, such as a slim $P-E$ hysteresis loop (Figure 1.3 a) and a broad maximum in the $\varepsilon'(T)$, the temperature of which (T_m) is strongly frequency dependent (Figure 1.3 b).

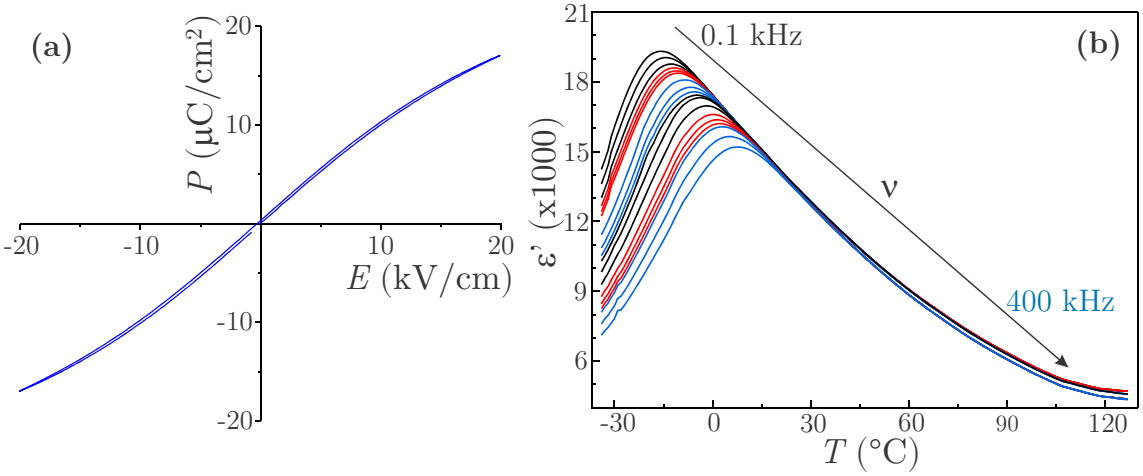


Figure 1.3: (a) the $P-E$ hysteresis loop at 1 kHz and (b) temperature dependence of ε' of PMN ceramics with an average grain size of 2.0 μm, measured on cooling [22].

[2] Measurements were not performed above ~530 °C due to the temperature limit of the measurement equipment.

Unlike in classic ferroelectrics, where a sharp and frequency-independent dielectric maximum is associated with the paraelectric-to-ferroelectric phase transition, this peak is not attributed to any structural phase transition but it is a result of the specific dielectric dynamics of PNR, which are present in the ergodic PMN phase [9]. The presence of PNR is additionally confirmed by a non-linear $P-E$ dependence, see Figure 1.3 a. After the field-removal the PNR switch back to the initial state, resulting in zero macroscopic polarization.

By cooling the PMN from T_B over the ergodic state, i.e., the state where all relaxation times are finite, the PNR gradually grow in size, the relaxation times increase, until at the freezing temperature (T_f ~ -50 °C) the PNR freeze. At T_f the longest relaxation times diverge and PMN undergoes the transition into the non-ergodic state [23]. From the non-ergodic relaxor a long-range ferroelectric order can be irreversibly induced by the application of an electric field that is higher than the threshold field (E_T) [24]–[26]. This is the first-order relaxor-to-ferroelectric phase-transition and is accompanied by a high entropy change. As shown in the $E-T$ phase diagram for the PMN single crystal (Figure 1.4), the critical point (CP) separates the first-order transition line and the Widom line where a supercritical evolution is observed. [27], [28].

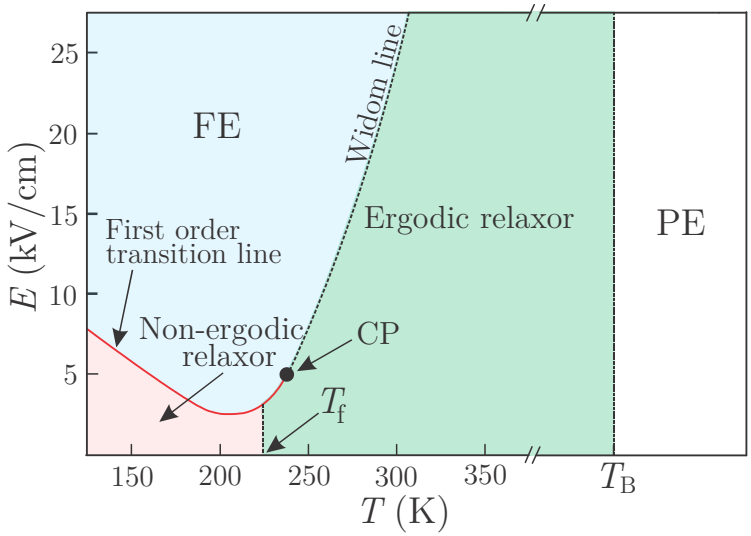


Figure 1.4: Phase diagram of the PMN single crystal, obtained by applying a bias electric field along the [113] direction at a constant temperature. FE – ferroelectric phase, PE – paraelectric phase, CP – critical point. After [27].

1.2 Electrocaloric Effect

The electrocaloric (EC) effect is defined as the change in entropy and, consequently, in the temperature of a dielectric material due to the electric-field-induced changes in the polar states. Because it is directly related to the polarization change under an electric field it is especially strong in materials such as ferroelectrics and relaxors. The application of the electric field to the material causes a partial alignment of dipoles and consequently a reduction of entropy of the dipole system.

Under adiabatic conditions the temperature of the dielectric is increased to keep the total entropy of a material constant. In a reverse process, as the applied electric field is reduced to zero and the dipoles return to the disordered state, an increase in the total entropy of the dipole system occurs, the dielectric will cool down for the EC temperature

change (ΔT_{EC}) [29]–[31]. Besides the ΔT_{EC} and electric field E, the EC coefficient[3] ($\Delta T_{EC}/E$) gives additional information about the investigated EC material and allows a comparison with other EC materials [32]

1.2.1 Thermodynamics of the Electrocaloric Effect

The thermodynamics of the EC effect is described as follows. The differential form of the Gibbs free-energy density (G) of a dielectric material can be written as [30]:

$$dG = -SdT - x_i dX_i - D_i dE_i, \tag{1.8}$$

where S, x and X are the entropy density, strain and stress, respectively. S, x and D can be expressed as:

$$S = -\left(\frac{\partial G}{\partial T}\right)_{X,E}, x_i = -\left(\frac{\partial G}{\partial x_i}\right)_{T,E}, D_i = -\left(\frac{\partial G}{\partial E_i}\right)_{X,T}. \tag{1.9}$$

The relations between the (S,T) and (D,E) pairs of parameters are given by the following Maxwell relation:

$$\left(\frac{\partial S}{\partial E_i}\right)_{T,X} = \left(\frac{\partial D_i}{\partial T}\right)_{E,X}. \tag{1.10}$$

The specific heat capacity at constant electric field (c_E) is defined as [30]:

$$c_E = \frac{T}{\rho}\left(\frac{\partial S}{\partial T}\right), \tag{1.11}$$

where ρ is the density of the material. From Eq. (1.10) and (1.11) we obtain the expression for the change of T under applied E:

$$\left(\frac{\partial T}{\partial E}\right)_S = \frac{T}{c_E \rho}\left(\frac{\partial D}{\partial T}\right)_E = \frac{T}{c_E \rho} p_e, \tag{1.12}$$

where p_e is the pyroelectric coefficient. By further assuming a constant stress X, the EC temperature change ΔT_{EC} is expressed as:[31]–[33]

$$\Delta T_{EC} = -\frac{T}{\rho}\int_{E_1}^{E_2} \frac{1}{c_E}\left(\frac{dD}{dT}\right)_E dE = -\frac{T}{\rho}\int_{E_1}^{E_2} \frac{1}{c_E}\left(\frac{dP}{dT}\right)_E dE \tag{1.13}$$

Eq. (1.12) and (1.13) show that the p_e is proportional to the ΔT_{EC}. Therefore, in order to achieve a large ΔT_{EC}, the dielectric material should possess a large p_e over a broad electric field and temperature ranges. In the case of ferroelectric and relaxor materials, a large pyroelectric effect exists near the dielectric peak permittivity at T_m.

[3] In some literature denoted as EC responsivity.

1.2.2 Electrocaloric Cycle

In Figure 1.5 the basic idea of an EC cycle is shown. In the initial state, the $E = 0$ and the material has the initial temperature T_1, which is equal to the surrounding temperature. The EC cycle consists of four steps as follows [31], [32]:

1st step - adiabatic polarization: An electric step-signal is applied to the EC material, which causes a partial orientation of the electrical dipoles with regard to the direction of the applied E. Due to the dipole alignment, the entropy of the dipole system decreases, and under adiabatic conditions, where the total entropy of the EC material is kept constant, the EC material heats above the initial temperature T_1.

2nd step – isoelectric enthalpy transfer: The heat is removed to the surroundings (or heat sink) at the applied E. The constant E prevents the dipoles from ″absorbing″ the heat, therefore, the entropy of the dipole system remains constant and the total entropy decreases.

3rd step – adiabatic depolarization: The E is removed in ″an instant″ and the dipoles revert to the less-oriented state and the entropy of the dipole system decreases. Under the adiabatic conditions the material cools below the initial temperature T_1 for ΔT_{EC}.

4th step – isoelectric entropic transfer: The E is kept at zero. Because the EC material is cooler than the surroundings, the heat migrates from the surroundings (or the heat source) into the working material. By reaching the initial temperature T_1, the EC material completes the EC cycle.

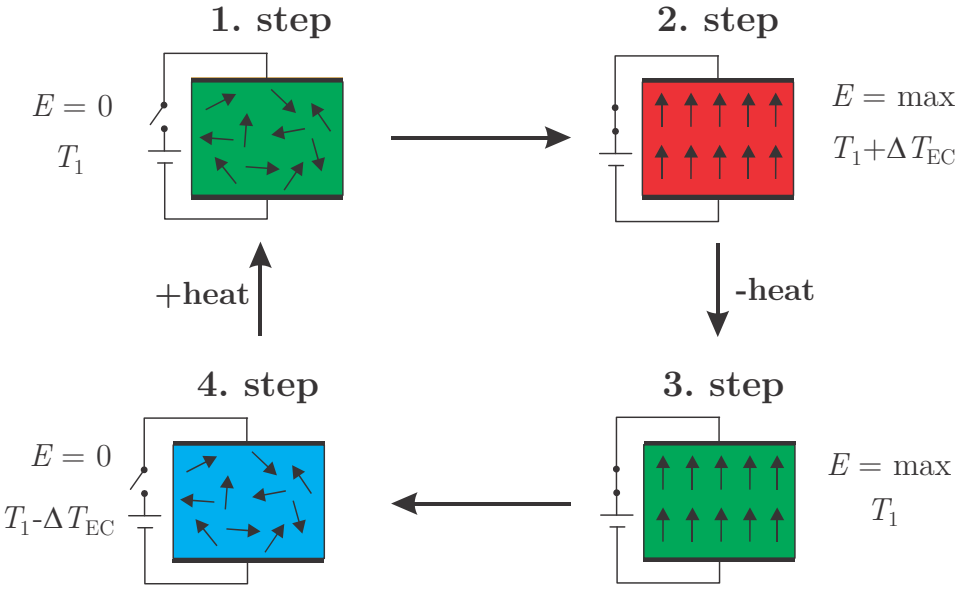


Figure 1.5: Schematic presentation of the EC cycle. The numbers of the individual steps corresponds to the description in the text. After [32].

From the described EC cycle we can easily recognize the basic idea of EC cooling, which is being considered as an alternative to existing cooling technologies. EC cooling has the potential to provide refrigeration systems with a much lower environmental impact, higher energy efficiency and lower level of noise and vibration than the conventional vapor compression refrigeration. Unlike conventional refrigerators, the EC cooling systems can be of compact sizes because there is no need for large-size components, like compressor, evaporator, etc. Furthermore, because of the strong insulating character of the EC materials, and hence a negligible Joule heating, an EC cooling device could be more efficient than the solid-state thermoelectric devices [32], [34], [35]. For the purposes of application

the EC materials need to be incorporated into a working system [32], [36], [37]. To date, several cooling-system concepts were proposed in the literature [38]–[42] and some of them have been realized as the first proof-of-concept devices [37], [43].

1.2.3 Measuring the Electrocaloric Effect

The basis for an EC study of a material is an accurate measurement system, which enables the determination of ΔT_{EC} as a function of electric field amplitude E and temperature T. To date, there is no standardized or validated measurement method, or even a commercially available EC measurement system. Nevertheless, until now many different methods have been developed, which can be divided in two groups, i.e., indirect and direct EC measurement methods. In the former case, the ΔT_{EC} is obtained through a calculation from other experimental data. The advantage of the indirect method is that the measurement and calculation procedures are simple but the obtained ΔT_{EC} is just the estimated value. The direct EC measurements, on the other hand, are performed so that the temperature of a sample or heat flow[4] from/to the sample is measured directly, when an electric signal is applied to the sample. The direct measurements give more reliable results than the indirect EC measurements; however, they are more challenging and time consuming [34], [35]. In the following text both methods are briefly described.

1.2.3.1 Indirect EC Measurements Using a Thermodynamic Approach

The EC temperature change ΔT_{EC} was derived in Section 1.2.1. As can be seen from Eq. (1.13), the ΔT_{EC} of a studied material with the density ρ and the specific heat capacity c_E, is determined from the dielectric polarization P as a function of the temperature T and electric field E. The $P(T, E)$ data are obtained by measuring the $P - E$ hysteresis loops at different temperatures (Figure 1.6 a). The $(\partial P/\partial T)_E(T)$ data are transposed to $(\partial P/\partial T)_T(E)$ and integrated from E_1 to E_2. The integration gives the ΔT_{EC} as a function of T at selected E. In the EC studies the results are often represented as ΔT_{EC} vs. T at several selected E (Figure 1.6 b), which provides a good description of the EC behavior for the investigated material.

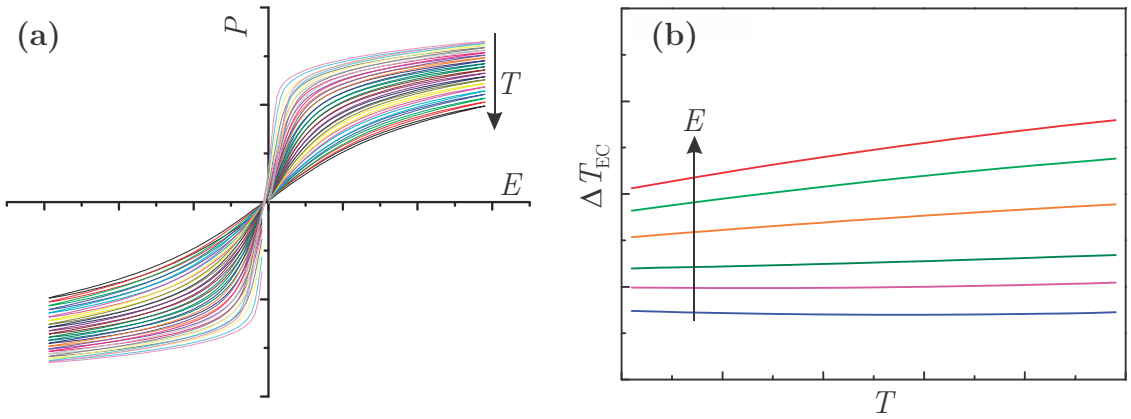


Figure 1.6: (a) $P - E$ hysteresis loops obtained at different temperatures. (b) Temperature dependence of the indirectly determined ΔT_{EC} at different electric fields. After [35].

In the literature we can find guidelines about how the ΔT_{EC} should be indirectly determined [32], [35], [44]. However, to the best of our knowledge, it is not generally accepted, which measurement conditions should be used in order to evaluate the ΔT_{EC}.

[4] In case that a direct EC measurement is performed in a modified differential scanning calorimeter.

For example, the measured $P-E$ hysteresis loops and consequently the calculated ΔT_{EC} can differ with regard to the used shape and frequency of the applied electric signal. In addition, it is important that the investigated EC material has as high as possible electrical resistivity. Conversely, the ΔT_{EC} can be easily overestimated. As shown by Lu et al. [45], the indirect approach should not be applied to relaxors in the non-ergodic state. But, at high enough electric fields the long-range ferroelectric order is induced in non-ergodic relaxors, see Figure 1.4. Hence, the indirect approach may be used at such field amplitudes to determine the ΔT_{EC}.

1.2.3.2 Direct Measurements of the EC Effect Using High-Resolution Calorimetry

In order to measure the ΔT_{EC} directly, different research groups use in-house-built EC measuring systems or they modify commercial systems. An example of such a system is a modified high-resolution calorimeter, in which the EC measurement is carried out by stabilizing the temperature of the bath, and the sample temperature is measured as a function of time, while an electric signal is applied to the sample [35], [44].

In an EC measurement different shapes of electric signals can be applied. The most widely used is the electric step-signal (see Figure 1.7). When the electric field is applied, the sample temperature rapidly increases due to the EC effect. Then the sample temperature decreases to the initial temperature T_{bath}, as a result of the dissipation of heat. When the T_{bath} is reached, the electric field is removed and the temperature of the material rapidly decreases below the initial temperature for the ΔT_{EC}. Afterwards, due to the heat migration, the sample temperature slowly increases to the initial temperature T_{bath}. The internal thermal response times of the sample due to the EC effect are usually very short (<1 s); however, the relaxation of the sample temperature back to the T_{bath} can be as long as 100 s or even more. Therefore, the time span of the electrical pulses has to be long enough to allow the sample temperature to return to the T_{bath} [44].

Note that the electric step-signal due to its symmetric shape provides additional information about the measured sample. Namely, from the comparison of the positive and negative ΔT_{EC}, i.e., when the electric field is applied and removed, the asymmetry (or symmetry) of the EC effect can be determined. This can give some additional information about possible Joule heating due to the leakage current, internal dielectric losses related to the wide $P-E$ hysteresis loop or large switching currents. A schematic representation of the direct EC measurement of a sample with noticeable Joule heating is shown in Figure 1.7 (b). It can be seen that the sample temperature does not relax back to the initial temperature T_{bath} while the E is still applied [44].

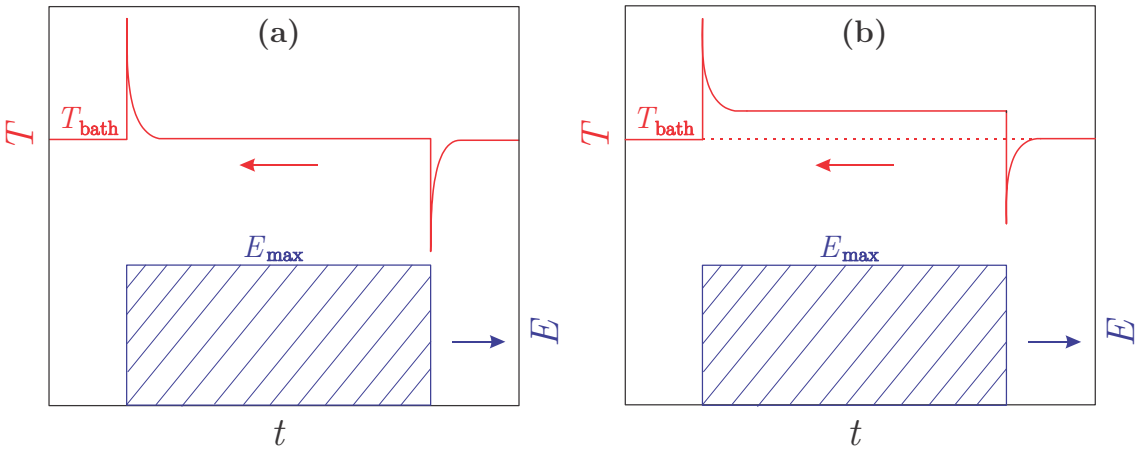


Figure 1.7: Schematic representation of the EC measurements for a sample (a) without and (b) with Joule heating. After [35], [44].

1.2.4 Importance of the Dielectric Breakdown Strength in Electrocaloric Materials

Dielectric materials will lose their insulating properties when they are placed in an electric field if the field exceeds a certain critical value. This phenomenon is known as the dielectric breakdown, and the corresponding critical electric field is referred to as the dielectric breakdown strength (E_b). It is defined as the maximum potential gradient to which a material can be subjected without the loss of insulation [46]:

$$E_b = \left(\frac{dV}{dx}\right)_{max} = \frac{V_b}{d}, \tag{1.14}$$

where V_b is the breakdown voltage and d is the thickness of the sample.

The EC temperature change ΔT_{EC} also depends on the applied electric field E (see Eq. (1.13)), therefore, understanding of the breakdown phenomenon is critical [47]. Here, a few of the most important factors that affect E_b are described, while further details about the breakdown phenomena can be found in Appendix A.

The E_b for different dielectric materials is inversely proportional to the dielectric permittivity ε' (see Figure 1.8)[5]. For example, a linear dielectric such as Al_2O_3 possesses a high E_b (~8,000 kV/cm) and a low ε' (~10). In contrast, a non-linear dielectric such as $0.65Pb(Mg_{1/3}Nb_{2/3})O_3$-$0.35PbTiO_3$ exhibits a modest E_b (~100 kV/cm) and a high ε' (~60,000 at T_m). Furthermore, the experimental data of different materials collected in Figure 1.8 reveal that the dielectric breakdown strength shows an inverse square-root correlation to the dielectric permittivity [4], [48]:

$$E_b \propto (\varepsilon')^{-\frac{1}{2}} \tag{1.15}$$

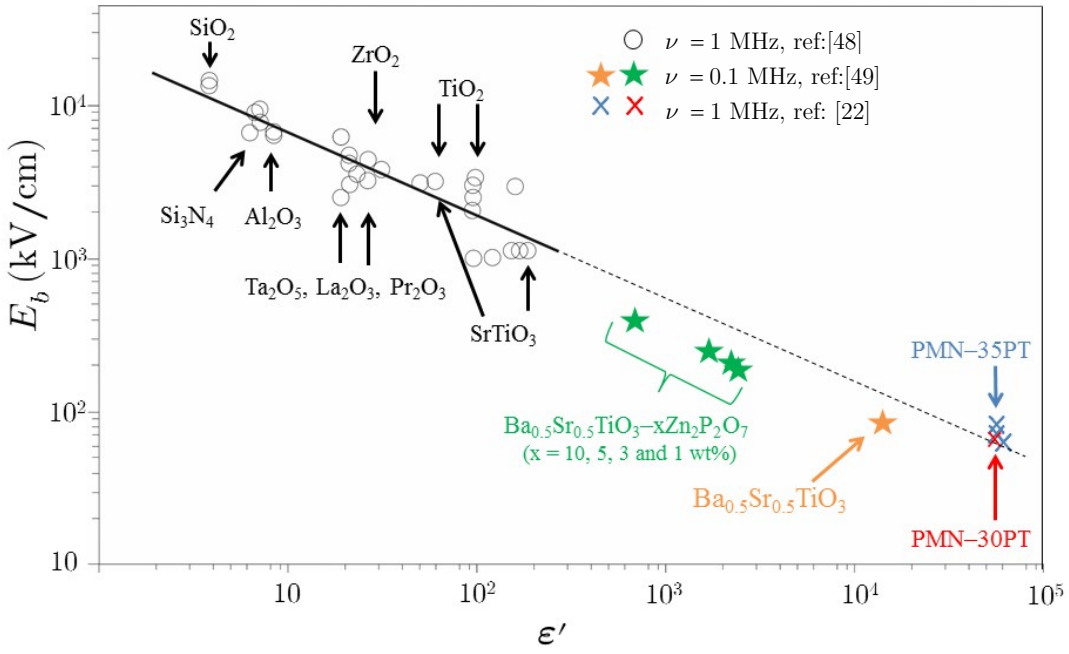


Figure 1.8: Dielectric breakdown strength E_b vs. dielectric premittivity ε' for different materials at certain frequencies. After [22], [48], [49].

[5] For ferroelectric and relaxor materials the ε' is given at dielectric permittivity maximum T_m.

Such a correlation was additionally confirmed for the $Ba_{0.5}Sr_{0.5}TiO_3$–$xZn_2P_2O_7$ material with different compositions (x = 0, 1, 3, 5, 10 wt%; green and orange stars in Figure 1.8) and for PMN–PT bulk ceramics (red and blue crosses in Figure 1.8).[6] The correlation between E_b and ε' is related to the local electric field E_{loc}, which increases with the externally applied field and the material's ε' (see Section 1.1.1, Eq. (1.4) and (1.5)). The E_{loc} could weaken, or even break polar bonds inside a dielectric material, which results in the development of a conductive path and consequently in the occurrence of a dielectric breakdown [4], [48].

The microstructure is another critical factor that affects the E_b. It was shown for different ceramic materials (Al_2O_3, $BaTiO_3$, (1-x)$Ba_{0.5}Sr_{0.5}TiO_3$-$xZn_2P_2O_7$, etc.) with grain sizes (GSs) in the micro-range that the smaller the GS of a material the higher the E_b [46], [49]–[53]. For example, $BaTiO_3$ ceramics with an average GS of ~1 µm exhibit an approximately two times higher E_b (~2,000 kV/cm) than the same material with an average GS of ~3 µm [52]. This relationship can be attributed to the fact that more grain boundaries represent a longer path of least resistance for the tunneling current, which requires a higher electric field for the dielectric breakdown to happen [54].

In [55] it was shown for $Pb(Zr_xTi_{1-x})O_3$[7] (PZT) ceramics that the lower the porosity and pore size the higher the E_b. For example, PZT with porosity of ~10 % and ~20 % possessed E_b >30 kV/cm and <20 kV/cm, respectively. The samples with a higher density possess a higher E_b because the gas, entrapped in the pores, possesses a significantly lower E_b[8] than the E_b of the material surrounding the entrapped gas [46], [55]. The entrapped gas can ionize at high electric fields, which leads to a high current flow, local heating and cracking, and finally results in a breakdown [46]. Besides the microstructure there are also other parameters that can significantly influence the E_b, e.g., the thickness and shape of the sample and the measurement conditions (see Appendix A).

1.2.5 Energy Efficiency of Electrocaloric Materials

The EC materials are not just interesting from the scientific point of view, but also due to their possible utilization in cooling. This idea was a driving force for numerous EC studies, especially after 2006, when Mischenko et al. [57] reported a giant EC effect, i.e., ΔT_{EC} = 12 °C at 480 kV/cm and 220 °C, in $PbZr_{0.95}Ti_{0.05}O_3$ thin films. Surprisingly, the efficiency of EC materials or prototype devices has rarely been discussed, although it is of the utmost importance for applications. To date, only a small number of studies [36], [58] analyzed the work needed to drive different EC ceramic and polymer films. They analyzed the work and the heat, which is absorbed or released by the EC material due to the EC effect. The work done on an EC material, is the electrical work, which is needed for polarization (charging) of the EC material and can be given as the work density (W) in [30]:

$$W = \int E \times dD. \tag{1.16}$$

The released or absorbed heat density (Q) due to the EC effect is given by [59]:

$$Q = \Delta T_{EC} \times c_E \times \rho. \tag{1.17}$$

As was shown in Section 1.2.2, the EC material releases and absorbs heat in the second and fourth steps of the EC cycle. However, in the analyses made in [36], [58], the EC

[6] Note that the small deviations from linear behavior in Figure 1.8 could be attributed to different measurement frequencies.

[7] Composition of PZT was not given.

[8] The E_b of air is 30 kV/cm (flat electrodes) [56].

material was not subjected to the EC cycle, but it was investigated under isothermal conditions at T_m, where the dielectric permittivity displays the maximum value. The performed work on the EC material was calculated by using Eq. (1.16) and the $D(E)$ data were obtained from the *P(E)* measurements via Eq. (1.2). The absorbed heat was calculated by Eq. (1.17), and the ΔT_{EC} values were determined by the indirect method (Eq. (1.13)).

Defay et al. [58] introduced the dimensionless EC efficiency (η), which is for a random EC material under isothermal conditions given by:

$$\eta = \frac{|Q|}{|W|}. \tag{1.18}$$

The sign of η is positive for the EC material that releases the heat ($Q > 0$) when it is polarized ($W > 0$), and absorbs heat ($Q < 0$) on depolarization ($W < 0$). As was shown in [58] by the Landau theory, η varies with Q and therefore for different EC materials it can be meaningfully compared only if the Q values are similar. For the purposes of a comparison of different EC materials, the Q can be changed by varying the ΔT_{EC} (see Eq. (1.17)), and the ΔT_{EC} can be varied by the applied electric field E within $E = 0$ and E_b (see Eq. (1.13)).

Although Defay et al. [58] suggested a comparison of η at a similar absorbed heat Q, they provided only the values of η and Q, which were calculated from the maximum measured ΔT_{EC} of a selected material. Therefore, as can be seen from Figure 1.9, where some results for different EC materials from the references [36] and [58] are shown, the comparison of different materials is rather difficult. It seems that the most energy-efficient EC material is $Pb_{0.8}Ba_{0.2}ZrO_3$ due to it having by far the highest η, which approaches 30, at a relatively high absorbed heat Q of 46 J/cm^3. On the other hand, if the polymer films are compared, the poly(vinylidene fluoride-trifluoroethylene) 65/35 mol% reaches the highest η but it was calculated at a modest Q of 32.5 J/cm^3 (denoted as P(VDF-TrFE)* in Figure 1.9).

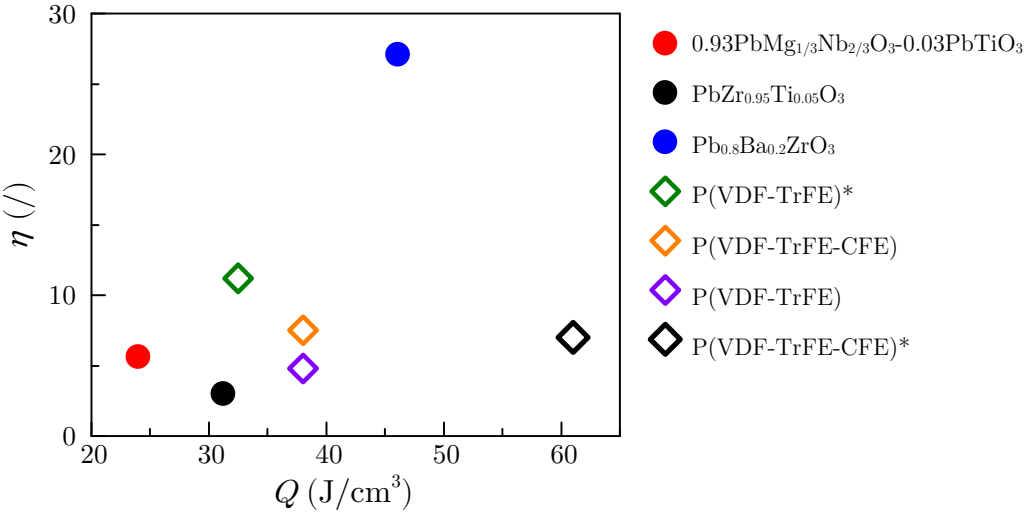


Figure 1.9: EC efficiency η as a function of the absorbed Q for some ceramic and polymer thin films. After [36], [58].

P(VDF-TrFE) – poly(vinylidene fluoride-trifluoroethylene) 55/45 mol%
P(VDF-TrFE)* – poly(vinylidene fluoride-trifluoroethylene) 65/35 mol%
P(VDF-TrFE-CFE) – poly(vinylidene fluoride-trifluoroethylenechlorofluoroethylene) 59.2/33.6/7.2 mol%
P(VDF-TrFE-CFE)* – poly(vinylidene fluoride-trifluoroethylenechlorofluoroethylene) 56.2/36.3/7.6 mol%

It should be pointed out that the EC materials in these studies were subjected to isothermal conditions and not to a thermodynamic cycle as in real cooling systems. Therefore, the type of the cycle, the temperature spans of the EC material and of the heat sink and source were not taken into account. Moreover, the $P-E$ hysteresis losses of a selected EC material could have an important influence on its efficiency, hence, they should be considered in the EC efficiency analysis.

Moya et al. [36] additionally proposed that the energy efficiency of an EC material can be substantially enhanced by energy recovery. Namely, the electric energy that is consumed for polarizing the EC material, i.e., charging the EC capacitor, represents some potential electric energy that could be recovered during the process of depolarizing (discharging). Recovery of as much as 80 % of the consumed electric energy could enhance η by a factor of five by using a dedicated electric circuit. However, no details to support such a hypothesis were provided.

1.3 (1-x)Pb($Mg_{1/3}Nb_{2/3}$)O_3-x$PbTiO_3$ Solid Solution

1.3.1 Phase Diagram

PMN is considered as a prototype relaxor material with a pseudocubic unit cell across a wide temperature range. It exhibits a slim $P-E$ hysteresis loop at room temperature (T_{room}) and a broad maximum in the temperature dependence of the dielectric permittivity with a strong frequency dispersion. Its dielectric permittivity peak reaches ~20,000 at -8 °C and 1 kHz [9]. In contrast to PMN, $PbTiO_3$ (PT) is a ferroelectric perovskite with a tetragonal unit cell at T_{room}. It displays a ″square″ hysteresis loop and its frequency-independent dielectric permittivity peak reaches ~10,000 at ~500 °C [5].

PMN and PT form a solid solution (1-x)Pb($Mg_{1/3}Nb_{2/3}$)O_3-x$PbTiO_3$ (PMN-100xPT) over the whole concentration range, x [60]. Figure 1.10 shows the real part of the dielectric permittivity ε' as a function of temperature for different compositions of PMN-PT. It can be seen that the addition of PT to PMN progressively shifts the permittivity peak towards higher temperatures, to ~40 °C and ~170 °C for PMN-10PT and PMN-35PT, respectively.

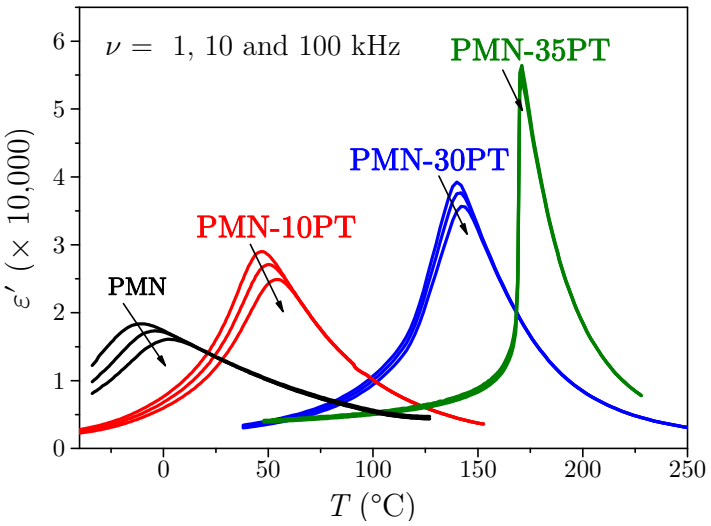


Figure 1.10: Temperature dependence of the dielectric permittivity ε' for different PMN-PT compositions. The arrow indicates the increase of frequency [22].

As the PT content increases, the relaxor behavior is gradually suppressed, i.e., the maximum dielectric permittivity peak becomes progressively sharper, and the $P-E$ hysteresis loop wider until at $x > 0.3$ the dielectric permittivity peak is frequency independent, as is typical for classical ferroelectrics.

Many attempts have been made to construct the temperature-composition ($T-x$) phase diagram for the PMN-PT system. Ouchi et al. [60] in 1965 proposed two phases, i.e., the cubic phase on the PMN-rich side and the tetragonal phase on the PT-rich side. Later studies revealed the existence of additional phases [61]. Namely, it was shown that a rhombohedral phase is already established in PMN-5PT and PMN-15PT at -258 °C and T_{room}, respectively [8]. This phase was thought to be the room-temperature phase up to the morphotropic phase boundary (MPB)[9] at x(PT)~$0.30-0.35$, with the tetragonal phase on the PT-rich side [61]–[63]. However, more recent studies have revealed the coexistence of two monoclinic phase regions between x(PT) = 0—0.35, denoted as M_B (space group Cm) and M_C (Pm) [65]–[67]. It should be noted that there is some disagreement between the studies regarding the position of the MPB and the phase fields. This is most probably the result of different procedures used for preparing the samples and the consequent variations in phase composition (see Section 1.3.2). The phase diagram of the PMN-PT system, which is based on some recent studies, is shown in Figure 1.11.

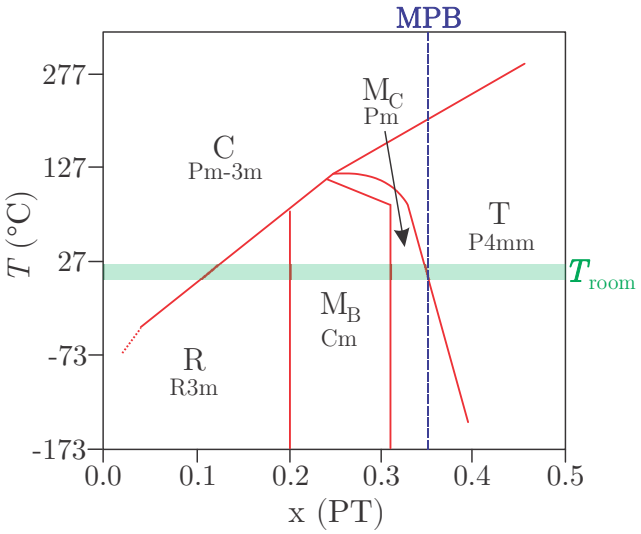


Figure 1.11: Phase diagram of the PMN-PT system. After [68], [69].

1.3.2 Role of the Grain Size and Chemical Homogeneity of (1-x)Pb($Mg_{1/3}Nb_{2/3}$)O_3-x$PbTiO_3$ Ceramics

The grain size effect on the dielectric properties of PMN and PMN-7PT was firstly studied by Papet et al. [70] and Randall et al. [71], respectively. They studied ceramic samples with grain sizes in the micrometer range[10] that were obtained by conventional sintering or hot pressing at different temperatures and times. As shown in Figure 1.12, in PMN as well as in PMN-7PT, a monotonic decrease of the dielectric permittivity ε' with decreasing grain size was observed, e.g., in PMN the maximum value of ε' decreased from ~18,000 (GS = 6.2 µm) to ~5,000 (GS = 0.3 µm) at 100 kHz. The authors of both studies

[9] MPB in a ($T-x$) phase diagram of a solid solution denotes a composition, where two or more phases coexist. The MPB composition is charaterized by maximum dielectric permittivity values [5], [64].

[10] PMN was studied in the grain size range from 0.3 µm to 6.2 µm [70] and PMN-7PT from 1.5 µm to 9.0 µm [71].

stressed that in all samples an amorphous Pb-rich phase was detected at the grain boundaries. Therefore, they suggested that the fine-grained samples had lower dielectric permittivity values than the coarse-grained samples due to the higher amount of grain boundaries and the low-dielectric-permittivity secondary phase.

Papet et al. [70] reported that annealing (600 °C, 24 h) of a sample that was hot pressed at 825 °C for 2 h resulted in an increase of the dielectric permittivity from 5900 to 7500, but no grain growth was observed. It was suggested that the increase in ε' is related to the release of the internal stresses during the annealing process.

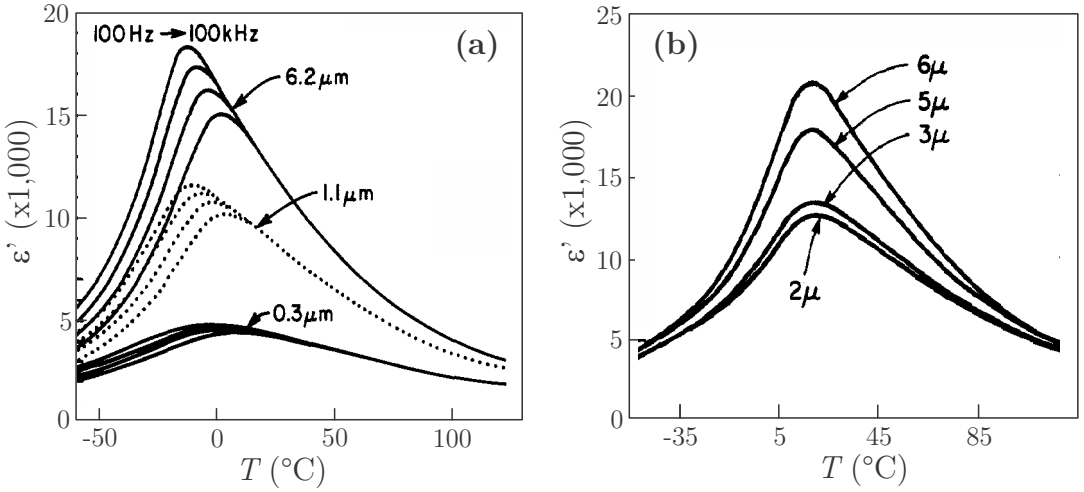


Figure 1.12: The grain-size dependence of the dielectric permittivity ε' as a function of temperature for (a) PMN [70] and (b) PMN-7PT [71].

Leite et al. [72] later studied the dielectric properties of PMN-35PT ceramics with different grain sizes and showed that besides the grain size, the chemical homogeneity also plays an important role. The ceramic samples with grain sizes from 0.6 µm to 10.8 µm were obtained by hot pressing at 950 °C for 0.5 h and subsequent annealing at 1150 °C for 5 h and 10 h, see Table 1.1. The dielectric investigation revealed that the sample with the finest grains, i.e., the sample that was only hot pressed, displayed a frequency-dependent dielectric permittivity maximum that is characteristic for relaxor compositions. In contrast, the coarse-grained samples, i.e., hot pressed and subsequently annealed, showed a classical ferroelectric behavior with a sharp and frequency-independent dielectric peak. Furthermore, post-annealing resulted in a strong increase of dielectric permittivity ε' and saturated polarization (P_s), and a downward shift of T_m. The authors suggested that the higher ε' and P_s values and the downward shift of T_m of the annealed samples are not connected with the larger grain size only, but also with the enhanced chemical

Table 1.1: Microstructure and dielectric properties of the hot-pressed PMN-35PT samples (HP; at 950 °C) and the samples subsequently annealed at 1150 °C. The maximum dielectric permittivity ε'_{max} and T_m were measured at 1 kHz. The arrows denote the trends of the increasing values. After [72].

Sample	ρ (g/cm^3)	GS (µm)	ε'_{max} (/)	T_m (°C)	P_s (µC/cm^2)
HP	8.12	0.6 ↓	8,160 ↓	190 ↑	~20 ↓
HP+Annealed (5 h)	8.12	7.0 ↓	34,110 ↓	172 ↑	~35 ↓
HP +Annealed (10 h)	8.12	10.8	41,720	169	~35

homogeneity.[11] They supported their hypothesis with energy-dispersive X-ray spectroscopy (EDXS), which revealed a considerable variation in the titanium and niobium concentrations in the ceramic powder. Furthermore, the chemical heterogeneity persisted even in the fine-grained sample, but not in the coarse-grained samples. The latter samples, which experienced the chemical homogenization process during annealing, possessed higher ε' and P_s values and a sharp dielectric maximum.

Carreaud et al. [73] studied the effect of the grain size in PMN and PMN-35PT ceramics. They reported that downscaling from the micro- to the nano-range in both compositions resulted in a continuous and significant decrease (by more than one order) in the value of the dielectric permittivity peak as well as in its widening. The PMN displayed relaxor behavior across the whole grain-size range, i.e., from 3 µm to 15 nm; however, a substantial suppression of the relaxor behavior was observed in the samples with grain sizes below 30 nm. On the other hand, PMN-35PT ceramics with the micro-sized grains exhibited a classical ferroelectric behavior; the ceramics with the grain-size between 200 nm and 30 nm showed a relaxor-like frequency-dependent dielectric peak; while in the ceramic samples with the grains below 30 nm the dielectric anomaly was not observed, the samples exhibited paraelectric behavior. The authors suggested that by decreasing the grain size of the PMN-35PT ceramics the macroscopic ferroelectric domains desegregated into smaller domains or PNR, which was observed as dielectric relaxation. A further grain size reduction led to the vanishing of the correlation between PNR, which was observed as the weakened or even vanished dielectric relaxation for PMN and PMN-35PT, respectively [73].

In another study, Alguero et al. [74] prepared PMN-35PT ceramics with average grain sizes of 4 µm and 0.15 µm and compared their $P-E$ hysteresis loops (see Figure 1.13). The coarse-grained sample exhibited a typical ferroelectric $P-E$ hysteresis loop, while the fine-grained sample displayed a much slimmer $P-E$ loop. Furthermore, in the former case the saturated polarization P_s was more than four times higher than in the latter case. The authors reached the conclusion that the ″poor″ hysteresis loop of the 0.15-µm-grain-sized sample is related to the hindered domain switching as a consequence of the reduction in the size of the ferroelectric domains [69].

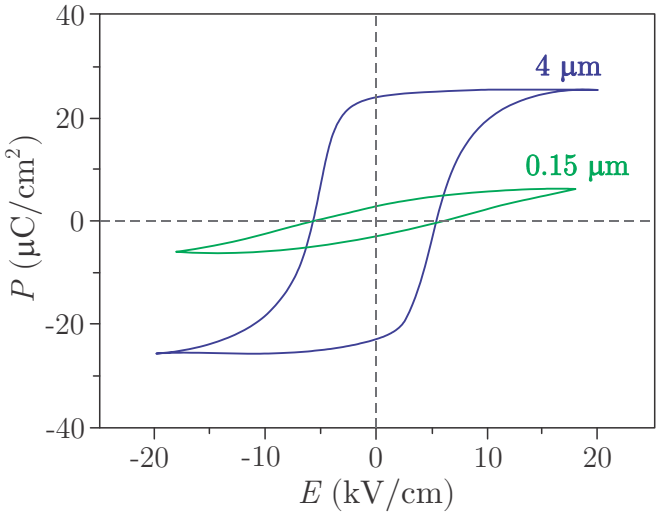


Figure 1.13: The $P-E$ hysteresis loops of the PMN-35PT ceramics with average grain sizes of 0.15 µm and 4 µm, measured at 0.1 Hz [74].

[11] The effect of the released stresses during the annealing process was excluded because the authors assumed that it was very unlikely that it would have a strong influence on the ε' [72].

1.3.3 Synthesis of the (1-x)Pb($Mg_{1/3}Nb_{2/3}$)O_3-x$PbTiO_3$ Ceramics

1.3.3.1 Columbite Synthesis

The conventional solid-state synthesis of PMN by mixing constituent oxides yields, in addition to the perovskite phase, an undesired pyrochlore lead niobate phase. This secondary phase has a low dielectric permittivity (~130 at T_{room}). The pyrochlore phase is thermodynamically stable, hence, it is difficult to eliminate it from the final product [75].

The reaction mechanism of the PMN from a stoichiometric PbO-MgO-Nb_2O_5 mixture was proposed by Inada, see Eq. (1.19)-(1.21) [76]. The reaction between lead oxide and niobium oxide results in the formation of the pyrochlore phase at temperatures between 530 °C and 600 °C (Eq. (1.19)). Even though the pyrochlore subsequently reacts with MgO to form the perovskite PMN, some pyrochlore remain in the mixture. The low reactivity of magnesium oxide and its low weight fraction in the PbO-MgO-Nb_2O_5 mixture are additional impediments to obtaining single-phase perovskite.

$$3PbO + 2Nb_2O_5 \xrightarrow{530-600\ ^\circ C} Pb_3Nb_4O_{13}\ \text{(cubic pyrochlore)}, \tag{1.19}$$

$$Pb_3Nb_4O_{13} + PbO \xrightarrow{600-700\ ^\circ C} 2Pb_2Nb_2O_7\ \text{(rhombohedral pyrochlore)}, \tag{1.20}$$

$$\begin{aligned} 3Pb_2Nb_2O_7 + MgO \xrightarrow{700-800\ ^\circ C} & 3Pb(Mg_{1/3}Nb_{2/3})O_3\ \text{(perovskite)} \\ & +\ Pb_3Nb_4O_{13}\ \text{(cubic pyrochlore)}. \end{aligned} \tag{1.21}$$

In order to avoid or at least to suppress the amount of pyrochlore phase in PMN, Swartz and Shrout [77] proposed a new synthesis method, denoted as the columbite synthesis, where the undesired reaction between PbO and Nb_2O_5 is avoided. In the first step a columbite precursor $MgNb_2O_6$ is synthesized:

$$MgO + Nb_2O_5 \xrightarrow{1000\ ^\circ C} MgNb_2O_6\ \text{(columbite)}. \tag{1.22}$$

In the second step, the PbO reacts with $MgNb_2O_6$ to form the perovskite phase:

$$MgNb_2O_6 + 3PbO \xrightarrow{900\ ^\circ C} 3Pb(Mg_{1/3}Nb_{2/3})O_3\ \text{(perovskite)}. \tag{1.23}$$

The columbite synthesis has also been successfully applied for the synthesis of PMN-PT ceramics [78]. Here, in the second step, both PbO and TiO_2 are added to the $MgNb_2O_6$. The reaction between equimolar amounts of PbO and TiO_2 occurs at as low as 360 °C and results in the formation of the perovskite $PbTiO_3$ [5].

1.3.3.2 Mechanochemical Synthesis

In mechanochemical synthesis or high-energy milling a powder mixture is subjected to high-energy collisions with the milling bodies. The mechanochemical reactions are promoted by the energy transferred from the milling bodies to the particles [79], [80].

Baek et al. [81] prepared a single perovskite PMN-10PT from a 100 g of PbO-$Mg(OH)_2$-Nb_2O_5-TiO_2 powder mixture by mechanochemical synthesis in a multi-ring-type mill, operating at 1850 rpm for 1 h, and subsequent calcination at 850 °C for 4 h. Lower temperatures or times of the calcination yields also the pyrochlore phase.

Later Wang et al. prepared the perovskite PMN-10PT [82] and PMN [83] from a mixture of PbO, MgO, Nb_2O_5 and (TiO_2) by mechanochemical treatment only in a high-energy shaker mill at 900 rpm for 20 h. The authors explained that first the crystallite-size refinement and partial amorphisation of the mixture take place. The reaction product is formed from the activated mixture and, with further milling, its amount increases. Interestingly, the authors did not observe the formation of the pyrochlore phase, which typically takes place in the conventional mixed-oxide synthesis (see Eq. (1.19)-(1.21)). They suggested that the crystallization of the perovskite phase occurs directly via nucleation and subsequent growth from the activated amorphous matrix.

The reaction mechanism of the PMN [84] was later investigated by Kuščer et al. The PbO–MgO–Nb_2O_5 powder mixtures were mechanochemically synthesized in a planetary mill for ~60 h.[12] The powders were characterized by X-ray powder diffraction (XRD) and Rietveld refinement analysis. Similar to Wang et al. [82], [83], they observed the particle size reduction and amorphisation in the initial stage. However, unlike Wang et al., who observed that the perovskite phase formed directly from the powder mixture, Kuščer et al. detected the intermediate pyrochlore phase, see Figure 1.14. It can be seen that after 8 h of milling, the amount of crystalline oxides decreases due to the partial amorphisation and the reaction. The reaction products were the cubic pyrochlore $Pb_{1.86}Mg_{0.24}Nb_{1.76}O_{6.5}$ and a small amount of the perovskite phase, hence it was suggested that both phases form simultaneously. Upon further milling, after 16 h, the concentration of the pyrochlore phase reached a maximum, while the amount of the perovskite phase gradually increased. The authors showed that the quantity and the composition of the amorphous phase changed during milling indicating that it takes part in the reactions yielding both the perovskite and pyrochlore phases. Furthermore, it was shown that after a certain time of milling, when the initial oxides could no longer be identified and there was no MgO in the amorphous phase, a significant decrease in the formation rate of the perovskite phase was observed.

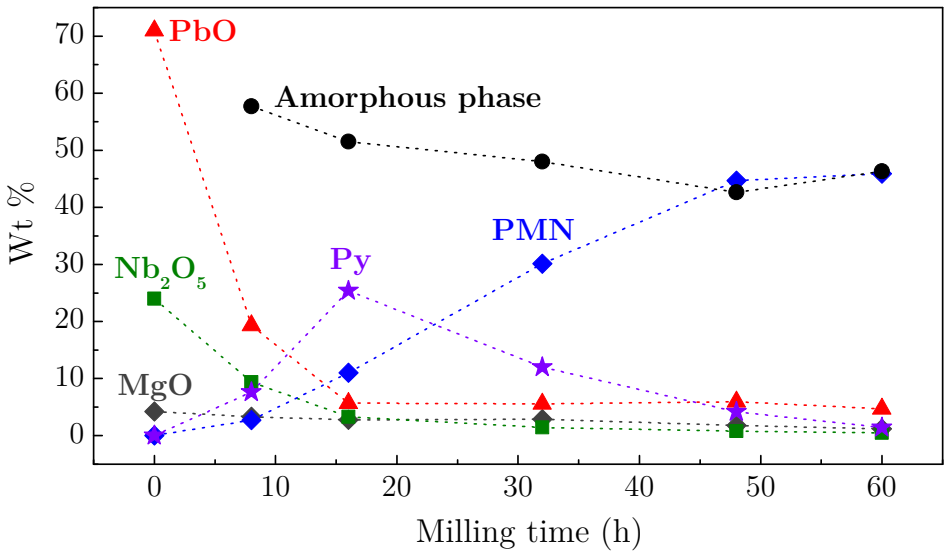


Figure 1.14: Quantities of individual phases as a function of the milling time for a powder mixture with a stoichiometry corresponding to PMN determined by Rietveld refinement analysis. The fraction of the amorphous phase was determined by an internal standard. Py – pyrochlore. Dashed lines are a guide for the eye. After [84].

[12] A vial was filled with a total of 200 g of the powder mixture and 15 WC balls with a diamater of 20 mm. The high-energy milling was performed at 300 rpm.

The authors assumed that the perovskite could not nucleate from the amorphous phase and that the perovskite phase formed via the pyrochlore-to-perovskite transformation, in a way similar to the conventional solid-state synthesis. A later study by Kuščer et al. [85] confirmed that the mechanism of mechanochemical synthesis of PMN-35PT was analogous to that of PMN.

1.4 Electrocaloric Effect in (1-x)Pb($Mg_{1/3}Nb_{2/3}$)O_3-x$PbTiO_3$ Perovskite Ceramics

The EC effect is directly related to polarization change as a function of temperature and electric field; therefore, it is especially strong in ferroelectric and relaxor materials [29]–[33]. The PMN-PT solid solution for x≤0.35 represents one of the potential EC material groups due to its excellent dielectric properties, such as high dielectric permittivity and polarization, and a large change of polarization with temperature [32], [86]–[90]. Another significant advantage of PMN-PT materials is that the position of the dielectric anomaly is altered over a wide temperature range in the vicinity of T_{room} by changing the concentration of PT, i.e., from around -8 °C (T_m of a PMN) to ~170 °C (T_m of PMN-35PT) [10]. Since the largest EC effect is expected to be in the vicinity of the dielectric anomaly, the temperature range of the maximum EC effect can be tuned by changing the concentration of PT [88].

In the literature we can find several studies of the EC effect in PMN-PT bulk ceramics, single crystals, thick and thin films. In Table 1.2-1.4 some recently reported ΔT_{EC} are collected, together with the most important measurement and sample parameters, with regard to the material form. Note that the following text is a brief overview of these tables, while the EC behavior, i.e., ΔT_{EC} as a function of E and T for selected PMN-PT compositions is discussed later in this section.

From Table 1.2, where the EC data for bulk ceramics and single crystals are collected, it can be seen that the single crystals were prepared by the Bridgman method, while the ceramics were prepared by solid-state or mechanochemical synthesis. The overview of the reported ΔT_{EC} values reveals that they range from about 0.5 °C to about 2.5 °C, and the EC coefficients from approximately 1.5×10^{-7} m°C/V to almost 6×10^{-7} m°C/V, respectively. Note that the ΔT_{EC} values were obtained at different temperatures and electric field amplitudes. In addition, the measurements were carried out by using different methods and equipment, and on the samples with thicknesses from 60 µm to 1000 µm.

Table 1.3 includes the only two EC data on PMN-PT thick films, published by the same research group [91], [92]. In these studies ~60-µm-thick samples were prepared by screen printing and the EC effect was measured directly in a high-resolution calorimeter. The PMN-30PT possesses a 1.0 °C larger ΔT_{EC} than the PMN-35PT (ΔT_{EC} = 1.8 °C) at a temperature of ~155 °C and an electric field of ~85 kV/cm. The EC coefficients are similar to those of bulk ceramics.

The PMN-PT thin films, collected in Table 1.4, were prepared by different deposition methods, i.e., by chemical solution and by physical vapor deposition, and had thicknesses between 200 nm and 260 nm. In all cases the reported ΔT_{EC} were calculated from the $P-E$ measurements. Note that the $P-E$ measurements were performed at different frequencies. There are three PMN-PT thin-film compositions, PMN-32PT, PMN-33PT and PMN-35PT, all prepared by physical vapor deposition, the EC response of which can be credibly compared due to the similar measurement conditions, T = 140–145 °C and E = 600–747 kV/cm.

Table 1.2: Some reported EC data for PMN-PT bulk ceramics.

Composition	Form	Synthesis method	T (°C)	ΔT_{EC} (°C)	E (kV/cm)	$\Delta T_{EC}/E$ (10^{-7}m°C/V)	d (µm)	Measurement method	Ref.
PMN	Cer	MCS	67	2.56	90	2.84	60-100	HRC	[88]
PMN	Cer	SS	69	1.42	90	1.56	100-130	DTR	[89]
PMN-5PT	Cer	SS	68	1.14	50	2.28	100-130	DTR	[89]
PMN-8PT	Cer	SS	30	0.58	20	2.90	1000	DSC	[93]
PMN-8PT (Mn)*	Cer	SS	55	0.35	20	1.75	1000	DSC	[93]
PMN-10PT	Cer	SS	50	0.45	29	1.55	500	DTR	[86]
PMN-10PT§	SC <111>	BM	55	1	40	2.50	600	IM (1 Hz)	[90]
PMN-10PT	Cer	SS	89	1.19	50	2.38	100-130	DTR	[89]
PMN-13PT§	Cer	SS	70	0.56	24	2.33	1000	DTR	[94]
PMN-15PT	Cer	SS	124	1.28	50	2.56	100-130	DTR	[89]
PMN-20PT	Cer	SS	141	1.41	50	2.82	100-130	DTR	[89]
PMN-25PT	Cer	SS	110	0.9¥	25	3.60	1000	DSC	[95]
PMN-25PT§	SC <111>	BM	100	1.2¥	25	4.80	1000	DSC	[95]
PMN-25PT	Cer	SS	146	1.30	50	2.60	100-130	DTR	[89]
PMN-28PT	SC <011>	BM	130	0.53	9	5.89	1000	DTR	[96]
PMN-30PT	Cer	SS	183	1.53	50	3.06	100-130	DTR	[89]
PMN-30PT	Cer	MCS	157	2.70	90	3.00	60-100	HRC	[88]
PMN-35PT	Cer	MCS	164	1.71	57	3.00	60-100	HRC	[22]
PMN-35PT	Cer	MCS	107	0.94	60	1.57	60-100	HRC	[97]

Cer – ceramics, SC <hkl> – single crystal of <hkl> plane

BM – Bridgman method, MCS – mechanochemical synthesis, SS – solid-state synthesis

DSC – differential scanning calorimetry, DTR – direct temperature reading by thermocouple, HRC – high-resolution calorimetry, IM (ν) – indirect measurement (frequency), *Mn-doped (3 mol%), §Data also reported in the review article [32]. ¥Calculated from the Q data using the c_E see Appendix B.

Table 1.3: Some reported EC data for PMN-PT thick films.

Composition	Synthesis method	T (°C)	ΔT_{EC} (°C)	E (kV/cm)	$\Delta T_{EC}/E$ (10^{-7}m°C/V)	d (µm)	Measurement method	Ref.
PMN-30PT§	SP	160	2.8	90	3.11	50-70	HRC	[92]
PMN-35PT§	SP	154	1.8	80	2.25	40-70	HRC	[91]

SP – screen printing, HRC – high-resolution calorimetry

§ - Data also reported in the review article [32].

Table 1.4: Some reported EC data for PMN-PT thin films.

Composition	Deposition method	T (°C)	ΔT_{EC} (°C)	E (kV/cm)	$\Delta T_{EC}/E$ (10^{-7}m°C/V)	d (nm)	Measurement method	Ref.
PMN-7PT§	CSD	25	9	723	1.25	210	IM (0.1 kHz)	[98]
PMN-10PT§	CSD	75	5	895	0.55	260	IM (10 kHz)	[99]
PMN-32PT§	PVD	145	13.4	600	2.23	200	IM (0.1 kHz)	[100]
PMN-33PT§	PVD	145	14.5	600	2.41	200	IM (1 kHz)	[101]
PMN-35PT§	PVD	140	31	747	4.15	240	IM (0.2 kHz)	[102]

CSD – chemical solution deposition, PVD – physical vapor deposition

IM (ν) – indirect measurement (frequency)

§ - Data also reported in the review article [32].

Due to different synthesis and measurement methods, sample and measurement parameters, a comparison of the ΔT_{EC} values is rather difficult and can be credibly compared in only rare cases. However, some general trends can be observed. Bulk ceramics, single crystals and thick films exhibit a ΔT_{EC} of up to a few degrees, which is much lower than in thin films. One of the main reasons for the high EC response of thin films is their high dielectric breakdown strength E_b, which approaches 10^3 kV/cm, resulting in a giant ΔT_{EC} of a few tens of degrees. Bulk ceramics, single crystals and thick films, on the other hand, possess an order of magnitude lower E_b, below 10^2 kV/cm, resulting in a ΔT_{EC} of a few degrees. Note, however, that thin films possess substantially lower EC coefficients (2.1×10^{-7}m°C/V) than bulk ceramics and single crystals (2.8×10^{-7}m°C/V).

Another important fact that can be recognized from these EC studies is that quite different values of ΔT_{EC} are reported for the same materials, for example, compare the data for PMN in Table 1.2. Here, it should be noted that in most EC studies the material properties, such as the phase composition and microstructure, are often not reported, even though their impact on the dielectric properties is significant and well known.

As mentioned before, the relaxor PMN-PT compositions, i.e., with $0 \leq x \leq 0.3$, do not possess any long-range ferroelectric order at zero-electric field. However, at temperatures below the critical point in the $E - T$ phase diagram a high enough electric field irreversibly induces the long-range rhombohedral order. This first-order relaxor-to-ferroelectric phase-transition is accompanied by a high entropy change, hence a high EC effect is expected.

In the literature two recent EC studies of the PMN and PMN-30PT ceramics can be found. Rožič et al. [88] prepared the PMN and PMN-30PT ceramics by mechanochemical synthesis. The PMN and PMN-30PT materials were single-phase perovskite with respective relative densities of 94 % and 97 %. Peräntie et al. [89] prepared the ceramic samples by the columbite synthesis. The materials were single-phase perovskite with a relative density above 95 %. The EC temperature change was directly measured in both cases, see Table 1.2. The results of the EC measurements for PMN (a, b) and PMN-30PT (c, d) ceramics are shown in Figure 1.15. We can observe the following trends:

i) In all cases the ΔT_{EC} increases with the electric field and temperature. However, in PMN the ΔT_{EC} shows a very weak temperature dependence at lower electric fields, i.e., up to ~25 kV/cm, which becomes more pronounced at higher electric fields. In PMN-30PT ceramics, on the other hand, the ΔT_{EC} shows a stronger temperature dependence already at low fields, which becomes gradually stronger with higher fields.

ii) At a selected electric field the maximum ΔT_{EC} occurs at a lower temperature in PMN than in PMN-30PT ceramics. This is directly related to the respective dielectric permittivity peak position, see Figure 1.10.

iii) The maximum ΔT_{EC} shifts towards higher temperatures with increasing electric field amplitude. This shift is schematically denoted with red arrows in Figure 1.15, and is even more apparent in the EC results, reported by Peräntie et al. [89] due to a higher density of the measurement data. The upward shift of the maximum ΔT_{EC} corresponds to the shift of the induced relaxor-to-ferroelectric phase transition (see the $E - T$ phase diagram in Figure 1.4) [88]. As already mentioned, considerable differences between the reported ΔT_{EC} values can be observed in some cases. This is indeed the case for PMN ceramics, where the highest measured ΔT_{EC} is 2.56 °C and 1.54 °C at 90 kV/cm and ~68 °C, as reported by [88] and [89], respectively (compare Figure 1.15 (a) with (b)). In contrast, the EC response of PMN-30PT is in a good agreement in both studies, e.g., the ΔT_{EC} is ~1.5 °C at the highest comparable electric field of ~55 kV/cm and ~165 °C. Disagreement and agreement of the ΔT_{EC} magnitude in PMN and PMN-30PT does not necessarily bring into question the reliability of the authors' measurement equipment or measurement procedure, but it could indicate a possible influence of the material properties on the EC effect.

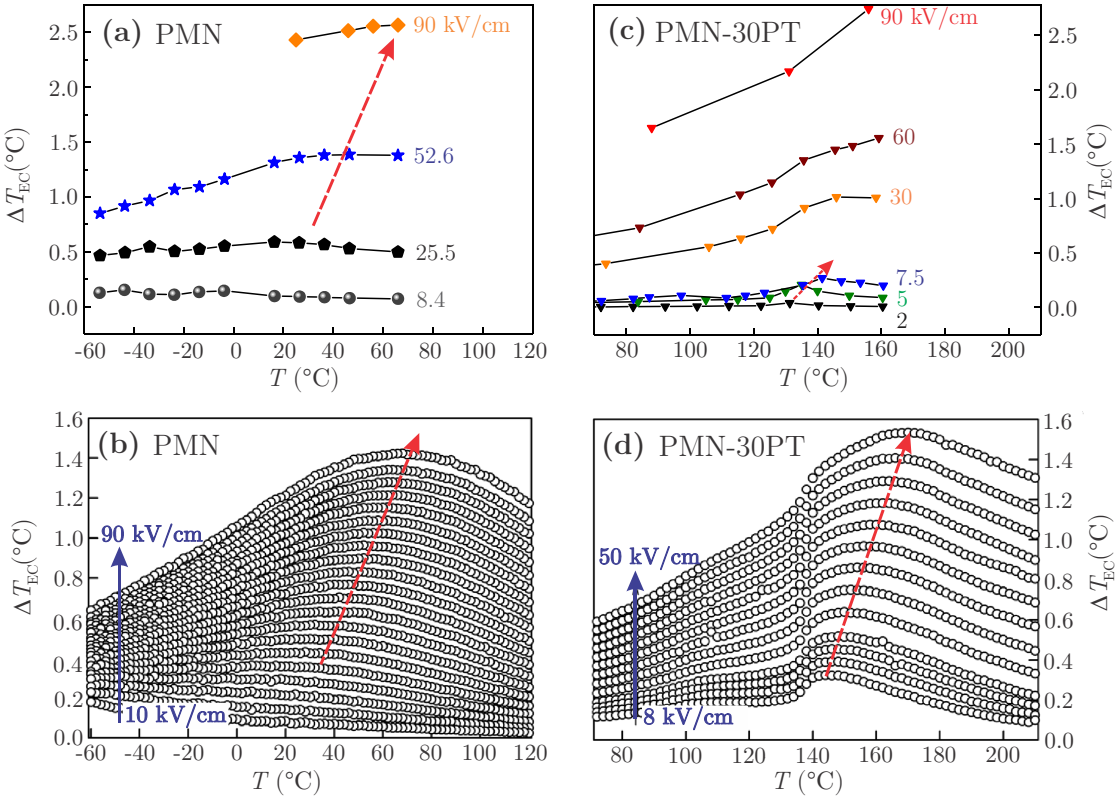


Figure 1.15: The EC temperature change ΔT_{EC} vs. E and T for (a, b) PMN and (c, d) PMN-30PT ceramics: (a, c) after [88] and (b, d) after [89]. The red arrow denotes the upward shift of the maximum value of the ΔT_{EC} with increasing E. The temperature range in (a) and (c) is rescaled so that it is comparable to the ones in (b) and (d). Note the different y-scales of (a, b) and (c, d).

Chapter 2

Aims and Hypothesis

The (1-x)Pb($Mg_{1/3}Nb_{2/3}$)O_3-x$PbTiO_3$ (PMN-100xPT) solid solution with x≤0.35 has been widely studied for its excellent dielectric and piezoelectric properties, and recent studies have also shown that the compositions exhibiting the dielectric permittivity maximum close to room temperature, such as PMN-10PT, exhibit a great potential for electrocaloric (EC) applications. Although it has been generally accepted that the microstructure crucially influences the dielectric properties of perovskite ferroelectric and relaxor ferroelectric ceramic materials, the correlations between the microstructure and EC phenomena have not yet been explored. As very high electric field amplitudes (>50 kV/cm) are needed to achieve large EC temperature changes (ΔT_{EC}), the dielectric breakdown strength of selected materials should be considered.

In the first three chapters of this thesis we address the influence of the microstructure on the EC properties of the PMN-10PT ceramics prepared by the mechanochemical and columbite powder-synthesis routes. Based on the hypothesis that the microstructural descriptors influence the EC response of the PMN-10PT ceramics we have formulated our aims:

- To investigate and to explain the influence of the microstructure, i.e., the grain size in the micrometer range and the chemical composition, on the EC properties of the PMN-10PT ceramics, prepared by both, mechanochemical and columbite powder-synthesis routes.
- To study whether the synthesis method, mechanochemical and columbite, influences the EC properties of the PMN-10PT ceramics.

In the last part we discuss the energy efficiency of an EC cooling device. This topic has only rarely been discussed, yet it is of crucial importance from the application point of view. The influence of the polarization – electric field ($P-E$) hysteresis losses on the material's energy efficiency is addressed, and for this purpose, the PMN-10PT is compared with the prototype relaxor PMN and the morphotropic phase-boundary composition ferroelectric PMN-35PT. The electric energy recovery and its influence on the efficiency of an EC cooling system is analyzed. Our hypothesis has been that the energy efficiency of a cooling system is enhanced for the PMN-PT compositions with slim $P-E$ loops, i.e., with a pronounced relaxor character, and for a high degree of electric-energy recovery. The principal aim of this part is:

- To study the influence of the $P-E$ hysteresis losses and the electric-energy recovery on the coefficient of performance for a cooling system in which a PMN-100xPT ceramic (x=0, 0.1 and 0.35) is subjected to a thermodynamic cycle.

Chapter 3

Materials and Methods

3.1 Sample Preparation

3.1.1 Synthesis of the 0.9Pb($Mg_{1/3}Nb_{2/3}$)O_3-0.1$PbTiO_3$ Powders

The 0.9Pb($Mg_{1/3}Nb_{2/3}$)O_3-0.1$PbTiO_3$ (PMN-10PT) powders were synthesized from the constituent oxides, see Table 3.1. Prior to the synthesis, the MgO was milled in an attritor mill (Netzsch, PE 075/PR 01) at 600 rpm for 3 h in isopropanol, using yttria-stabilized zirconia (YSZ) balls with a diameter of 3 mm. After each wet-milling the powder was dried at 85 °C.

Table 3.1: Chemicals used during the synthesis of the PMN-10PT powders.

Name	Formula	Purity (%)	Supplier	Crystal system[§]	JCPDS[§]
Lead (II) oxide	PbO	99.9	Sigma-Aldrich	orthorhombic	77-1971
				tetragonal	85-1739
Magnesium (II) oxide	MgO	99.95	Alfa Aesar	cubic	77-2364
Niobium (V) oxide	Nb_2O_5	99.9	Sigma-Aldrich	orthorhombic	30-0873
Titanium (IV) oxide	TiO_2	99.8	Alfa Aesar	tetragonal	78-1509

[§]Determined by the XRD analysis as described in Section 3.2.3.

The particle sizes and the field-emission scanning electron microscope (FE-SEM) images of the oxides are collected in Table 3.2 and Figure 3.1, respectively. The characterization methods are described in Section 3.2.

The PbO consisted of disc-like particles with a median size of 0.82 µm. The as-received MgO consisted of about 1–20-µm-large agglomerates, and after milling in an attritor its d_{50} was reduced from 2.29 µm to 0.35 µm. The median particle sizes of Nb_2O_5 and TiO_2 were 0.34 µm and 0.21 µm, respectively.

Table 3.2: The particle sizes of constituent oxides used for the PMN-10PT synthesis.

Chemical formula	d_{10} (µm)	d_{50} (µm)	d_{90} (µm)
PbO	0.27	0.82	5.56
MgO (as-received)	0.51	2.29	8.81
MgO (milled)	0.21	0.35	0.83
Nb_2O_5	0.15	0.34	1.09
TiO_2	0.13	0.21	0.81

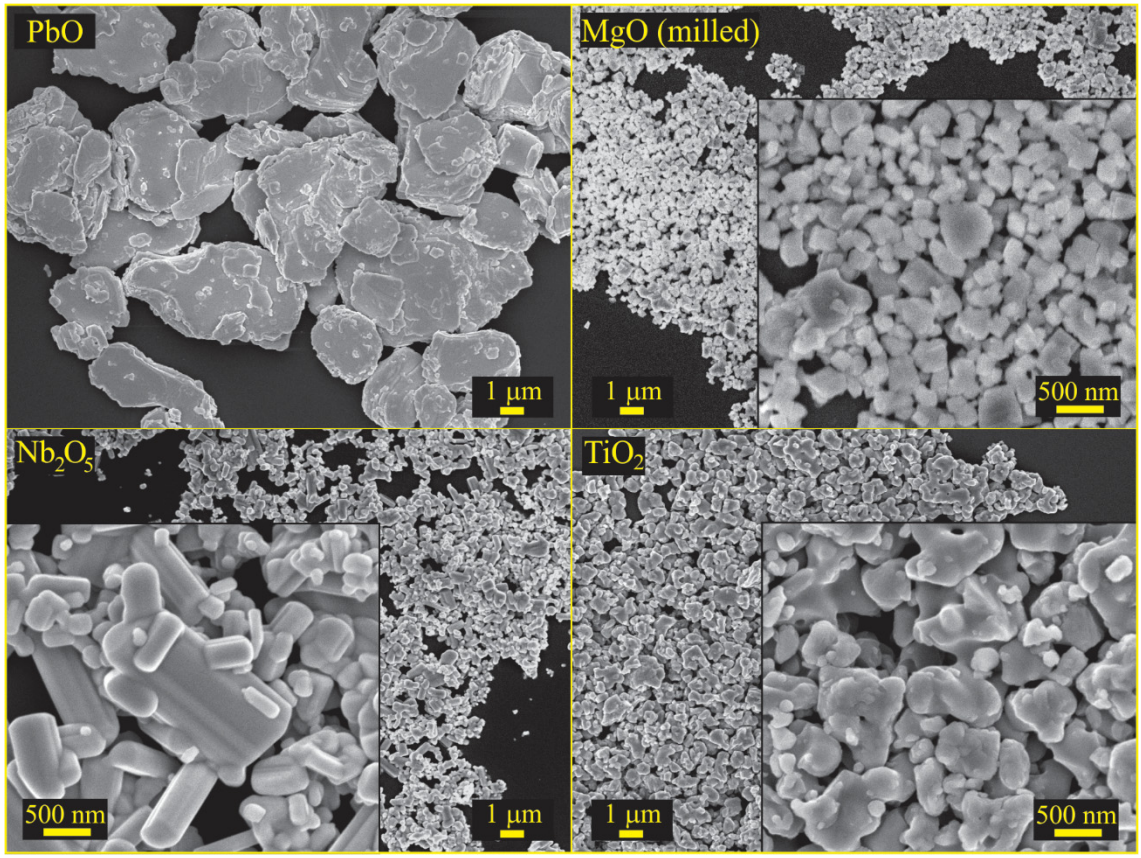


Figure 3.1: The FE-SEM images of the constituent oxides used for the PMN-10PT synthesis.

3.1.1.1 Mechanochemical Synthesis of PMN-10PT

The general scheme for the mechanochemical synthesis of the PMN-10PT powder is shown in Figure 3.2 (a). The stoichiometric powder mixture was first homogenized in a planetary mill (Retsch, PM 400) at 200 rpm for 2 h in isopropanol, using 10-mm YSZ balls and dried. The homogenized powder mixture was then mechanochemically synthesized in a planetary mill at 300 rpm for 96 h, using 20-mm tungsten carbide (WC) balls, milled in an attritor mill at 800 rpm for 4 h in isopropanol (3-mm YSZ balls) and dried.

3.1.1.2 Columbite Synthesis of PMN-10PT

The scheme of the columbite synthesis of the PMN-10PT powder is shown in Figure 3.2 (b). In the first step the MgO-Nb_2O_5 powder mixture was milled in an attritor mill (3 mm YSZ balls) at 800 rpm for 4 h in isopropanol and dried. The powder mixture was then placed in an alumina crucible with a lid and calcined in a chamber furnace at 1150 °C for 4 h. The heating and cooling rates were 5 °C/min. In the second step, both PbO and TiO_2 were added to $MgNb_2O_6$ in the molar ratio corresponding to the stoichiometry of the PMN-10PT, and the mixture was milled in the attritor mill under the same conditions as in the first step and dried. The as-prepared PbO-$MgNb_2O_6$-TiO_2 powder mixture was then calcined at 750 °C for 4 h (heating and cooling rates were 5 °C/min), milled in the attritor at 800 rpm for 4 h in isopropanol and dried.

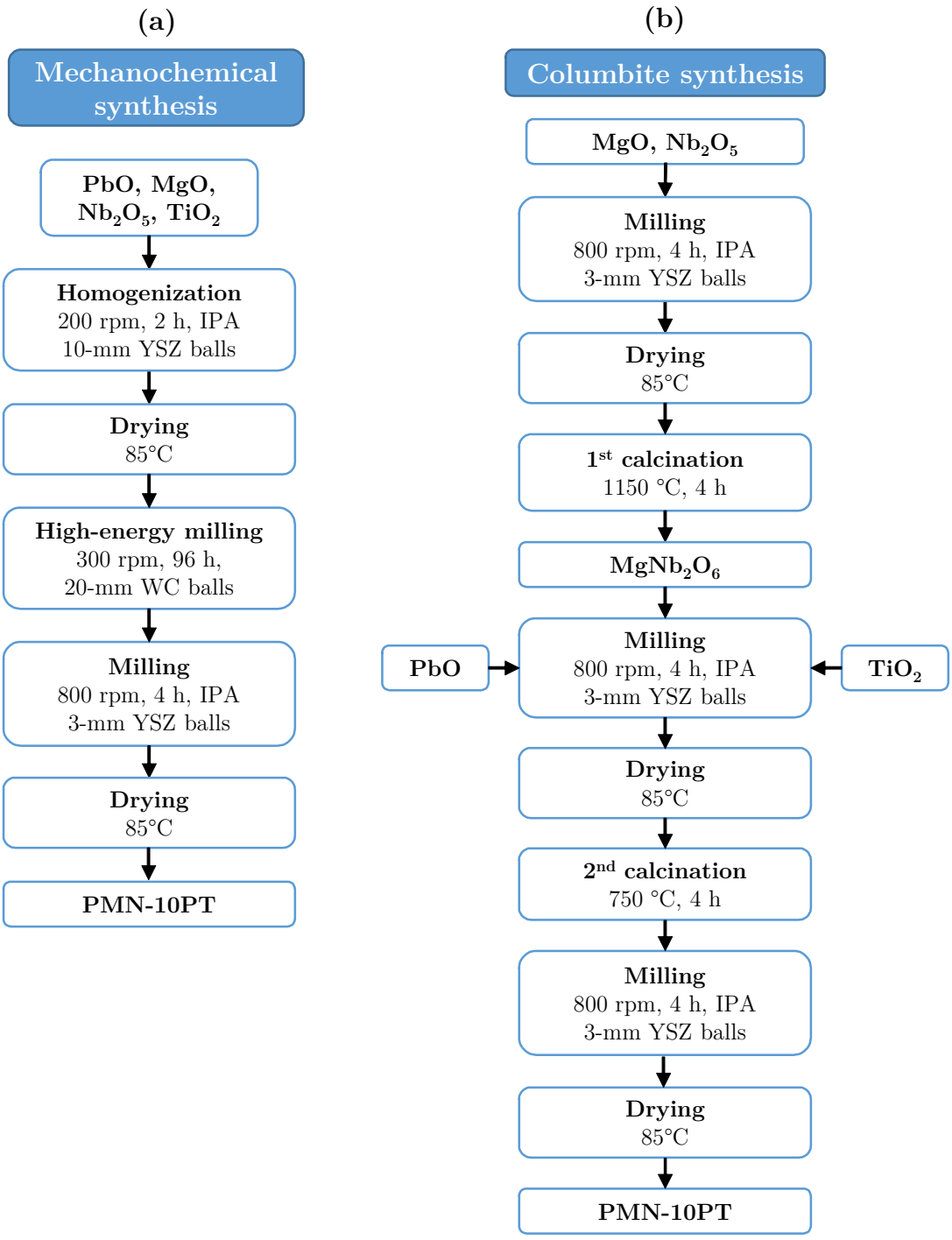


Figure 3.2: Schematic presentation of the (a) mechanochemical and (b) columbite synthesis of the PMN-10PT ceramic powder. IPA – isopropanol.

3.1.2 Sintering and Preparation for the Electrical Measurements

The powder compacts were pressed uniaxially at 50 MPa and then isostatically at 300 MPa, and sintered in double alumina crucibles in the presence of PMN-10PT packing powder. The mechanochemically synthesized PMN-10PT powder compacts were sintered

at 1100 °C for 2 h, at 1150 °C for 2 h, 1200 °C for 2 h and 16 h and at 1250 °C for 8 h and 16 h.

The PMN-10PT powder compacts, prepared by the columbite synthesis, were sintered at 1200 °C for 2 h. The heating and cooling rates were in all cases 2 °C/min. For the dielectric and direct EC measurements, the pellets were cut to a thickness of about 200 µm and 80 µm, respectively, polished, annealed at 600 °C for 1 h and cooled with a rate of 1 °C/min. The Cr/Au electrodes were deposited using RF-magneton sputtering (5 Pascal).

3.2 Characterization Methods

3.2.1 Thermogravimetric Analysis

The thermogravimetric analyses of the initial oxides were performed by using a Netzsch STA 409 analyzer. A total of about 50 mg of the sample was heated to approximately 1200 °C (750 °C in case of PbO) with a heating rate of 2 °C/min.

3.2.2 Particle Size and Particle Size Distribution Analysis

The particle sizes and particle-size distributions of the powders were analyzed with a static light-scattering method, using a laser granulometer (Microtrac S3500 Particle Size Analyzer). Prior to the measurements the powder samples were suspended in isopropanol and then placed in an ultrasound bath (Iskra Sonis 4) for a few minutes in order to break up the agglomerates. The powders are described with the area particle size distribution, the cumulative curve, and with the 90 % particle size limit (d_{90}), 50 % particle size limit (d_{50}), and 10 % particle size limit (d_{10}).

3.2.3 X-Ray Diffraction

The synthesized powders and sintered ceramics were analyzed with an X-ray diffractometer (X'Pert PRO MPD, PANalytical, Almeo) using Cu-Kα_1 radiation. Prior to the analysis the ceramics were pulverized in an agate mortar. The XRD patterns were recorded in the 2Θ-region from 10° to 70° using a 1D detector (X'Celerator, PANalytical, Almeo) with a capture angle of 2.122°. The exposure time for each step was 100 s and the interval between the obtained data points was 0.034°. The peak positions and their relative intensities were determined from the experimental patterns. The crystallographic cards from the JCPDS (Joint Committee on Powder Diffraction Standards) database were used for the qualitative analysis.

3.2.4 Inductively Coupled Plasma Spectroscopy

Quantitative elemental analyses of the powder were performed with inductively coupled plasma (ICP) mass spectroscopy using a quadrupole-based 7500 CE spectrometer. The measurements were made without a reference. Instead, an additional technique was used to verify the results, i.e., ICP atom emission spectroscopy using a Thermo Jarrel Ash Atomscan 25 spectrometer.

3.2.5 Dynamic Sintering Curves

The dynamic sintering curves of the powder compacts were recorded with a heating rate of 5 °C/min using an optical dilatometer (Leitz V. 1A, Leitz, Wetzlar). The dimensions of

the samples were continuously measured from the digitalized images and the relative shrinkage ($\Delta l/l$) was determined with the equation:

$$\left(\frac{\Delta l}{l}\right) = \frac{l_i - l_T}{l_i} \tag{3.1}$$

where l_i is the initial dimension of the sample at T_{room} and and l_T is the dimension of the sample at a selected temperature, respectively.

3.2.6 Specific Heat Capacity

The specific heat capacity c_E as a function of temperature of the ceramic samples was determined from the differential scanning calorimetry curves using a differential scanning calorimeter (DSC; Netzsch, DSC 204 F1). The samples of ~5 mm in diameter and a thickness of ~1 mm were put in Pt crucibles with lids, and heated in a calorimeter with a heating rate of 2 °C/min from 35 °C to 300 °C. Each measurement was repeated two times. Sapphire (Netzsch, diameter of 5.2 mm, thickness of 1 mm) was used as the standard material. The specific heat capacity of the sample was calculated from the measured DSC-curves according to:

$$c_E = c_E^{standard} \times \frac{DSC^{sample}}{DSC^{standard}} \tag{3.2}$$

where $c_E^{standard}$ is the specific heat capacity of a standard, and DSC^{sample} and $DSC^{standard}$ are the measured DSC curves of a sample and standard, respectively. The values of the $c_E^{standard}$ as a function T of were extracted from [103].

3.2.7 Density Measurements

The densities ρ of the sintered ceramics were measured with a gas-displacement density analyzer (Micromeritics, AccuPyc III 1340 Pycnometer) at room temperature. The obtained results represent an average of ten measurements. The relative densities (RD) of the ceramics were calculated using the theoretical density of PMN, i.e., 8.13 g/cm^3 (JCPDS 81-0861).

3.2.8 Microstructural Analysis

For the microstructural investigations with a FE-SEM (JEOL JSM-7600, equipped with a wavelength-dispersive X-ray spectrometer WDXS), the samples were cut with a diamond wire and polished to a 0.25-µm finish. For the grain-size and grain-size-distribution analysis an additional set of samples was prepared by thermal etching. The latter was carried out in a tube furnace by exposing the polished sample at a temperature approximately 300 °C below the sintering temperature. Prior to the analysis the samples were coated with a 4-nm-thick carbon coating in a Gatan PECS 682 to provide electrical conductivity and avoid any charging effects. For the stereological analysis more than 300 grains per sample were measured with the Image Tool Software [104]. The grain size is expressed as the Feret's diameter [105].

An analytical HR-TEM (JEOL JEM-2010F) was employed for the study of the microstructure on the nanoscale. For the HR-TEM investigations, the specimens were prepared by mechanical grinding, dimpling and finally Ar-ion milling.

WDXS was utilized to determine the chemical composition. The accelerating voltage was 20 kV. A <111> single crystal with the PMN-32PT composition was used as a

reference sample (APC International, Ltd. Mackeyville, PA) for the quantification of the Pb, Ti, Nb, and Mg contents. The X-ray intensities for the Pb-Lα spectral line were measured with a LIF (lithium fluoride) crystal, the Ti-Kα, Nb-Lα and Zr-Lα spectral lines were measured with a PET (pentaerythritol) crystal, and the Mg-Kα spectral line with a TAP (thallium acid phthalate) crystal. The oxygen was calculated from the stoichiometry. The obtained results represent the average of about ten measurements.

3.2.9 Dielectric Spectroscopy

The complex dielectric constant $\varepsilon^* = \varepsilon' - i\varepsilon''$ was measured in the temperature range from -50 °C to 150 °C at frequencies of 0.1, 1, 10, and 100 kHz using an Agilent E4980A Precision LCR meter. The amplitude of the probing ac electric signal was 1 V. After heating the sample up to 150 °C, the dc bias electric field was applied and then the dielectric response was measured during the cooling run with a rate of 1 °C/min. The temperature was stabilized to within $\pm$0.01 °C using a lock-in bridge technique with a Pt100 resistor as the thermometer.

3.2.10 Domain Structure Investigations

Prior to the domain-structure investigations the samples were cut with a diamond wire, polished to a 0.25-µm finish and fine polished for 2 h using a suspension consisting of 60 mL of OP-S silica colloidal suspension (Struers), 0.3 g of dissolved potassium hydroxide (Alfa Aeasar, 85 %), and 440 mL of deionized water. Afterwards, the samples were annealed at 600 °C for 1 h and then cooled with the rate of 1 °C/min.

The topography and the piezoresponse images were recorded with an atomic force microscope (AFM; Asylum Research, MFP-3D) equipped with a piezoresponse force mode (PFM). For scanning the sample surface a tetrahedral Si tip coated with conductive Ti/Ir layer (Asyelec-01, AtomicForce F&E GmbH) with the curvature diameter of 30 nm $\pm$ 10 nm was applied. The topographies and the out-of-plane amplitude PFM images were measured in the Dual AC Resonance Tracking mode at an ac amplitude signal of 40 V and a frequency of ~300 kHz.

After the investigations of the as-sintered samples the Ag-electrode paint (Ted Pella, Leitsilber 200 Silver Paint) was deposited on the sample surfaces and dried for 30 min. As-prepared samples were poled at room temperature using a dc electric field of 42 kV/cm, applied for 15 min. After the poling process the electrodes were removed using acetone. The poled samples were aged for 24 h and reinvestigated by PFM.

3.2.11 Electrocaloric Measurements

3.2.11.1 Indirect Electrocaloric Measurements

For the indirect EC measurements the $P - E$ hysteresis loops were measured with an Aixacct TF analyzer 2000 in the temperature range from T_{room} to 140 °C with a step of 5 °C. The applied electric signal was sinusoidal and the frequency was 1 Hz. The ΔT_{EC} was calculated via Eq. (1.13), as described in Section 1.2.3.1. For the calculation the specific heat capacity c_E and the density of the investigated sample were used. The c_E was measured with the DSC (see Section 3.2.6) as a function of temperature at zero electric field. The field dependence of the heat capacity was neglected, while its temperature dependence was taken into account.

3.2.11.2 Direct Electrocaloric Measurements

For the direct EC measurements a modified high-resolution calorimeter, which allows a precise temperature stabilization of the bath, i.e., within ±0.1 mK was employed. The temperature of the sample was followed by measuring the resistance of a micro-bead thermistor, which was attached to the sample, together with electrical contacts (50 µm thick Au wires) as shown in Figure 3.3.

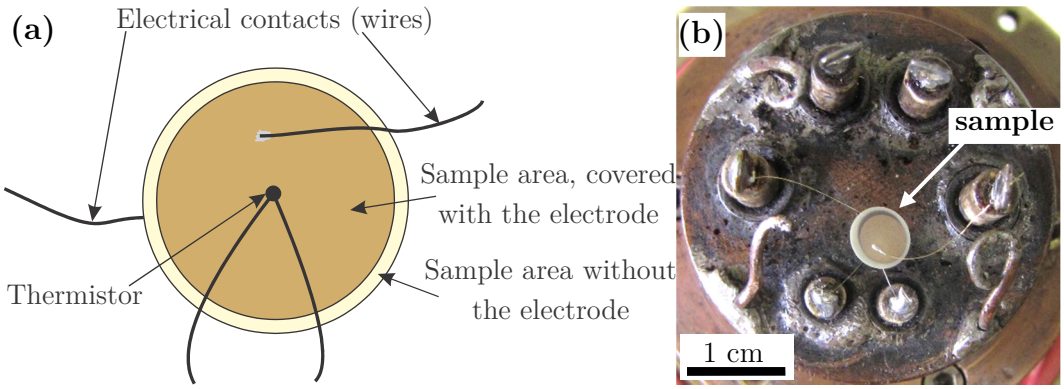


Figure 3.3: (a) Schematic representation of the prepared sample for direct EC measurements. (b) Mounted sample in the calorimeter's head. (Thermistor is on the bottom side of the sample).

The calorimeter setup consists of a high-voltage generator (Kepco BOP 1000M), an arbitrary signal generator (Krohn-Hite Corporation Arbitrary Waveform Generator 5920), a digital multimeter (Keithley 2002 Multimeter), a temperature controller (LakeShore 340 Temperature Controler) and a computer. The high-voltage generator is driven and the digital multimeter is triggered by the arbitrary signal generator. The digital multimeter measures the resistance of the platinum resistance thermometer-Pt100 (mounted in the Cu block, which encloses the sample) and the resistance of the thermistor attached to the sample. The latter data are then recorded by a computer, which also controls the temperature controller of the surrounding bath temperature. The flexible heater attached around the Cu block enables a precise temperature stabilization. The shape of the applied electric pulse is controlled by the computer via the arbitrary signal generator. More details about the calorimeter setup can be found in [44].

In the direct EC experiment a step electric signal was used. The rise and fall times of the pulse were less than 200 µs. The length of the pulse was ~5 min, so that the sample temperature completely relaxed back to the bath temperature. The ΔT_{EC} was determined by taking into account the masses and heat capacities of the passive components, such as of the thermistor, wires, silver glue and the part of the sample without the electrode. The ΔT_{EC} was calculated using the equation:

$$\Delta T_{EC} = \Delta T_{meas} \frac{\sum_i m^i c_E^i}{m^a c_E^a} \tag{3.3}$$

where ΔT_{meas} is the actual measured temperature change, m^i and c_E^i are the mass and specific heat capacity for each of the ″passive components″ (thermistor, sample without electrode, etc.), and m^a and c_E^a are the mass and specific heat capacity for the active material, i.e., sample with the electrode.

3.2.12 Study of the Energy Efficiency of an EC Cooling System Employing xPb($Mg_{1/3}Nb_{2/3}$)O_3-(1-x)$PbTiO_3$ Ceramics[13]

The energy efficiency and electric-energy recovery analysis was performed for an EC cooling system employing PMN-100xPT ceramics with x = 0, 0.1 and 0.35. The PMN-PT ceramic powders were synthesized by mechanochemical synthesis. The PMN-10PT composition was prepared as described in Section 3.1.1.1, while the details of the preparation of the PMN and PMN-35PT powders can be found in [88] and [97], respectively. The powder compacts were prepared as described in Section 3.1.2. Sintering was performed at 1200 °C for 2 h in the packing powder. The heating and cooling rates were 2 °C/min.

The work done on the EC material, i.e., the work that is needed to charge the EC material, and the work that can be recovered by discharging the EC material were calculated from the $P(E)$ measurements. The latter were performed by the Aixacct TF analyzer 2000 at 27 °C with a unipolar triangular electric signal with the rise and fall times of 50 ms (Figure 3.4). Ten or more cycles were applied to the sample so that reproducible *P(E)* measurements were obtained.

The heat that can be absorbed or released from an EC system, in which the PMN-PT ceramic is subjected to a thermodynamic cycle, was calculated by using the experimental c_E and ΔT_{EC} data. The former were determined by DSC (see Section 3.2.6), while the latter were obtained from direct EC measurements in a high-resolution calorimeter (for PMN-10PT see Section 3.2.11.2). The EC data for PMN and PMN-35PT were taken from [88] and [97], respectively.

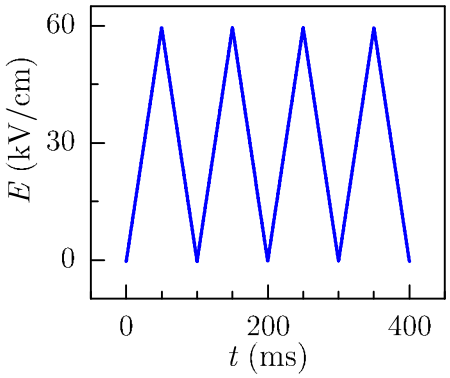


Figure 3.4: Applied electric signal during the $P(E)$ measurements of PMN-PT ceramics.

[13] The analysis was made in collaboration with Uroš Plaznik, Prof. Alojz Poredoš and Assoc. Prof. Andrej Kitanovski from the University of Ljubljana, Faculty of mechanical engineering, Laboratory for refrigeration and district energy. The results of the analysis were published in a common paper [97].

Chapter 4

Results and Discussion

4.1 Electrocaloric Response of the Mechanochemically Synthesized $0.9Pb(Mg_{1/3}Nb_{2/3})O_3$-$0.1PbTiO_3$ Ceramics with Different Grain Sizes

The goal of this section is to investigate the EC effect of PMN-10PT ceramics with grain sizes in the micron range, prepared from mechanochemically synthesized powder. The section begins with the characterization of the PMN-10PT powder and it continues with a phase composition and microstructure analysis of the ceramics with different grain sizes. The next part is devoted to investigations of the dielectric properties, while the last part completes the section with a study of the EC effect as a function of temperature, electric field and grain size.

4.1.1 Phase Composition and Microstructure

The PMN-10PT ceramic powder was prepared by mechanochemical synthesis as described in Section 3.1.1.1. According to the XRD analysis (Figure 4.1) all the peaks of the as-synthesized powder correspond to the perovskite phase. Note that the crystallographic data for PMN-10PT do not exist in the JCPDS database so the best match could be obtained with the JCPDS 81-0861 card for cubic PMN phase.

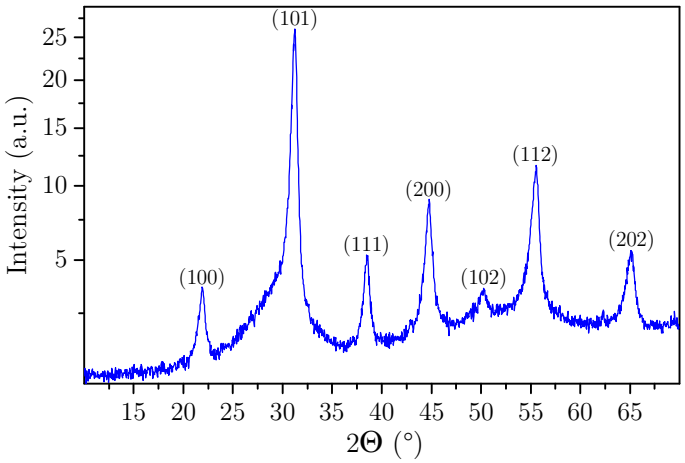


Figure 4.1: XRD pattern of the PMN-10PT powder after 96 h of high-energy milling. All the peaks correspond to the perovskite phase (JCPDS 81-0861). Note the square root y-scale.

Broad diffraction peaks and a high background in the XRD pattern (Figure 4.1) indicate the fine size of the crystallites and the presence of the amorphous phase in the powder. This is in a good agreement with previous studies of the mechanochemically synthesized PMN-PT [82]–[85], [106]. Wang et al. [83] estimated that the crystallite size in the mechanochemically synthesized PMN is ~15 nm. Kuščer et al. showed with a Rietveld refinement that the mechanochemically synthesized PMN [84] contained about 50 % of the amorphous phase, while in PMN-35PT the amount of the amorphous phase was about 10 % lower [85].

The quantitative chemical analysis of the PMN-10PT powder confirmed the presence of W and Zr in concentrations of 236 mg/kg and 52 mg/kg, respectively, see Table 4.1. Note that the amount of Co was below the detection limit. The contamination of PMN-10PT powder with the W and Zr is a consequence of the wear of the milling vial and the balls during the high-energy and attrition milling. A possible influence of the contaminants on the functional properties of PMN-10PT is discussed in Section 4.3.

Table 4.1: Concentrations of contaminants in the PMN-10PT powder due to the wear of the milling bodies, determined by the ICP spectrometry.

	Concentration	
Element	(mg/kg)	(%)*
Co	<25§	-
W	236	0.04
Zr	52	0.02

*mole of contaminant per mole of PMN-10PT (in %)
§below the detection limit

In Figure 4.2 (a) the FE-SEM micrographs of the milled PMN-10PT powder are shown. The powder consists of particles ranging from about 100 nm to about micron size. The lower-magnification image reveals that the particles form loose agglomerates with sizes up to approximately 5 µm. The particle size distribution (Figure 4.2 b) reveals a narrow size distribution with the median particle size d_{50} equal to 0.31 µm. The results are in agreement with the FE-SEM investigations.

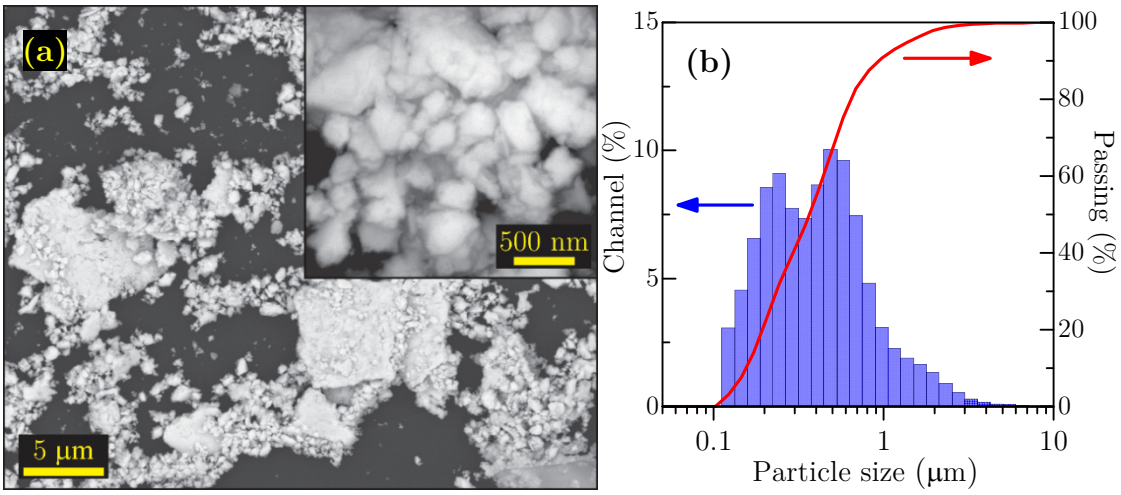


Figure 4.2: (a) FE-SEM micrograph and (b) particle size distribution of the PMN-10PT powder, prepared by mechanochemical synthesis, after attrition milling.

The PMN-10PT compacts were investigated by recording the dynamic sintering curves using an optical dilatometer (Figure 4.3). The sample shrinks slightly from 200 °C to ~430 °C. After reaching the plateau at ~490 °C it expands slightly up to ~770 °C. Between ~950 °C and ~1280 °C a steep slope in the shrinkage curve is observed. At about 1310 °C the material starts to melt, which is in a good agreement with the reported melting point of 1318 °C [107].

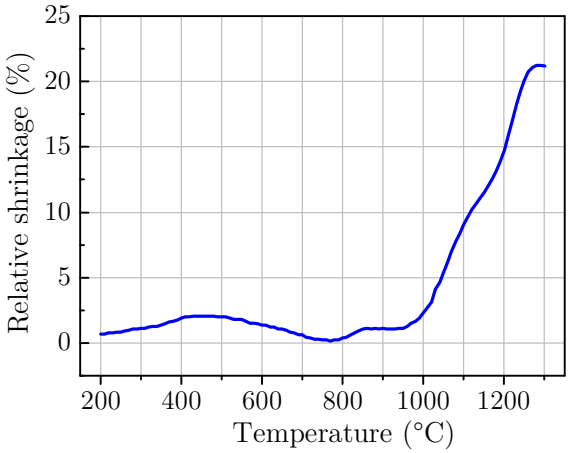


Figure 4.3: Dynamic sintering curve of the mechanochemically synthesized PMN-10PT powder compact. The heating rate was 5 °C/min.

In order to obtain ceramics with different grain sizes the samples were sintered at different temperatures and times, i.e., at 1150 °C for 2 h, at 1200 °C for 2 h and 16 h, and at 1250 °C for 8 h and 16 h. Note that sintering at 1050 °C and 1100 °C for 2 h was also performed and it resulted in ceramic samples with a high RD of ~97 %. The latter samples had similar grain sizes to the one sintered at 1150 °C, and were not included in our study. On the other hand, sintering at temperatures >1250 °C was not carried out because it might result in significant lead-oxide losses [75].

The X-ray powder diffraction patterns of the crushed ceramic pellets are presented in Figure 4.4 (a). All the samples contained only the perovskite phase (JCPDS 81-0862).

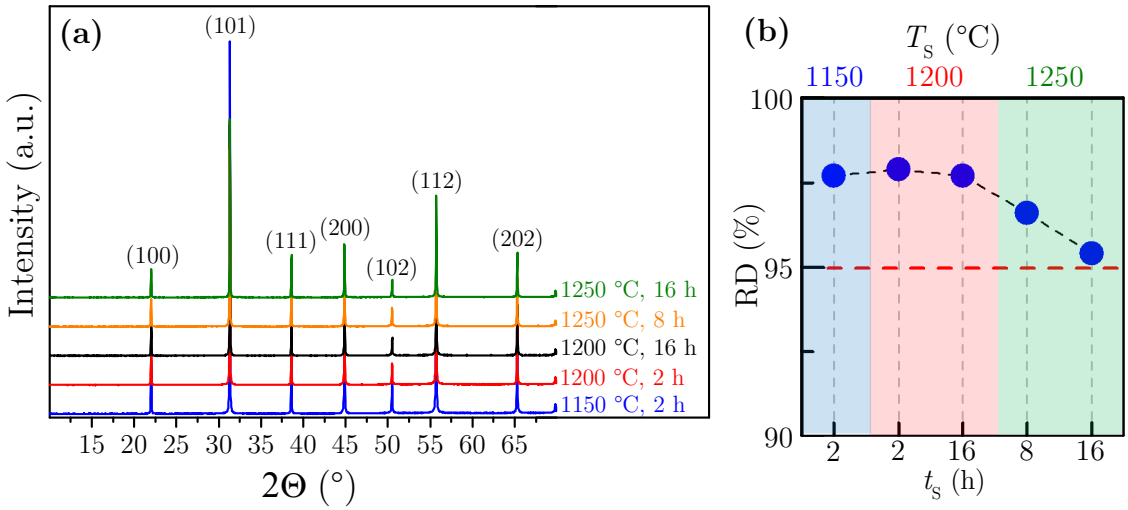


Figure 4.4: (a) XRD patterns and (b) relative densities (RD) of the sintered PMN-10PT ceramics, prepared from the mechanochemically synthesized powder (JCPDS 81-0861).

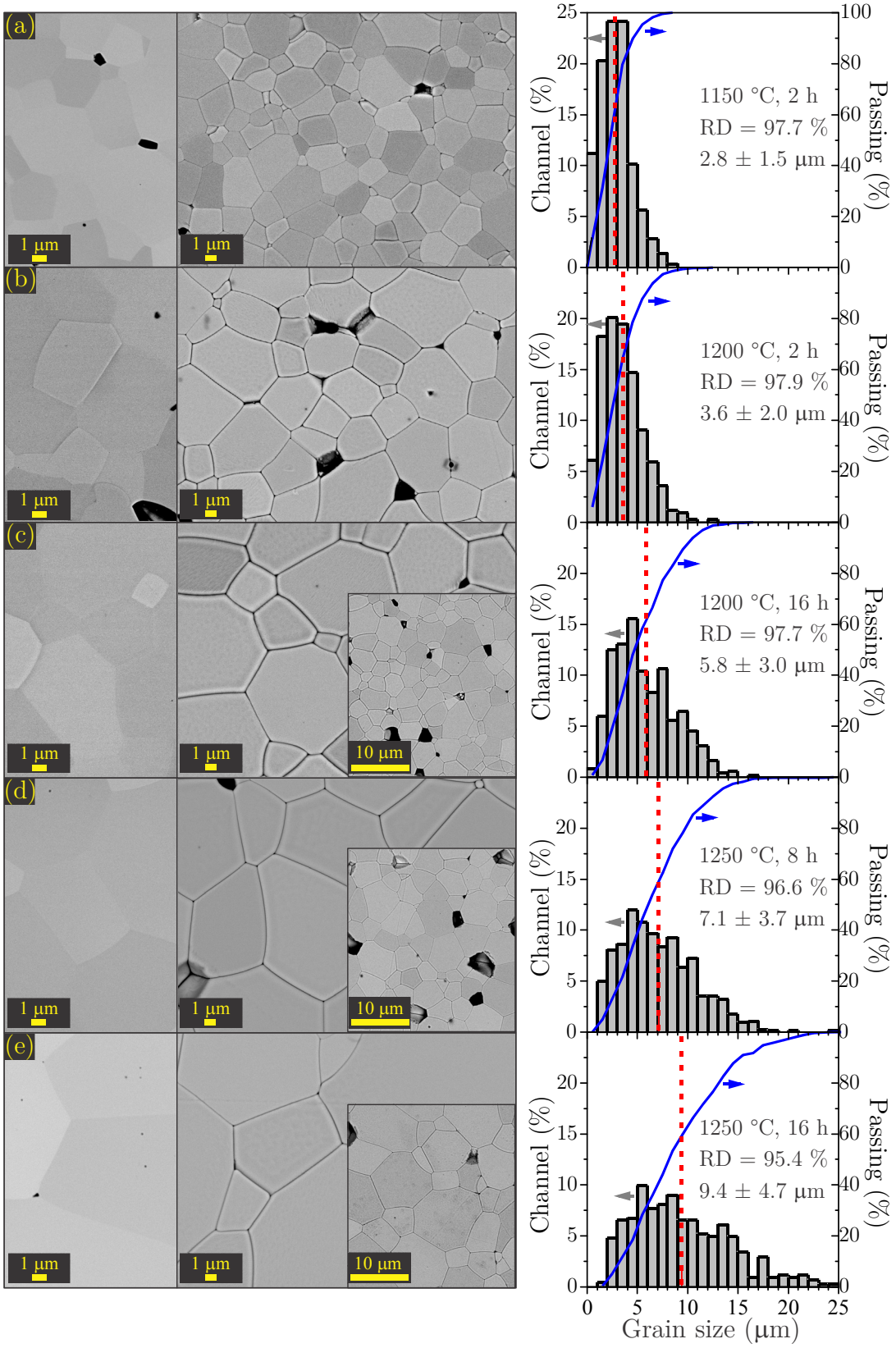


Figure 4.5: FE-SEM micrographs of the polished (left) and thermally etched (middle) surfaces together with the grain-size distributions and cumulative curves (right) of the PMN-10PT ceramics sintered at selected temperatures and times. Sintering conditions, RD and average grain sizes (denoted with a vertical dashed line) are added.

The densities of the PMN-10PT ceramic samples are shown in Figure 4.4 (b). The samples sintered at 1150 °C for 2 h and at 1200 °C for 2 h and 16 h have a high RD of ~98 %, while the samples sintered at 1250 °C for 8 h and 16 h have a slightly lower RD of 96.6 % and 95.4 %, respectively. A similar decrease in the density with increasing sintering temperature was also previously observed for PMN by Swartz et al. [78]. Namely, the PMN samples sintered at 1200 °C and 1270 °C for 1 h in the packing powder had RDs of 95.7 % and 93.3 %, respectively. Based on the weight losses, the authors connected the lower densities with a higher level of sublimation of the lead-oxide during the sintering process.

The FE-SEM images of the polished and thermally etched surfaces (Figure 4.5) reveal dense and homogeneous microstructures. Furthermore, no secondary phases were detected, in agreement with the XRD analysis. The stereological analysis revealed that the average grain size increased with the increasing thermal budget. Namely, by changing the sintering temperature and time the average grain sizes of the samples ranged from 2.8 ± 1.5 µm to 9.4 ± 4.7 µm. All the samples exhibited unimodal grain-size distributions, see Figure 4.5.

As mentioned in the Introduction (Section 1.3.2), Papet et al. [70] prepared PMN ceramics with grain sizes from 0.3 µm to 6.2 µm by hot pressing and conventional sintering, while Randall et al. [71] prepared the PMN-7PT ceramics with grain sizes from 1.5 µm to 9.0 µm by conventional sintering. In these studies the authors detected a Pb-rich amorphous phase, located at the grain boundaries in all the samples by TEM, regardless of the sintering conditions. The thickness of this intergranular phase was ~2 nm.

We additionally investigated the 3.6-µm- and 9.4-µm-grained samples using HR-TEM. The selected samples were exposed to considerably different thermal budgets, i.e., 1200 °C for 2 h as opposed to 1250 °C for 16 h. The analysis confirmed clean grain boundaries in both samples as is evident from Figure 4.6. No segregation of the secondary phases at the nanometer level could be detected.

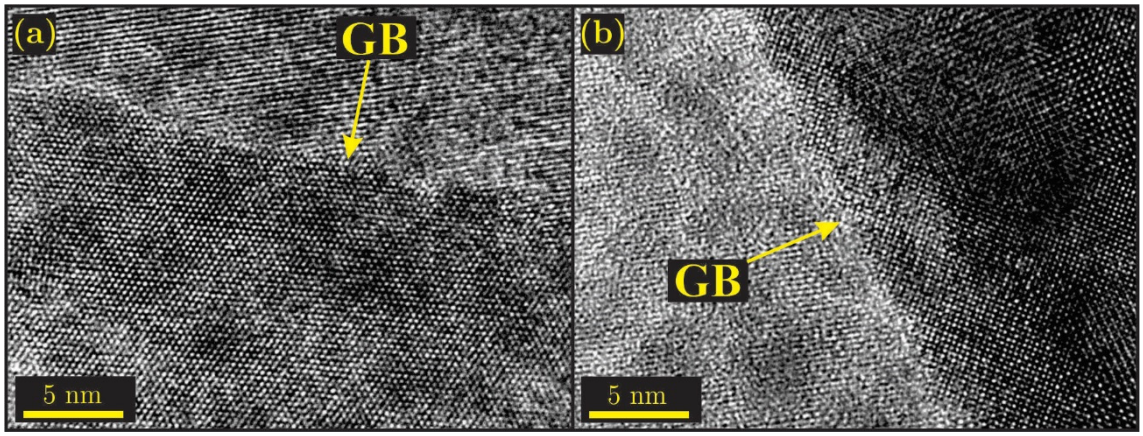


Figure 4.6: HR-TEM images of a grain boundary (GB) for the ceramics with an average grain size of (a) 3.6 µm and (b) 9.4 µm.

As mentioned above, the 9.4-µm-grained sample, i.e., the sample with the largest thermal budget had an RD of 95.4 %, which is noticeably lower than the RD of the sample with a finer microstructure (97.7 %). According to [78], a lower density could be a consequence of lead-oxide losses. Hence, the chemical compositions of the respective samples were additionally probed by WDXS analysis.

The results of the analysis are collected in Table 4.2. The analysis confirmed a low standard deviation in both samples, indicating the high chemical homogeneity. The Pb-contents are 20.31 at% ± 0.19 at% and 20.05 at% ± 0.43 at%, for the 3.6-µm- and 9.4-µm-grained samples, respectively. Furthermore, the calculated A:B ion ratio is lower in the

coarse-grained sample than in the fine-grained sample, 1.007 ± 0.016 as opposed to 0.994 ± 0.032. The latter confirms a slight lead deficiency in the sample with the largest grains, in agreement with its lower RD, see Figure 4.4 (b).

Table 4.2: Chemical composition with the standard deviation (STDEV) of the PMN-10PT ceramics with the average grain sizes of 3.6 µm and 9.4 µm obtained by WDXS.

	Nominal Composition	GS = 3.6 µm (1200 °C, 2 h)		GS = 9.4 µm (1250 °C, 16 h)	
Element	at%	at%	STDEV	at%	STDEV
Pb	20	20.31	0.19	20.05	0.43
Mg	6	6.78	0.20	6.45	0.14
Nb	12	11.34	0.16	11.73	0.28
Ti	2	2.05	0.03	1.99	0.03
O§	60	59.53	0.11	59.79	0.22

§ – calculated from the stoichiometry.

4.1.2 Dielectric Properties

The temperature dependences of the dielectric permittivity ε' of the PMN-10PT ceramics with grain sizes from 2.8 µm to 9.4 µm, measured at 1 kHz, are collected in Figure 4.7. The maximum value of ε' is approximately 30,000 for all the samples, regardless of the grain size. Note that the measured values are, by a few thousands, higher than the previously reported data [78], [81], [108], which could be related to the high level of chemical homogeneity obtained in our case by the mechanochemical synthesis of the powder [109]. The peak-permittivity temperature T_m is at ~47 °C for all samples, with the exception of the sample with the largest grains, which displays T_m at 42 °C.

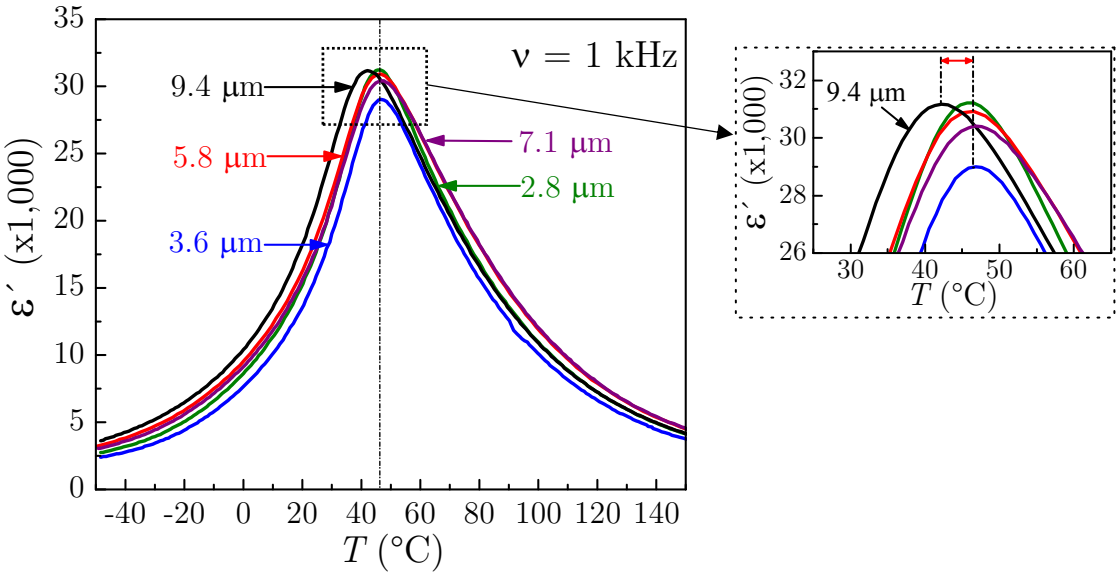


Figure 4.7: Dielectric permittivity ε' at 1 kHz as a function of temperature for the PMN-10PT ceramics with different grain sizes. Note the downward shift of the T_m of the 9.4-µm-grain sized sample in comparison to the other samples.

Swartz et al. [78] observed that the PbO-deficient PMN material experienced a downward shift of T_m, while the PMN with an excess of PbO experienced an upward shift of T_m with respect to the stoichiometric material.[14] This is in agreement with our results for the sample with 9.4-µm grains.

In PMN-10PT ceramics the relaxor-to-ferroelectric phase-transition temperature is electric-field dependent. Therefore, the ΔT_{EC} at a selected temperature depends on the amplitude of the electric field due to both the field-induced entropy change, and the shift of the phase-transition temperature at which the EC exhibits the maximum value. Rožič et al. [88] showed for the PMN-30PT ceramics that the ΔT_{EC} exhibits a maximum value at the relaxor-to-ferroelectric phase-transition temperature, which typically takes place in the middle of the low-temperature slope of the dispersive dielectric permittivity peak. For this reason, before introducing the results of the ΔT_{EC} as a function of temperature and electric field for PMN-10PT ceramics, we will verify the field-induced phase-transition temperature shift.

In Figure 4.8 the dielectric permittivity ε' and dielectric losses $tan\delta$ as a function of temperature at different dc electric field amplitudes for the 3.6-µm-grain sized sample are shown. At $E = 0$, the material exhibits a typical relaxor behavior, in agreement with earlier studies [78], [82]. When the dc electric field is applied, the frequency dispersion is strongly suppressed due to the induced ferroelectric phase [110], and the maximum dielectric permittivity is decreased. The ε'_{max} decreases from ~30,000 to ~3,100 at a dc field of 25 kV/cm. Furthermore, the peak temperature T_m experiences a significant upward shift when increasing the dc electric field amplitude, i.e., from 47 °C at 0 kV/cm to 115 °C at 25 kV/cm, as is evident from the inset of Figure 4.8.

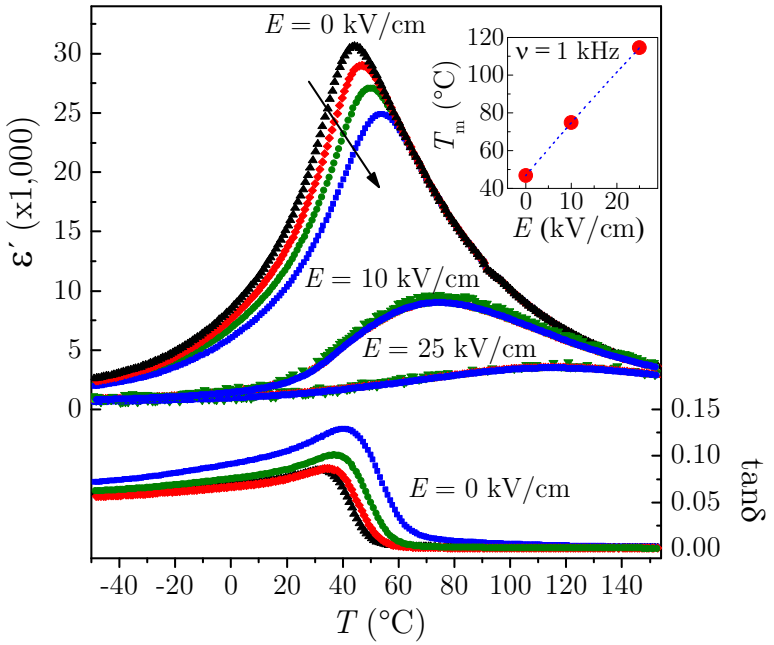


Figure 4.8: Temperature dependence of ε' and $tan\delta$ for PMN-10PT ceramics with an average grain size of 3.6 µm at 0.1, 1, 10 and 100 kHz for different applied dc electric fields. The arrow indicates the increase of frequency. Inset: T_m as a function of the applied dc field at 1 kHz.

[14] PMN with 2 mol% of PbO-deficiency had for 2 °C lower T_m and the PMN with 2 mol% of PbO-excess had for 3 °C higher T_m than the stoichiometric PMN.

4.1.3 Electrocaloric Properties

The EC effect as a function of temperature and electric field was investigated by the indirect and direct methods, as described in Section 3.2.11. In order to evaluate the EC effect by the indirect method, the $P-E$ hysteresis loops at 1 Hz were measured with a temperature step of 5 °C. The indirect EC measurements are shown for the PMN-10PT ceramics with the 5.8-µm-large grains only (Figure 4.9), while the EC results for the other samples are discussed later in this section.

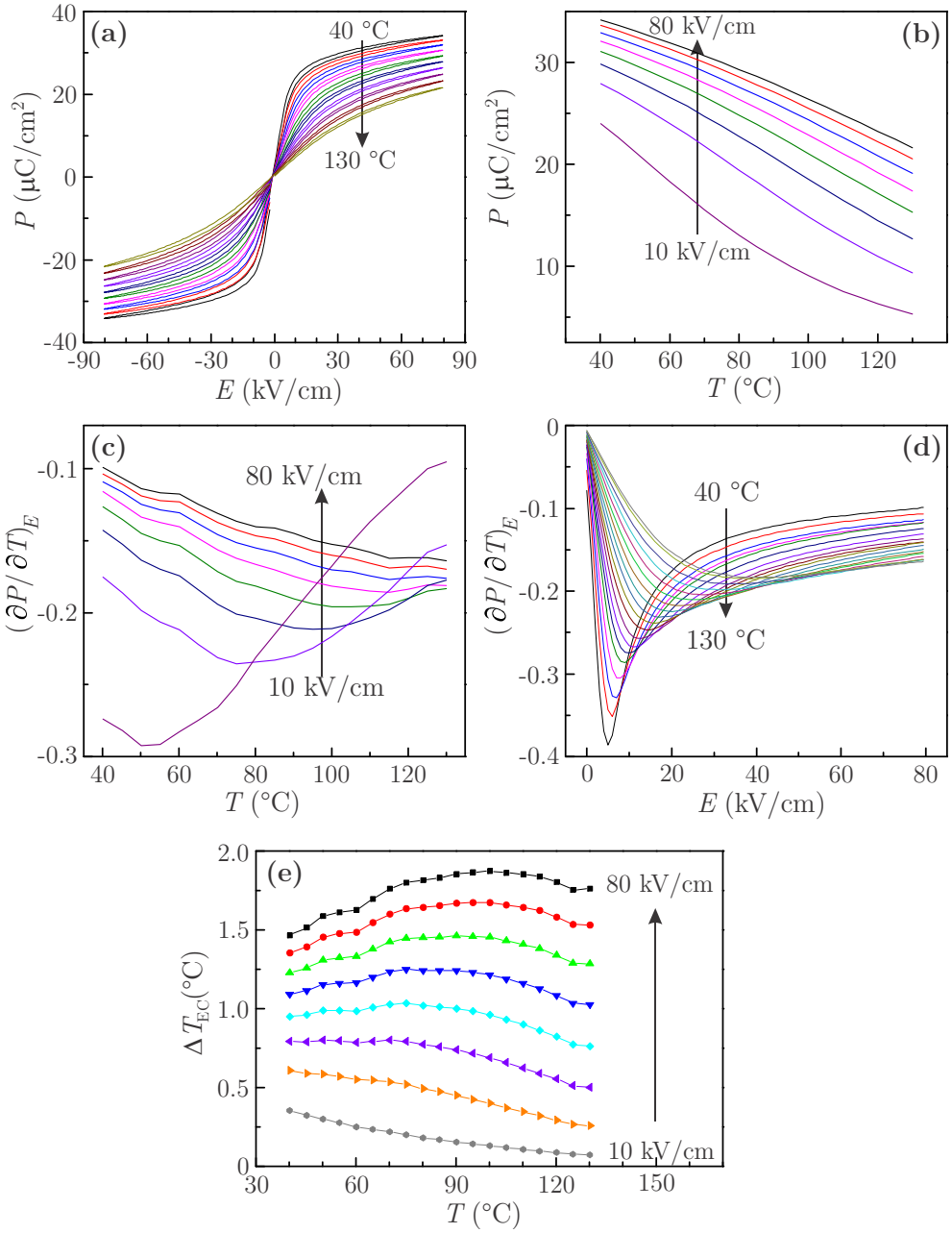


Figure 4.9: (a) The $P-E$ hysteresis loops of the PMN-10PT ceramics with average grain size of 5.8 µm, measured at 1 Hz within the temperature interval from 40 °C to 130 °C with a step of 5 °C. (b-e) Intermediate results of the indirect EC evaluation, extracted from the $P-E$ hysteresis loops, from which the final (e) ΔT_{EC} as a function of temperature at selected electric field amplitudes is calculated.

Figure 4.9 (a) reveals that the 5.8-µm-grain-sized sample displays relaxor-like slim $P-E$ hysteresis loops in the measured temperature range (40–140 °C). The saturation polarization value P_s is 33 µC/cm^2 and 19 µC/cm^2 at 40 °C and 130 °C, respectively.

The polarization values as a function of temperature and electric field $P(T,E)$, extracted from the $P-E$ hysteresis loops are shown in Figure 4.9 (b). It is evident that the polarization continuously decreases across the whole measurement range, implying that the sign of $(\partial P/\partial T)_E$ is negative (see Figure 4.9 c). Since the PMN-10PT composition is in the ergodic state in the studied temperature interval and no first-order phase transition is expected, the continuous decrease of polarization is in good agreement with the phase diagram [68], [69], [111].

The data for $(\partial P/\partial E)_T$ vs. E from which the ΔT_{EC} was subsequently extracted are shown in Figure 4.9 (d). The ΔT_{EC} was calculated by using the experimental data of the sample density, and specific heat capacity c_E. The latter was determined by DSC and the results are collected in Appendix B. For the calculation of the ΔT_{EC} the temperature dependence of the heat capacity was taken into account, while its field dependence was neglected. This is a good approximation since no transitions accompanied with high entropy changes are expected when applying high electric fields in the studied temperature range for the PMN-10PT.

The ΔT_{EC} as a function of temperature at selected electric field amplitudes is shown in Figure 4.9 (e). In agreement with Eq. (1.13), the ΔT_{EC} increases with the electric field. At the electric field of 10 kV/cm the peak ΔT_{EC} cannot be observed, because it is most probably below the temperature range of the measurements [89]. Therefore, the highest measured ΔT_{EC} at 10 kV/cm is 0.35 °C at the lowest temperature of 40 °C. At electric field amplitudes higher than 40 kV/cm, the peak maximum can be observed and it experiences an upward shift with an increasing electric field. Namely, the peak, determined by the point of maximum ΔT_{EC}, appears at 75 °C (ΔT_{EC} = 1.03 °C) and 100°C (ΔT_{EC} = 1.87) at the electric field of 40 kV/cm and 80 kV/cm, respectively.

The results of the direct and indirect EC measurements of the PMN-10PT ceramics with 2.8–9.4-µm-sized grains are collected in Figure 4.10 (a-e). The indirect EC measurements were performed as descried above.

According to the direct EC measurements all the samples withstood electric fields of 115 kV/cm, and the fine-grained PMN-10PT materials, i.e., with 2.8-µm and 3.6-µm grains, could be loaded with electric fields as high as 160 kV/cm without experiencing the dielectric breakdown. These electric fields are more than three times higher than the fields used in previous EC studies of PMN-10PT, see Table 1.2. For example, Zhang et al. [112], Shebanovs et al. [86] and Peräntie et al. [89] performed the EC measurements of PMN-10PT ceramics up to 15 kV/cm, 29.1 kV/cm and 50 kV/cm. However, it is not clear whether the authors of these studies performed the EC measurement at higher electric fields. On the other hand, Hagberg et al. [94] reported that the direct EC measurements of PMN-13PT at electric fields higher than 24 kV/cm were not possible due to the occurrence of a dielectric breakdown.

During the direct EC measurements no Joule heating was observed. For example, see Figure 4.10 (f), where 160 kV/cm was applied during an EC measurement. Note that the indirectly measured ΔT_{EC}, obtained from the polarization-electric field ($P-E$) hysteresis loops at different temperatures (see Figure 4.9), are in a good agreement with the direct measurements.

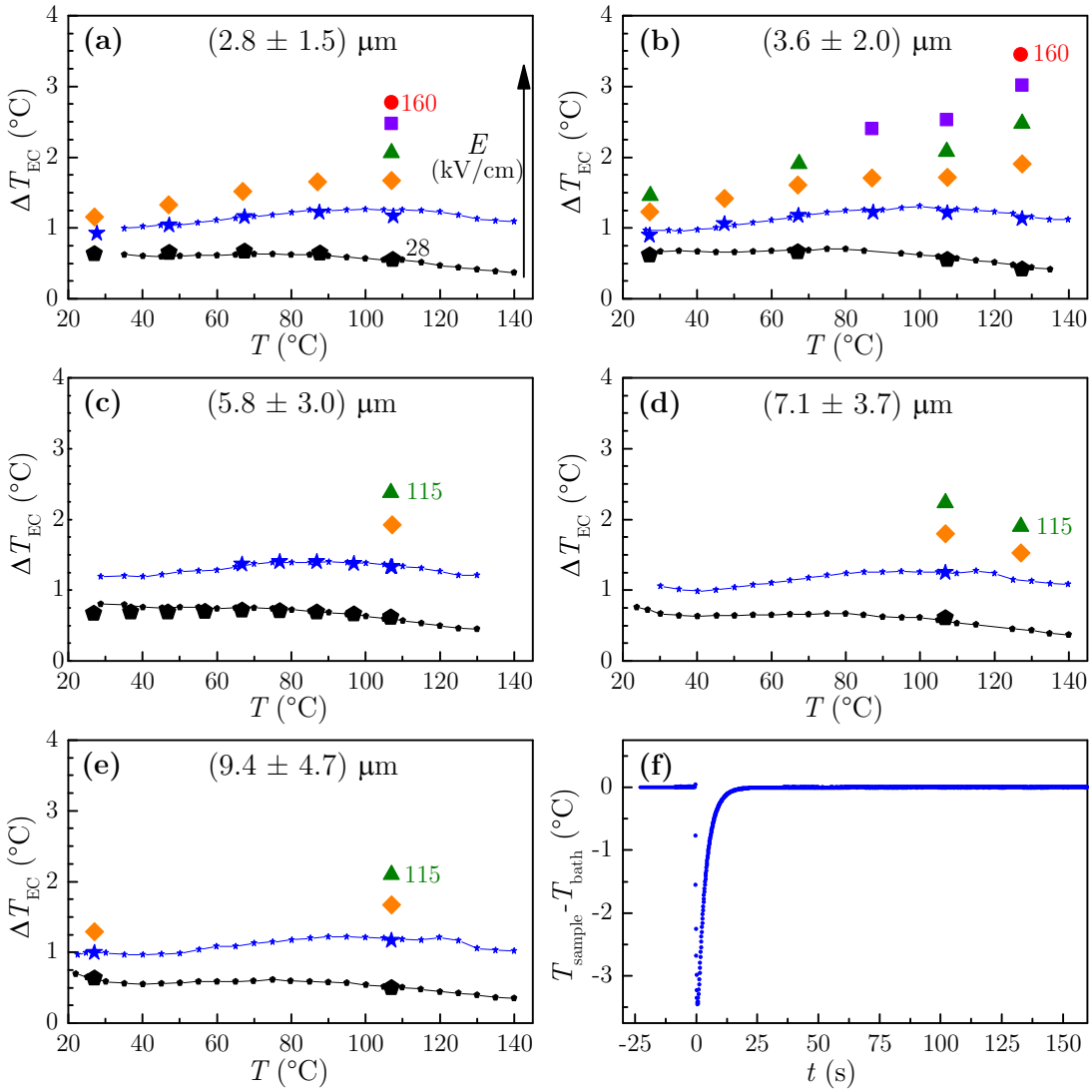


Figure 4.10: (a-e) The ΔT_{EC} of the PMN-10PT ceramics sintered at (a) 1150 °C for 2 h, (b) 1200 °C for 2 h, (c) 1200 °C for 16 h, (d) 1250 °C for 8 h and (e) 1250 °C for 16 h. The average grain sizes of the respective samples are included in the graphs. The larger and smaller symbols represent the results of the direct and indirect EC measurements, respectively. Lines are a guide for the eye. The arrow indicates the increase of the electric field amplitude from 28, 57, 87, 115, 140 to 160 kV/cm. (f) The directly measured EC response of a sample with the average grain size of 3.6 μm, obtained during the field removal (160 kV/cm).

A comparison of ΔT_{EC} and ε' as a function of temperature at similar electric field amplitudes is shown in Figure 4.11. It is clear that the maximum EC response coincides with the middle of the low-temperature slope of the dielectric permittivity peak at similar electric field amplitudes. The upward shift of the dielectric permittivity and ΔT_{EC} peaks with the increasing dc electric field (see Figure 4.8) corresponds with the upward shift of the phase-transition temperature under the increasing dc electric field [110].

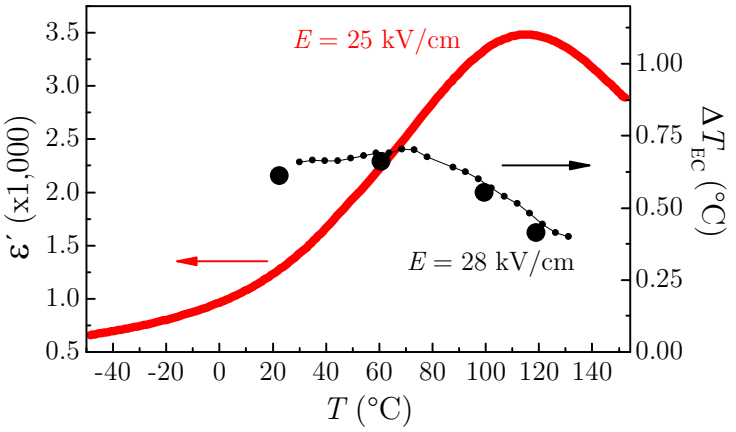


Figure 4.11: The ε' at the applied dc electric field of 25 kV/cm and at 1 kHz and ΔT_{EC} at 28 kV/cm as a function of temperature for the 3.6-µm-grain-sized sample. Data from Figure 4.8 and Figure 4.10 (b). The larger and smaller circles represent the direct and indirect EC measurements, respectively. Lines are a guide for the eye.

In Figure 4.12 (a) the ΔT_{EC} values of the ceramics with grain sizes from 2.8 µm to 9.4 µm at electric field amplitudes of up to 140 kV/cm and at 107 °C are collected. At the lowest electric field of 28 kV/cm the sample with the grain size of 5.8 µm exhibits a higher value than the other samples, i.e., 0.61 °C as compared to 0.55 °C. Such a trend persists and becomes even more pronounced with the increasing electric field amplitude. The EC coefficient, i.e., $\Delta T_{EC}/E$, at the electric field of 57 kV/cm is represented as a function of grain size in Figure 4.12 (a). Evidently, the ceramic with the grain size of 5.8 µm possesses the highest $\Delta T_{EC}/E$ of 2.3×10^{-7} °Cm/V, which is more than 10 % higher than the values obtained for the samples with finer or coarser grains.

It is well known that the EC effect is correlated with the material's dielectric properties, namely the ΔT_{EC} increases with increasing polarization, see Section 1.2.1 and [29], [30], [32]. Hence, the $P-E$ hysteresis loops of the ceramics with different grain sizes were measured at the same electric field amplitude of 57 kV/cm and at 107 °C. In Figure 4.12 (b) the values of the saturated polarization (P_s) vs. grain size are collected. The data reveal that the peak P_s value of 23.5 µC/cm^2 was obtained for the sample with the grain size of 5.8 µm, in agreement with the $\Delta T_{EC}/E$ dependence from Figure 4.12 (b). The maximum EC response of the ceramic with 5.8-µm grains at moderate electric field amplitudes in comparison with the materials having finer or coarser grains, is presumably related to its optimum microstructure in terms of grain size, chemical homogeneity and a high relative density. Nevertheless, the fine-grained samples exhibit the largest ΔT_{EC}, i.e., ~2.5 °C at ≥ 140 kV/cm and 107 °C, due to the higher breakdown strength than the coarser-grained ceramics, cf. Figure 4.12. As a consequence of an interplay between the increasing breakdown strength and the decreasing polarization, the largest ΔT_{EC} at the electric field amplitude of 160 kV/cm was obtained for the PMN-10PT with 3.6-µm-sized grains, i.e., 3.45 °C at 127 °C. Such a high value is obtained far away from any multi-critical point of the material [110], and it is attributed to the excellent chemical homogeneity of the mechanochemically derived material, evidenced by the WDXS analysis (see Table 4.2) and the absence of any grain-boundary layers or secondary phases (cf. Figure 4.5 and Figure 4.6), which have been reported to reduce the dielectric properties of PMN-PT [70]–[72].

The obtained ΔT_{EC} exceeds all the previously reported values for PMN-PT ceramics, see Table 1.2, and even for all Pb-based ceramics [32], [33]. Up until now, the highest

measured ΔT_{EC} of 2.7 °C in Pb-based ceramics was obtained in PMN-30PT at ~160 °C and 90 kV/cm [88].

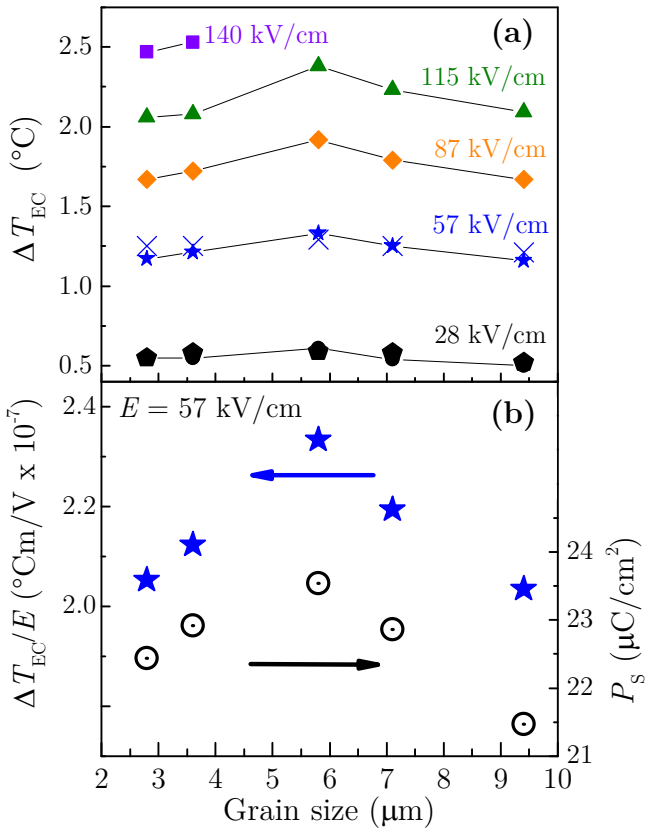


Figure 4.12: (a) The ΔT_{EC} and (b) $\Delta T_{EC}/E$ (solid stars) and P_s (open circles) vs. the average grain size of the PMN-10PT ceramics at 107 °C. (a) The solid symbols and crosses represent the data obtained by the indirect and direct measurements, respectively, extracted from Figure 4.10. Lines are a guide for the eye.

4.1.4 Summary

The main findings of this section are collected in Table 4.3.

Table 4.3: Summary of the relevant findings presented in the current section

PMN-10PT powder	• Perovskite phase coexisting with amorphous phase. • Narrow particle size distribution (d_{50}=0.31 µm). • Traces of W (236 mg/kg) and Zr (52 mg/kg) due to the wear of the milling media.
PMN-10PT ceramics	• Sintering at 1150–1250 °C for times from 2 h to 16 h. • Perovskite phase. • RD~98 % (sintering at 1150 °C, 1200 °C) and RD~96 % (sintering at 1250 °C). • Homogeneous microstructure with grains from 2.8 µm to 9.4 µm, no secondary phases. • HR-TEM: clean grain boundaries. • WDXS: a slight PbO-deficiency in the 9.4-µm-grain-sized sample.
Dielectric properties	• Typical relaxor $\varepsilon'(T, \nu)$ dependence. • ε'_{max}(1 kHz) of ~30,000, i.e., for a few thousands higher than in previous studies [78], [81], [108]. • A dc electric field induces a ferroelectric phase, observed as a suppressed frequency dispersion of $\varepsilon'(T)$, decrease of ε'_{max} and upward shift of T_m.
Dielectric breakdown strength	• All samples withstand 115 kV/cm. • E_b of the fine-grained samples ($\leq$3.6 µm) higher than 160 kV/cm.
Electrocaloric properties	• No Joule heating during the direct EC measurements. • 5.8-µm-grain-sized: the largest EC coefficient (2.3×10^{-7} °Cm/V) due to the largest P_s and attributed to the optimum microstructure. • ~10 % lower EC coefficients in the samples with finer and coarser grains. • ΔT_{EC} of ~3.5 °C in the 3.6-µm-grain-sized sample at 160 kV/cm exceeds all the previously reported values for Pb-based ceramics [32], [33].

4.2 Electrocaloric Properties of $0.9Pb(Mg_{1/3}Nb_{2/3})O_3$-$0.1PbTiO_3$ Ceramics Prepared by Columbite Synthesis

The main goal of this section is to study the EC properties of PMN-10PT ceramics that were prepared by the columbite synthesis. We discuss the synthesized powder and ceramics in terms of phase composition and microstructure, and the dielectric and EC properties of the prepared ceramics as functions of electric field and temperature.

4.2.1 Phase Composition and Microstructure

The PMN-10PT ceramic powder was prepared using the two-step columbite synthesis as described in Section 3.1.1.2. According to the XRD analysis of the calcined MgO–Nb_2O_5 powder mixture all the peaks could be described with the crystallographic card of the orthorhombic $MgNb_2O_6$ (JCPDS 88-0708). This indicates that the reaction between MgO and Nb_2O_5 after a 4-h-long calcination at 1150 °C was completed.

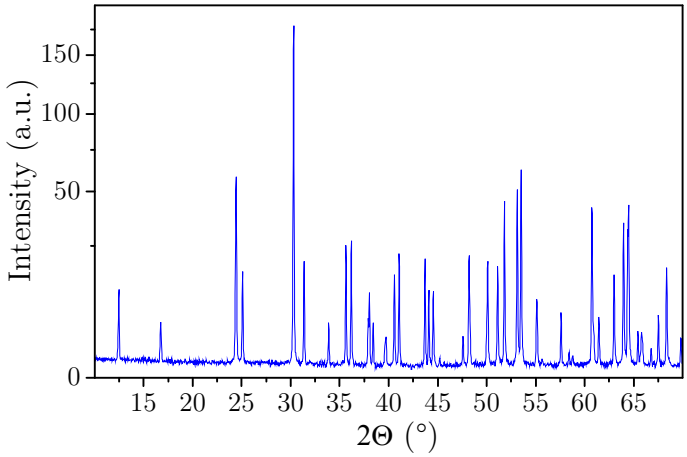


Figure 4.13: The XRD pattern of the columbite precursor after calcination at 1150 °C for 4 h. All the peaks correspond to the orthorhombic $MgNb_2O_6$ (JCPDS 88-0708). Note the square-root scale of the y-axis.

In the second step the PbO and TiO_2 were added to the $MgNb_2O_6$ in the molar ratio corresponding to the PMN-10PT stoichiometry. The XRD analysis reveals that the powder after calcination consists of multiple phases (Figure 4.14). Namely, the high-intensity peaks correspond to the perovskite PMN phase (JCPDS 81-0861), while the low-intensity peaks correspond to the cubic pyrochlore $Pb_{1.86}Mg_{0.24}Nb_{1.76}O_{6.5}$ (JCPDS 82-0338) and the tetragonal $PbTiO_3$ (PT, JCPDS 078-0299), see the inset of Figure 4.14. The formation of a small amount (<2 %) of the pyrochlore phase during the columbite synthesis of the PMN was also previously reported by Swartz et al. [77]. Furthermore, the presence of the PT phase indicates the chemical heterogeneity of the PMN-10PT powder, in agreement with an earlier study [72].

The quantitative chemical analysis of the PMN-10PT powder revealed the presence of Zr in the concentration 1151 mg/kg (0.42 %[15]). The Zr impurity is a consequence of the wear of the milling balls during the attrition milling. A possible influence of the Zr impurity on the functional properties of PMN-10PT is discussed in Section 4.3.

[15] Mole of contaminant per mole of PMN-10PT in %.

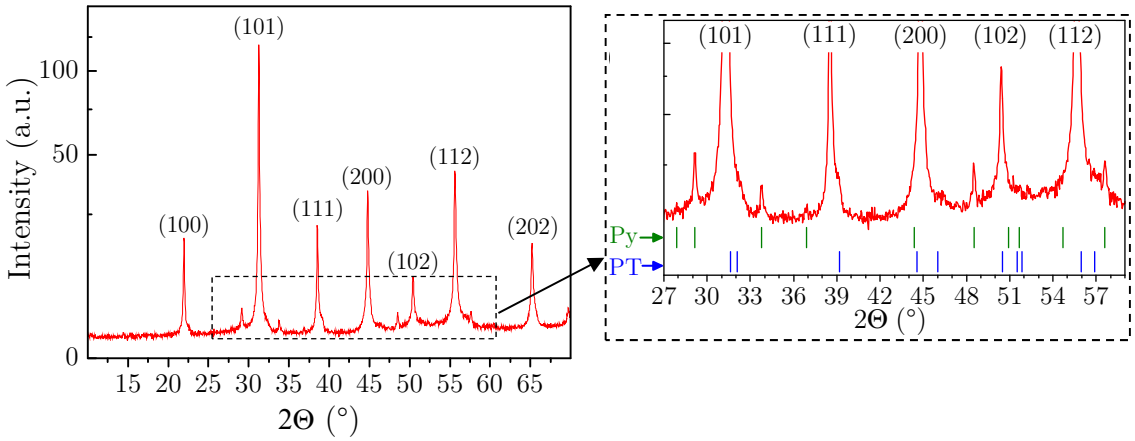


Figure 4.14: XRD pattern (red line) of the PMN-10PT powder after the second calcination step at 750 °C for 4 h. Inset: Smaller scale of the XRD pattern. All the high-intensity peaks correspond to the cubic PMN (JCPDS 81-0861)[16] and are denoted with the corresponding Miller indices. The green and blue tick marks correspond to the peak positions of the cubic pyrochlore $Pb_{1.86}Mg_{0.24}Nb_{1.76}O_{6.5}$ (Py; JCPDS 82-0338) and to the tetragonal $PbTiO_3$ (PT; JCPDS 078-0299), respectively. Note the square-root scale of the y-axis.

Figure 4.15 (a) shows the FE-SEM micrographs of the PMN-10PT powder after the final attritor milling. The powder consists of individual particles ranging from about 50 nm to about 500 nm. A lower-magnification image reveals that the particles form loose agglomerates with sizes up to a few microns. The particle size distribution (Figure 4.15 b) is very narrow and the median particle size d_{50} is equal to 0.25 µm. A total of 90 % of the particles are smaller than 0.56 µm, in agreement with the FE-SEM investigations.

A dynamic sintering curve of the PMN-10PT powder compact is shown in Figure 4.16 (a). From the start of the recording at 200 °C up to ~800 °C almost no changes in the dimensions of the powder compact are observed. The sample starts to shrink above this temperature and a steep slope in the shrinkage curve indicates a rapid densification between ~900 °C and ~1050 °C. Above ~1050 °C the sample only shrinks slightly until the final temperature of 1300 °C.

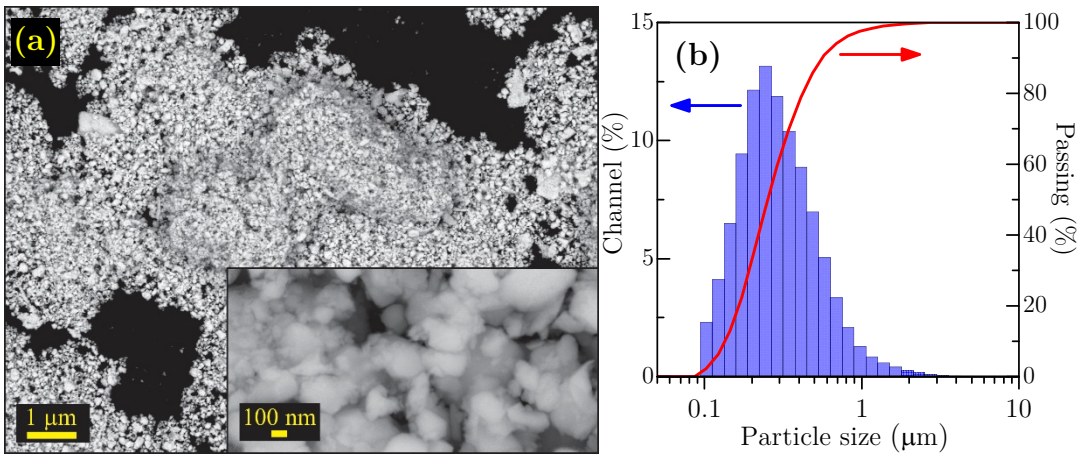


Figure 4.15: (a) FE-SEM micrographs and (b) particle size distribution of the PMN-10PT powder, prepared by the columbite synthesis and subsequent attrition milling.

[16] The crystallographic data for PMN-10PT do not exist in the JCPDS database so the best match could be obtained with the JCPDS 81-0861 card for cubic PMN phase.

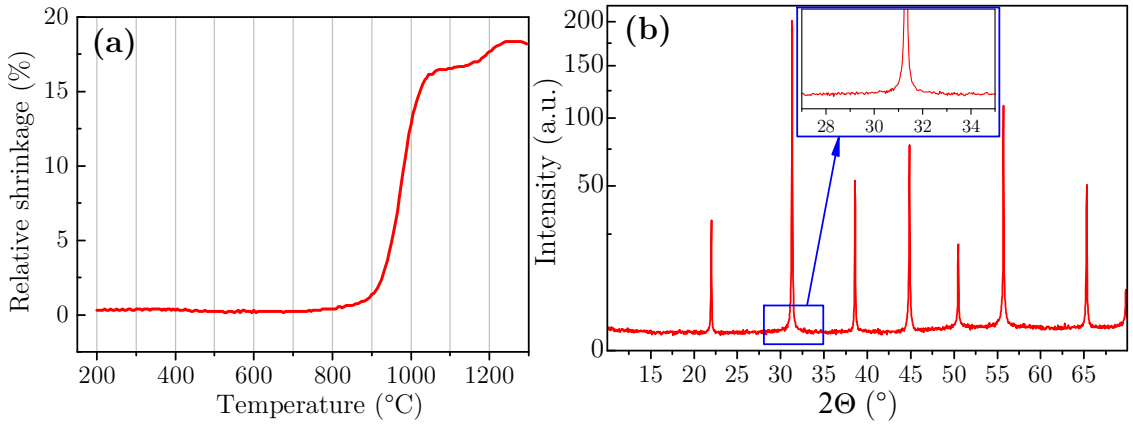


Figure 4.16: (a) Dynamic sintering curve of the PMN-10PT powder compact. The heating rate was 5 C/min. (b) The XRD pattern of the sintered PMN-10PT ceramics. All the peaks correspond to the perovskite phase (JCPDS 81-0861). Note the square-root scale of the y-axis.

The PMN-10PT powder compacts were sintered at 1200 °C for 2 h. The columbite-derived sample had a RD of 96.3 %. According to the XRD analysis the sample consisted only of the perovskite phase (JCPDS 81-0861), see Figure 4.16 (b). Note that the columbite-derived PMN-10PT powder consisted of multiple phases – a perovskite phase as the predominant phase and pyrochlore and PT phases in trace amounts, see Figure 4.14. This indicates that both the transformation of pyrochlore-to-perovskite and the chemical homogenization process took place during the sintering.

Leite et al. [72] reported that a columbite-derived PMN-35PT powder was chemically heterogeneous, as in our case. Furthermore, they prepared ceramic samples by hot-pressing at 950 °C for 0.5 h, which were chemically heterogeneous as well. Additional heat treatments of the latter samples at 1150 °C for 5 h or 10 h resulted in ceramic samples with a high level of chemical homogeneity, as confirmed by the TEM. The chemical homogenization process may also explain the suppressed densification process, observed in the dynamic sintering curve at about 1150 °C, see Figure 4.16 (a).

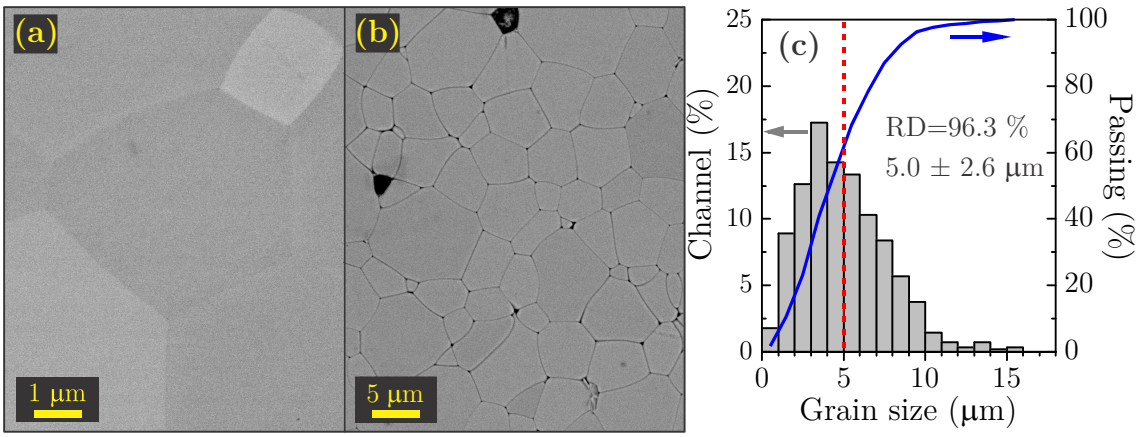


Figure 4.17: FE-SEM micrographs of the (a) polished and (b) thermally etched surfaces. (c) The grain size distribution and cumulative curve of the PMN-10PT ceramics, prepared by the columbite synthesis and sintering at 1200 °C for 2 h. The RD and the average grain size (denoted with a vertical dashed line) are added.

The FE-SEM analysis of the polished surface (Figure 4.17 a) confirmed the absence of the secondary phases, in agreement with the XRD analysis. The thermally etched surface (Figure 4.17 b) reveals a dense and homogeneous microstructure with an average grain size of 5.0 ± 2.6 µm. The grain size distribution is narrow, see Figure 4.17 (c).

Note that we could not investigate the ceramic samples prepared by the columbite method using TEM. Despite several attempts to prepare the specimens they broke during dimpling and Ar-milling before the appropriate thickness could be reached. For this reason, the presence of a lead-oxide rich intergranular phase, detected by TEM in an earlier study of the columbite-derived PMN-7PT ceramics [71] cannot be excluded.

The chemical composition of the samples with an average grain size of 5.0 µm ± 2.6 µm was additionally probed using WDXS analyses (Table 4.4). The analyzed lead content is 20.31 at% ± 0.33 at%, which is close to the nominal composition. Similarly, the determined contents of the other elements were in a good agreement with the nominal values. A low level of compositional deviation confirmed the high uniformity of the investigated sample. The calculated A:B ion ratio is 1.006 ± 0.029, confirming that the perovskite stoichiometry was preserved.

Table 4.4: Chemical composition with the standard deviation (STDEV) of the PMN-10PT ceramics with average grain sizes of 5.0 µm ± 2.6 µm obtained by WDXS.

	Nominal Composition	1200 °C, 2 h (GS = 5.0 µm)	
Element	at%	at%	STDEV
Pb	20	20.31	0.33
Mg	6	6.08	0.15
Nb	12	12.2	0.12
Ti	2	1.89	0.03
O§	60	60.11	0.09

§ – calculated from the stoichiometry.

As mentioned above, the ICP analysis revealed 1151 mg/kg of zirconium in the PMN-10PT powder. Therefore, the polished surface of the sintered sample was additionally probed by the standardless WDXS analysis[17] in order to detect the zirconium spectral lines. The analysis was performed on six different spots within the grains and seven different spots on the grain boundaries. Note that zirconium was not detected in any of the analyzed spots, indicating that it is not segregating and is homogeneously distributed in the ceramic material.

4.2.2 Dielectric Properties

The temperature and frequency dependence of the ε' and $tan\delta$ for increasing dc electric field amplitudes of the PMN-10PT ceramics are shown in Figure 4.18. At zero-electric field the material displays a characteristic frequency dispersion and the ε'_{max} reaches 28,000 at 47 °C and 1 kHz, in good agreement with the previous studies of PMN-10PT [78], [81], [108]. In the vicinity of the T_m and 1 kHz the $tan\delta$ approaches 8 %.

The application of a dc electric field induces the ferroelectric phase [110], which is observed as a strong suppression of the frequency dispersion, a decrease of the ε' in the whole temperature range and an upward shift of T_m. For example, at 1 kHz the ε'_{max} progressively decreases from ~28,000 at 0 kV/cm to 3,800 at 25 kV/cm. In addition, the

[17] The standardless WDXS analysis could provide only qualitative information about the investigated element.

T_m experiences an upward shift from 47 °C at 0 kV/cm to 116 °C at 25 kV/cm. The latter is additionally shown in the inset of Figure 4.18.

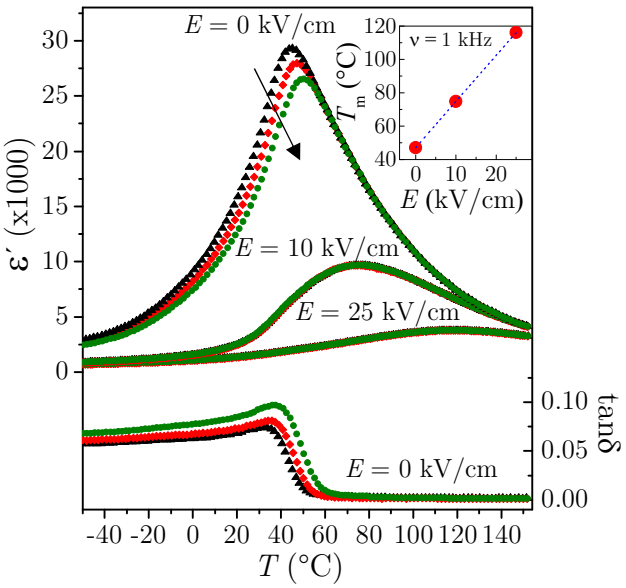


Figure 4.18: Temperature dependence of the ε' and $tan\delta$ at 0.1, 1, and 10 kHz for different applied dc electric fields of the columbite-derived PMN-10PT ceramics. The arrow indicates the increase of frequency. Inset: T_m as a function of the applied dc field at 1 kHz.

4.2.3 Electrocaloric Properties

The indirect EC measurements of the PMN-10PT ceramics were performed as described in Section 4.1.3 and are collected in Figure 4.19. The polarization values continuously decrease with the temperature, e.g., the P_s is 31.3 µC/cm^2 and 17.6 µC/cm^2 at 40 °C and 140 °C, respectively (Figure 4.19 a). The ΔT_{EC} increases with the electric field, in agreement with Eq. (1.13), see Figure 4.19 (b). At an electric field of 10 kV/cm the peak ΔT_{EC} cannot be observed, most probably because it is below the temperature range of the measurements [89].

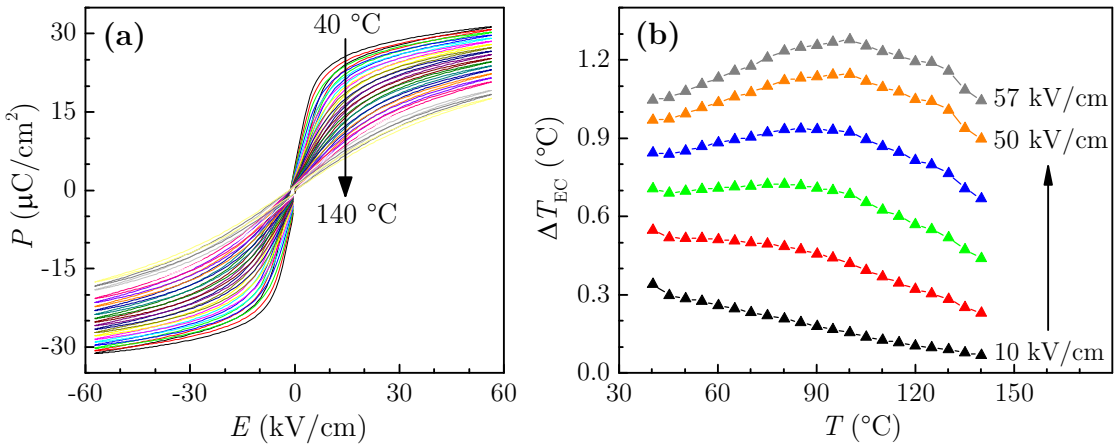


Figure 4.19: (a) The $P-E$ hysteresis loops of the PMN-10PT ceramics, prepared by columbite synthesis, and with an average grain size of 5.0 µm. The measurements were performed at 1 Hz within the temperature interval from 40 °C to 140 °C with a step of 5 °C. (b) The indirectly calculated ΔT_{EC} as a function of temperature shown at a few selected electric fields. The results are extracted from the data collected in (a).

Therefore, the highest measured ΔT_{EC} at 10 kV/cm is 0.34 °C at a temperature of 40 °C. At electric field amplitudes higher than 40 kV/cm, the peak ΔT_{EC} is evident and it experiences an upward shift with an increasing electric field. Namely, the peak appears at 85 °C (ΔT_{EC} = 0.93 °C) and 100°C (ΔT_{EC} = 1.30) at the electric fields of 40 kV/cm and 57 kV/cm, respectively. Note that the measurements at higher electric fields were not possible because the samples did not survive electric fields higher than ~60 kV/cm.

The results of the direct and indirect EC measurements at the same electric field amplitudes for the PMN-10PT ceramics are collected in Figure 4.20. No Joule heating was observed during the direct EC measurements. All the samples withstood electric fields of 57 kV/cm; however, at electric fields above ~60 kV/cm, the samples experienced a dielectric breakdown. Note a substantially lower dielectric breakdown strength in comparison with PMN-10PT ceramics, prepared by mechanochemical synthesis, regardless of the grain size (cf. Figure 4.10).

Nevertheless, the electric field amplitudes applied in the direct and indirect EC measurements are still considerably higher than the electric fields used in reported earlier EC studies, see Table 1.2. The EC measurements of the columbite-derived PMN-10PT in [86], [112] were carried out at electric field amplitudes lower than 30 kV/cm, and in [89] up to 50 kV/cm. The columbite-derived PMN-8PT [93] and PMN-13PT [94], prepared by reactive sintering, were loaded with electric field amplitudes of 20 kV/cm and 24 kV/cm, respectively. In [94] the authors reported that the EC measurements at fields higher than 24 kV/cm were not possible due to the occurrence of a dielectric breakdown.

The highest directly measured ΔT_{EC} of 1.39 °C was reached at 57 kV/cm and 97 °C. The EC coefficient at this temperature is therefore equal to 2.4×10^{-7} °Cm/V. The directly measured ΔT_{EC} values are in a good agreement with a recent study by Peräntie et al. [89], who measured a ΔT_{EC} of 1.19 °C at 50 kV/cm and 89 °C in the columbite-derived PMN-10PT ceramics.

Note that the ΔT_{EC} values obtained by the indirect method are slightly lower than those obtained by the direct measurements. This difference is even more pronounced at higher electric fields, for example, at 57 kV/cm and ~105 °C the directly and indirectly measured ΔT_{EC} are 1.38 °C and 1.28 °C, respectively. This discrepancy between the directly and indirectly obtained EC results is further discussed in the next main section of this chapter.

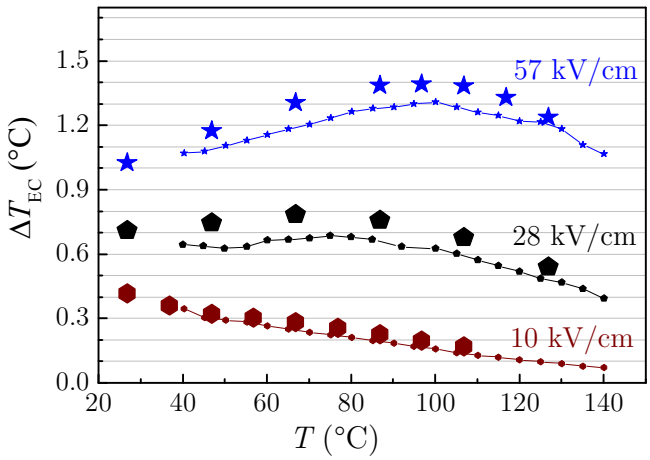


Figure 4.20: The ΔT_{EC} of the PMN-10PT ceramics (GS = 5.0 µm), prepared by the columbite synthesis and subsequent sintering at 1200 °C for 2 h. The larger and smaller symbols represent the results of the direct and indirect EC measurements, respectively. Lines are a guide for the eye.

4.2.4 Summary

The main findings of this section are collected in Table 4.5.

Table 4.5: Summary of the relevant findings presented in the current section.

PMN-10PT powder	• Perovskite with traces of PT and pyrochlore phase. • Narrow particle size distribution (d_{50}=0.25 µm). • Traces of Zr (1151 mg/kg) due to the wear of the milling media.
PMN-10PT ceramics	• Sintering at 1200 °C for 2 h. • Single-perovskite phase. • RD: 96.3 %. • Uniform microstructure with an average grain size of 5.0 µm. • WDXS: stoichiometric composition.
Dielectric properties	• Typical relaxor frequency dispersion of $\varepsilon'(T)$. • ε'_{max} = 28,000 at 1 kHz. • dc electric field induces a ferroelectric phase resulting in a suppressed frequency dispersion, decrease of ε'_{max} and upward shift of T_m.
Dielectric breakdown strength	• E_b~60 kV/cm.
Electrocaloric properties	• No Joule heating during the direct EC measurements. • The EC coefficient $\Delta T_{EC}/E$ of 2.4×10^{-7} °Cm/V. • The ΔT_{EC} of 1.39 °C, obtained at 57 kV/cm and 97 °C.

4.3 Comparison of $0.9Pb(Mg_{1/3}Nb_{2/3})O_3$-$0.1PbTiO_3$ Ceramics Prepared by Mechanochemical and Columbite Synthesis

The first part of the results addressed the EC properties of the mechanochemically synthesized PMN-10PT ceramics with different grain sizes, while in the second part we discussed the EC properties of the ceramics, prepared by the columbite method. In this section we compare and discuss the materials, dielectric and EC properties of the ceramics, prepared by different synthesis methods.

4.3.1 Powders and Ceramics

To maintain the clarity of the text in this section, the PMN-10PT samples, prepared by mechanochemical and columbite synthesis are denoted as the Mech and Col, respectively. We briefly compare the powders prepared by the two synthesis methods, for details please refer to Section 4.1 and 4.2.

The XRD patterns of the powders are collected in Figure 4.21. Although in both cases the perovskite PMN[16] is the major phase, the full width at half maximum of the Col peaks is lower, indicating a larger crystallite size. The Mech powder contains a large fraction of the amorphous phase, as discussed in Subsection 4.1.1, while traces of the $PbTiO_3$ (PT) and pyrochlore phases are present in the Col powder.

The particle size distributions of the two powders, shown in Figure 4.22 (a) are narrow. The d_{90} of the Mech and Col are 0.93 µm and 0.56 µm, respectively. The bimodal distribution of the Mech powder indicates the presence of agglomerates, as confirmed by the micrograph of the powder (Figure 4.2 a).

The dynamic sintering curves of both powder compacts reveal quite different shrinkage behaviors, see Figure 4.22 (b). Namely, the Col sample starts to shrink intensively at a lower temperature than the Mech, ~900 °C as opposed to ~950 °C, but with a narrower shrinkage interval. In the former sample, the intensive shrinkage between ~900 °C and ~1050 °C is followed by a plateau, which is tentatively ascribed to the chemical homogenization of the solid solution and/or pyrochlore-to-perovskite transformation. In the Mech, the shrinkage quite uniformly increases until the melting point at 1318 °C [107].

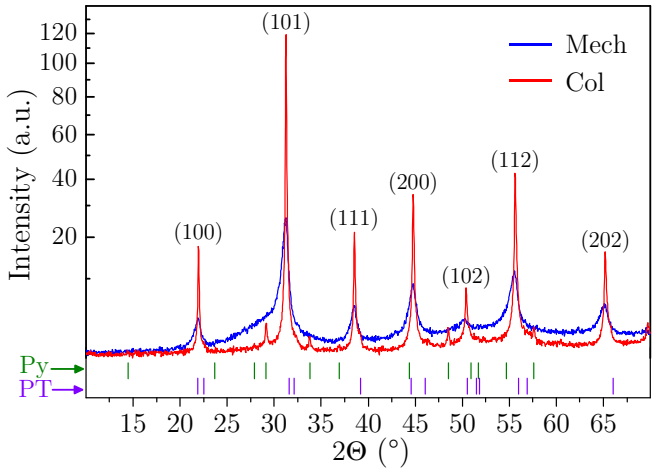


Figure 4.21: The XRD patterns of the Mech (blue) and Col (red) powders. The peaks, denoted with Miller indices, correspond to the PMN[16] (JCPDS 81-0861). Green and violet tick marks correspond to the peak positions of the cubic $Pb_{1.86}Mg_{0.24}Nb_{1.76}O_{6.5}$ (Py; JCPDS 82-0338) and tetragonal PT (JCPDS 078-0299), respectively. Note the square-root scale of the y-axis. Data from Figure 4.1 and Figure 4.14.

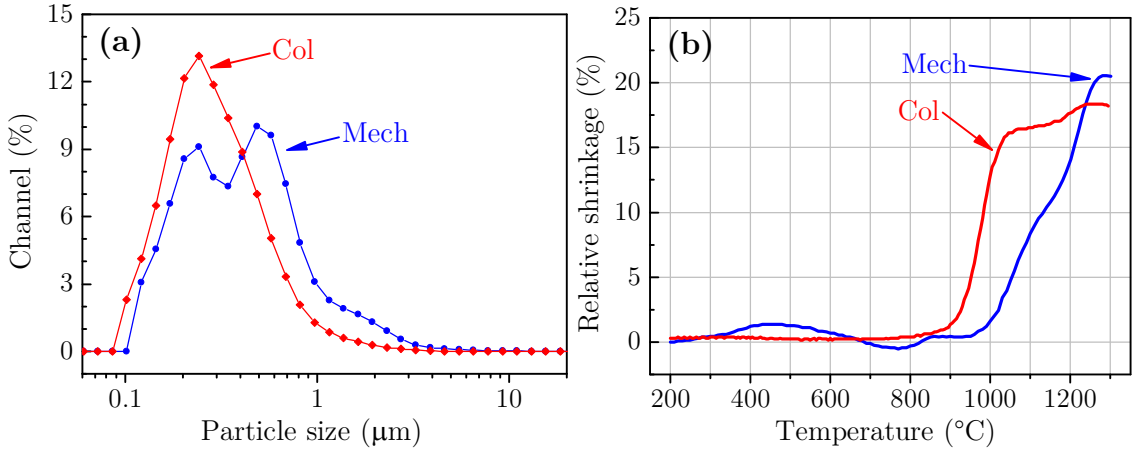


Figure 4.22: (a) The particle size distributions and (b) the dynamic sintering curves of the Mech (blue) and Col (red) powders. Lines are a guide for the eye. (a) Data from Figure 4.2 and Figure 4.15. (b) Data from Figure 4.3 and from Figure 4.16.

We decided to compare the EC properties of the ceramics with similar densities and grain sizes of about 5.0 µm, which exhibit the highest EC coefficient, $\Delta T_{EC}/E$. The respective microstructures are collected in Figure 4.23. Note that these samples were prepared with different thermal budgets, i.e., sintering at 1200 °C for 2 h and 16 h, respectively, for the Col and Mech samples. Both samples had RD exceeding 96 % and crystallized in a pure perovskite phase, cf. Figure 4.4 (a) and Figure 4.16 (b). We carefully compared the microstructures, as different sintering times could result in the evaporation of lead oxide and consequent a loss of stoichiometry. Furthermore, three ions occupy the B sites of the perovskite lattice, so the chemical homogeneity of the two samples was also compared.

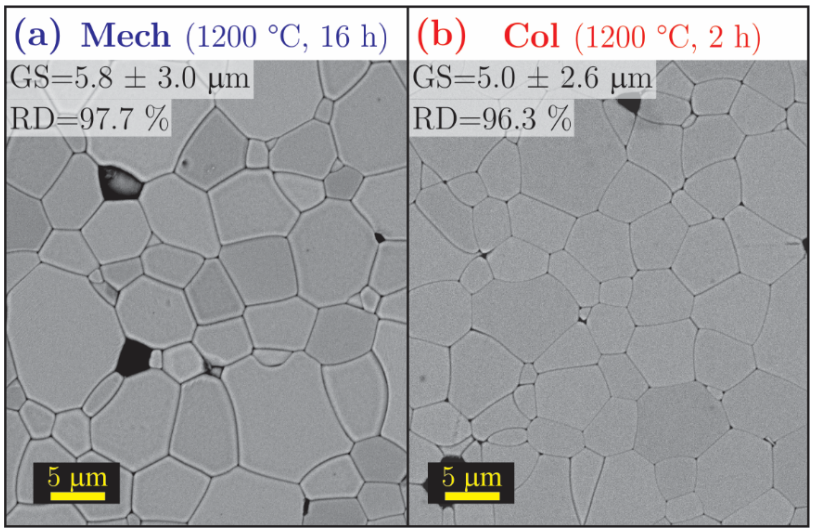


Figure 4.23: The FE-SEM micrographs of the thermally etched surfaces for (a) Mech and (b) Col ceramics with comparable grain sizes. Sintering conditions, RD and average grain sizes are added. Figures and data are from Figure 4.5 and Figure 4.17.

WDXS analysis of the Mech and the Col ceramics revealed that the materials had comparable chemical compositions, see Table 4.6. For example, the amount of Pb is ~20.3 at% in both cases. The calculated A:B ion ratios are 1.003 ± 0.011 and 1.007 ± 0.029 for the Mech and the Col ceramics, respectively. Nevertheless, we observe a lower deviation of Pb, Nb and Mg concentrations in the Mech sample, as evident from Figure 4.24. Scattering of the Pb concentration around its average value is more pronounced in the Col sample than in Mech, and it results in a three-times-larger standard deviation of Pb in the former sample. Note that we could not prepare the Col sample for a detailed TEM-EDXS analysis, cf. Section 4.2.1; therefore, we could not compare the chemical composition and/or possible presence of secondary phases of the two samples on a nm scale.

Table 4.6: Chemical composition and the standard deviation (STDEV) of the Mech and Col ceramics, determined by WDXS. Data of Col sample are from Table 4.4.

	Nominal Composition	Mech GS = 5.8 µm		Col GS = 5.0 µm	
Element	at.%	at.%	STDEV	at.%	STDEV
Pb	20	20.34	0.13	20.31	0.33
Mg	6	6.34	0.11	6.08	0.15
Nb	12	12.02	0.09	12.20	0.12
Ti	2	1.92	0.03	1.89	0.03
O§	60	60.01	0.07	60.11	0.09

§ – calculated from the stoichiometry.

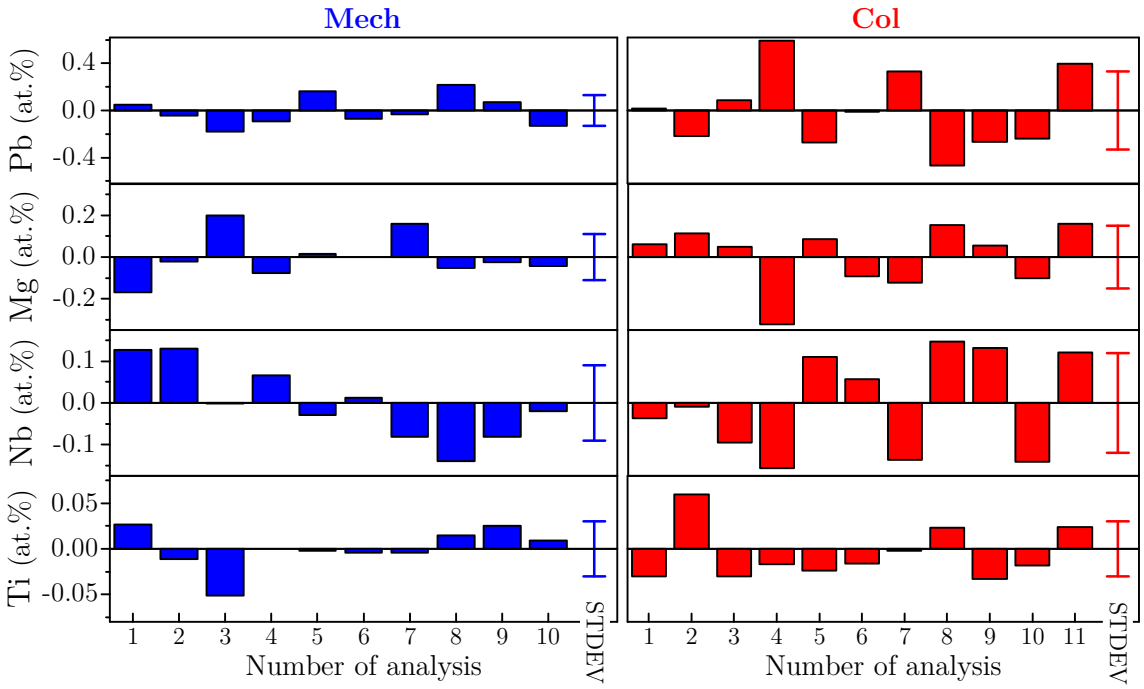


Figure 4.24: Deviation of the concentration for individual elements with regard to their average concentrations, determined by WDXS, see Table 4.6. The results are given together with the standard deviation (STDEV) for the Mech and Col ceramics. The analyses were performed on the grain interiors.

4.3.2 Dielectric and EC Properties

Figure 4.25 shows the dielectric permittivity ε' as a function of temperature for the Mech and Col ceramics. Both samples exhibit a dielectric permittivity maximum at 47 °C at 1 kHz, irrespective the synthesis method. However, the ε'_{max} of the Mech reaches 30,900, which is for ~10 % higher than the value obtained for Col ceramics, see the inset in Figure 4.25. A higher dielectric permittivity of the Mech is most probably related to the high level of chemical homogeneity, introduced by the mechanochemical synthesis of the powder [109]. In a study of $Pb(Sc_{0.5}Nb_{0.5})O_3$ ceramics it was shown that the mechanochemically treatment introduced a higher level of chemical homogeneity than the conventional solid-state synthesis in the respective materials, as evidenced by HR-TEM [113].

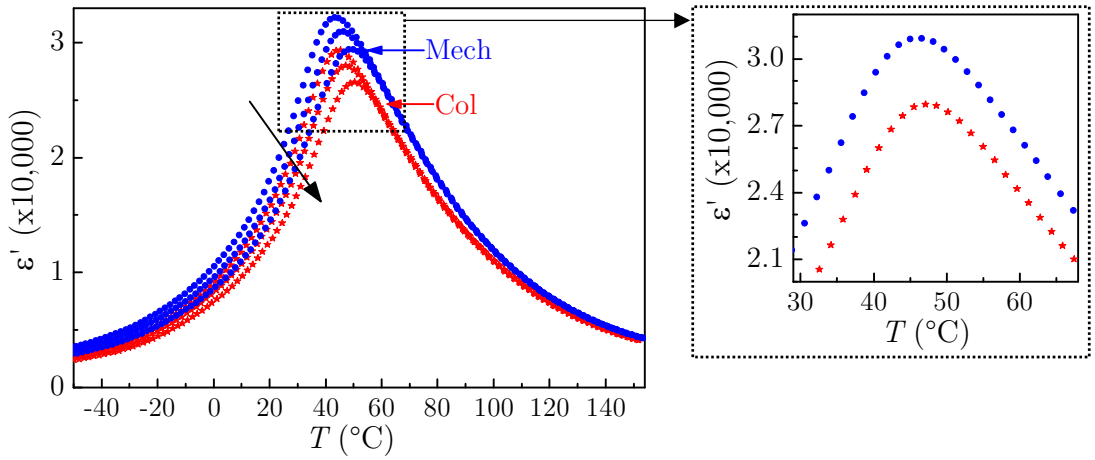


Figure 4.25: Temperature dependence of the ε' at 0.1, 1, and 10 kHz for the Mech (blue circles) and Col (red stars) ceramics. The arrow indicates the increasing frequency. Inset: smaller scale of the $\varepsilon'(T)$ at 1 kHz. Data from Figure 4.7 and Figure 4.18.

We should also not neglect the possible influence of the impurities, introduced by milling. In the Mech sample W and Zr were detected in the concentrations equal to 0.04 % and 0.02 %, expressed in moles per mole of PMN-10PT, respectively. The amount of Zr in the Col powder was about 20 times larger than in the Mech sample. According to [114] the PMN-13PT containing 1 % of WO_3 displayed a stronger frequency dispersion of $\varepsilon'(T)$, a downward shift of T_m and increased ε'_{max} than the stoichiometric material. A similar effect of W addition was observed in $Pb_{0.85-x}Ba_{0.15}[(Zn_{1/3}Nb_{1/3})_{0.7}Ti_{0.3})]_{1-x}W_xO_3$ with $0<x<0.05$ [115]. The material with 1 mol% of W showed a stronger frequency dispersion of $\varepsilon'(T)$ and possessed an ~15 % higher ε'_{max} at 1 kHz than the W-free material. In contrast, the addition of 1 vol% of YSZ to $[Pb_{0.98}Ba_{0.01}][(Zr_{0.53}Ti_{0.47})_{0.98}Nb_{0.02})O_3$ contributed to an ~20 % lower dielectric permittivity peak [116]. Therefore, we cannot exclude the possibility that 0.04 mol% of W in the Mech could slightly enhance the dielectric properties. Furthermore, 0.42 mol% of Zr in the Col could slightly deteriorate the dielectric properties of the former sample.

The $P-E$ loops of the Mech and Col samples, collected in Figure 4.26, reveal the following differences between the samples:

(*i*) The Mech ceramic exhibits a few percent higher polarization values than the Col. For example, the P_s are 34.4 μC/cm² and 33.5 μC/cm² at 60 kV/cm for the Mech and Col ceramics, respectively. A higher polarization of the Mech ceramics is in good agreement with the higher dielectric permittivity (see Figure 4.25).

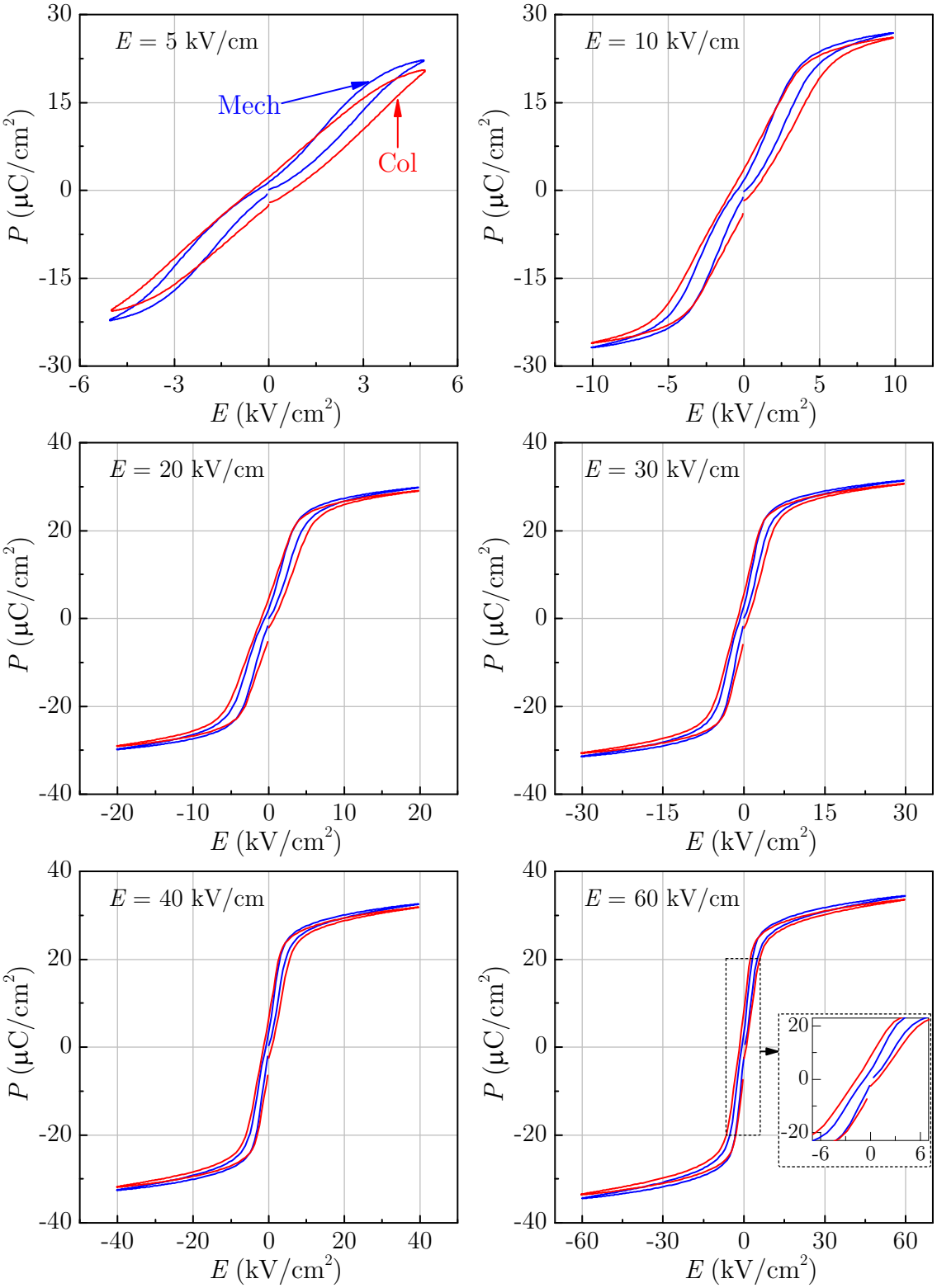


Figure 4.26: The polarization-electric field hysteresis loops for the Mech (blue line) and Col (red line) ceramics. The measurements were performed at 27 °C, 1 Hz and at different electric field amplitudes. Note the different scales of the x- and y-axes.

(*ii*) The Mech displays slightly slimmer $P-E$ hysteresis loops than the Col ceramic. This can be clearly seen at 5 kV/cm as well as at 60 kV/cm, see the inset in Figure 4.26. Furthermore, the hysteresis loops of the Mech ceramic are slightly pinched. The shape of the $P-E$ loop depends on several factors such as the grain and domain size, mechanical stresses during the domain switching, the presence of defects, etc. [5], [117], [118].

Pinching could be related to the coexistence of the polar and non-polar phases[18] [119], [120], or the presence of defects such as charged oxygen vacancies [117], [118], [121]. The critical point of the PMN-10PT is in the vicinity of the T_{room} [110]; therefore, it seems that coexistence of the polar and non-polar phases could be possible. However, then the pinching effect would be expected in both the Mech and Col samples.

The PFM analysis of the Mech and Col samples provided information about their domain structure. The examples of the topography and the PFM out-of-plane amplitude images are shown in Figure 4.27. The PFM investigations reveal that both samples possess a similar domain morphology, i.e., irregularly shaped domains. By comparing the size of the domains some differences can be noticed – the Mech sample possesses from a few tens to a few hundreds of nanometer sized domains, while in the Col sample the domains with the sizes from ~0.5 µm to over 1 µm were identified.

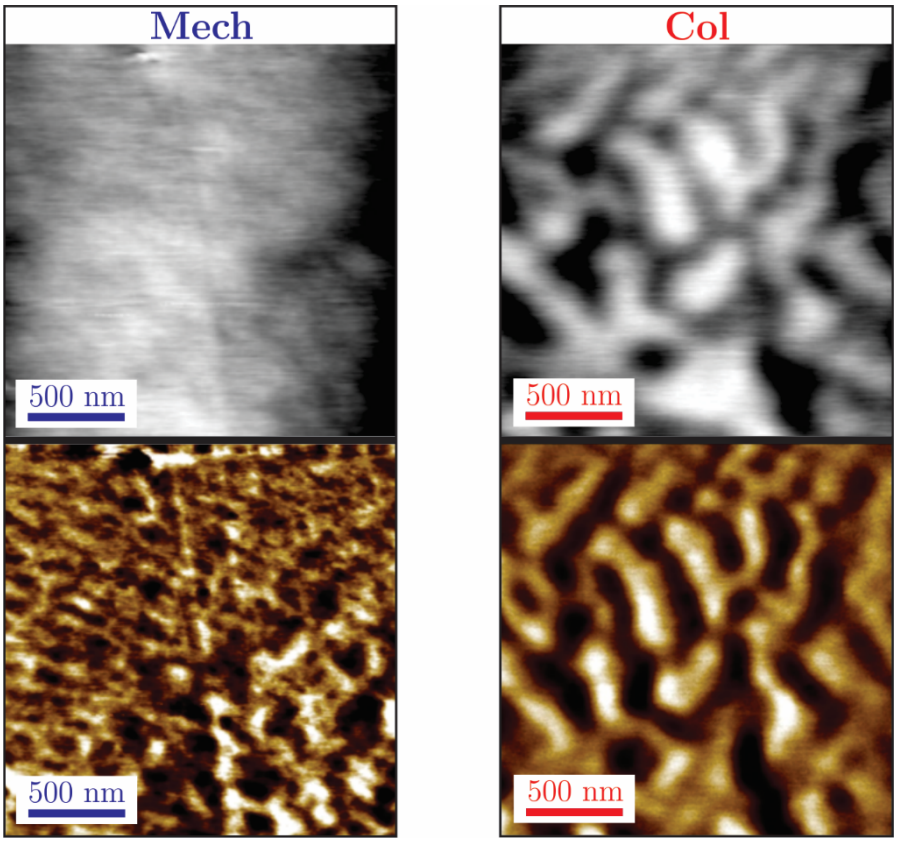


Figure 4.27: The topography images (above) and the out-of-plane amplitude PFM images (below) of the as-sintered Mech and Col ceramics.

[18] In [119] it was shown that $Pb(Sc_{0.5}Ta_{0.5})O_3$ exhibits a ferroelectric square hysteresis loop at -4 °C. However, at 6 °C, i.e., just above the first-order phase transition the material exhibits a pinched hysteresis loop implying the coexistence of polar and non-polar phases. This means that under a high electric field, a ferroelectric state can be induced in a material at a temperature above the first-order-transition curve but when the electric field approaches zero during the hysteresis measurement the induced macro-domain state disappears, resulting in a ″pinched″ hysteresis loop.

The domain morphology is also evident in the topography image. Here, it should be mentioned that the AFM or PFM provide us with information about the surface layer, which may differ from the interior of the sample. Namely, the depth-resolved synchrotron radiation provided evidence that in the surface layer of a PMN-20PT single crystal the cubic-to-rhombohedral phase transition occurs, while the interior of the sample remains cubic [122].

We observe that the different domain sizes of the two samples correspond well with the respective widths of the $P-E$ loops, i.e., the Mech sample with finer domains has got a slightly slimmer $P-E$ loop than the Col sample (see Figure 4.26). Different domain sizes could be related to different levels of ordering of the B-site ions, which presumably stem from different synthesis methods. Similarly, Uršič et al. [113] showed that the level of B-site ordering in the $Pb(Sc_{0.5}Nb_{0.5})O_3$ ceramic depends on the synthesis route. In the case of PMN-10PT only single crystals were investigated by PFM. The studies revealed that the characteristic domain size was in the range of 100 nm to 200 nm [123], [124].

In order to observe the domain structure after the application of the electric field the samples were poled by a dc field of 42 kV/cm and then reinvestigated with the PFM, see Figure 4.28. At such a field the PMN-10PT exhibited a ΔT_{EC} of ~0.9 °C, see Figure 4.19.

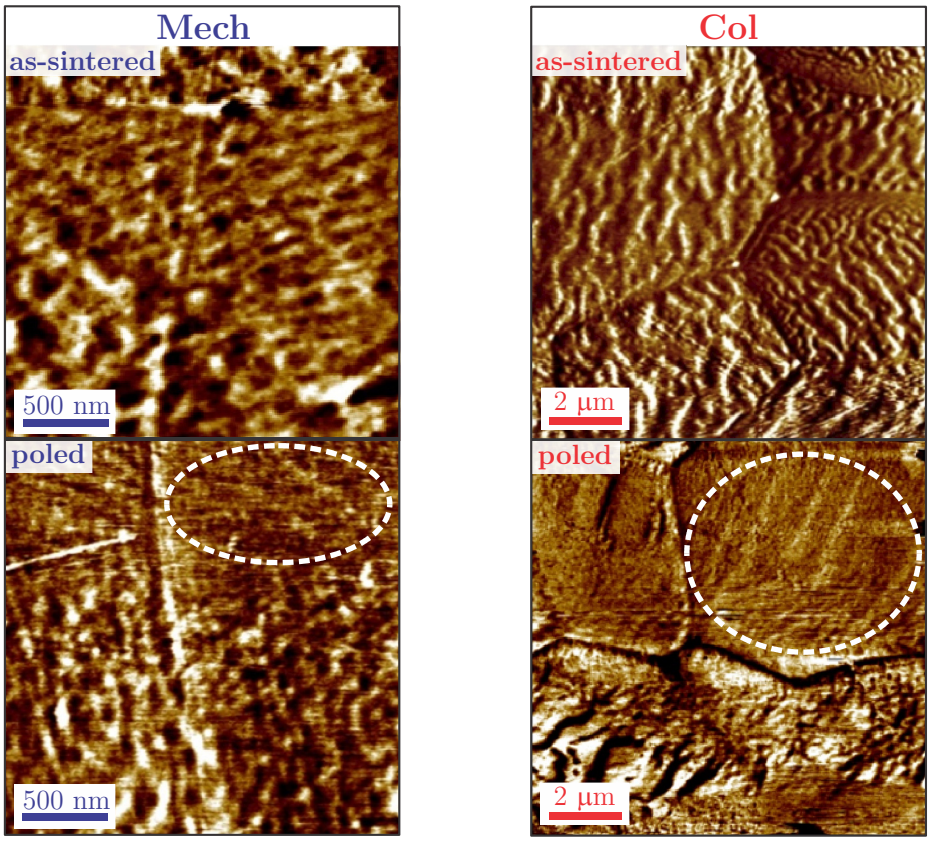


Figure 4.28: The out-of-plane amplitude PFM images, before and after poling for the Mech and Col ceramics. Note the different scales. The dashed circles indicate the areas in the poled samples with a lower number of domains.

The PFM-analyses of the different sample areas revealed the impact of poling in the Mech as well as in the Col samples. We could observe some areas with a number of domains, comparable to the one in the as-sintered samples, and other areas where the number of domains is considerably lower than in the as-sintered samples, see the dashed circles in Figure 4.28. These observations are in a good agreement with the $P-E$ hysteresis loops,

which display a non-zero remnant polarization after the removal of the electric field, see Figure 4.26.

The results of the direct and indirect EC measurements for the Mech and Col ceramics are presented in Figure 4.29. A comparison of the directly measured ΔT_{EC} values does not reveal any significant differences between the samples at electric fields of $\leq$57 kV/cm.

On the other hand, if the indirectly measured ΔT_{EC} values are compared a slight difference can be observed between the samples, as already commented on in Section 4.2.3. Namely, the ΔT_{EC} values of the Col sample are slightly lower that the ones of the Mech. As the indirectly estimated ΔT_{EC} is extracted from the $P(E,T)$ data, this is in a good agreement with slightly lower polarization values displayed by the Col sample (see Figure 4.26).

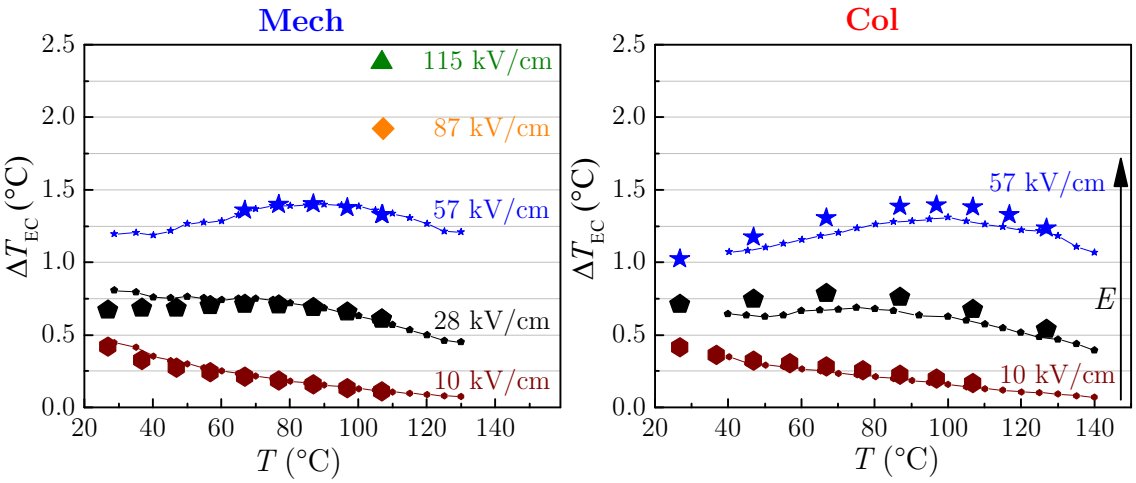


Figure 4.29: The $\Delta T_{EC}(T)$ at a few selected electric fields for the Mech and Col ceramics. The larger and smaller symbols represent the results of the direct and indirect EC measurements, respectively. Lines are a guide for the eye. The arrow indicates the increase in the electric field. Data are partially extracted from Figure 4.10 and Figure 4.20.

The Mech sample withstood the electric field of 115 kV/cm without experiencing any dielectric breakdown, while the Col broke at ~60 kV/cm. Consequently, a considerably higher ΔT_{EC} was achieved in the Mech than in the Col ceramic, 2.37 °C (115 kV/cm) as opposed to 1.39 °C (57 kV/cm). But why does the Mech ceramic withstand approximately two-times higher electric fields than the Col ceramic, although the materials have similar densities and grain sizes? The thicknesses of the investigated samples and the areas of the electrodes were similar, hence the impact of the measurement conditions could be excluded. Furthermore, Joule heating was not detected during the direct EC measurements, irrespective of the synthesis method and of the temperature and the applied electric field.

According to the literature, the dielectric breakdown occurs through the specimen, where the tunneling current has got the least resistance, i.e., through defects, pores, grain boundaries, etc. [50], [54], [55]. Based on the FE-SEM investigations both samples have homogeneous microstructures; however, the level of chemical homogeneity is slightly higher in the Mech. In addition, we should not neglect the possible influence of the W and Zr impurities on the dielectric breakdown strength. Namely, some previous studies of PMN-PT [93], [125], [126] have shown that acceptor dopants such as Mn^{2+} significantly reduce the $tan\delta$ of the material. Consequently, the dielectric breakdown strength may increase [93].

4.3.3 Summary

The influence of the processing on the EC response of the PMN-10PT ceramics was addressed in this section. The ceramics, prepared from the powders synthesized either by mechanochemical (Mech) or columbite (Col) routes, were compared. The ceramic samples had similar densities and microstructures, but the choice of the processing route introduced different levels of compositional deviation in the solid solutions, as evidenced by the WDXS, and different levels of impurities introduced by the wear of the milling media.

The Mech sample exhibits a slightly higher maximum dielectric permittivity and saturated polarization and slimmer polarization-electric field loops than the Col. The PFM analysis revealed that the domain size in the former sample is finer, which could explain its enhanced ferroelectric response.

The EC temperature changes of both samples at moderate electric field amplitudes, $\leq$57 kV/cm, are comparable. However, the Mech sample could withstand almost two-times higher electric fields without any dielectric breakdown than the Col, thus reaching the ΔT_{EC} of 2.37 °C. The observed enhanced performance of the Mech sample could be related to a higher level of chemical homogeneity, but a possible influence of the impurities on its properties cannot be neglected.

4.4 Energy Efficiency of an Electrocaloric Cooling System with (1-x)Pb($Mg_{1/3}Nb_{2/3}$)O_3-x$PbTiO_3$ Ceramics

In this section we analyze and discuss the energy efficiency of an EC cooling system in which the PMN-100xPT (x = 0, 0.1 and 0.35) ceramics are subjected to a thermodynamic cycle. A special focus is devoted to the influence of the $P-E$ hysteresis losses of the EC material and electric-energy regeneration on the energy efficiency of an EC cooling system. The energy-efficiency analysis was made in collaboration with Uroš Plaznik, Prof. Alojz Poredoš and Assoc. Prof. Andrej Kitanovski from the University of Ljubljana, Faculty of Mechanical Engineering, Laboratory for Refrigeration and District Energy. The results are published in a common paper [97].

4.4.1 Electrocaloric Material in a Thermodynamic Cycle

The principle of the EC cycle and the basic idea of EC cooling have already been discussed in Section 1.2.2. Let us upgrade this idea to the simple EC cooling system that is presented in Figure 4.30. It consists of a heat exchanger adjacent to a heat source (cold heat exchanger; CHX), a heat exchanger adjacent to a heat sink (hot heat exchanger; HHX), and of the EC material that can be moved from the heat source to the heat sink and vice versa.

During the operation of the EC system the heat is transferred between the system and its surroundings and the work is done on the system or by the system. The work performed on the system is the electrical work that is done on the EC material, i.e., work that is needed to charge the EC capacitor and is given as the work density $W = \int E \times dD$, see Eq. (1.16) [30].

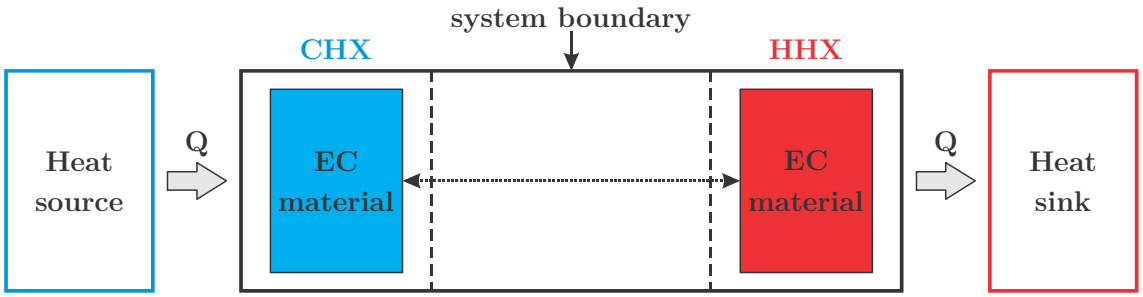


Figure 4.30: Schematic representation of a simple EC cooling system, consisting of the cold heat exchanger (CHX) adjacent to a heat source, the hot heat exchanger (HHX) adjacent to a heat sink, and the EC material that is in contact with the CHX or the HHX.

Note that in a real application there are other effects that can additionally contribute to the work done on the EC cooling system, e.g., energy needed to move the EC element from CHX to HHX and vice versa, friction, irreversibilities due to the heat transfer, etc. Such contributions reduce the cooling power of the EC system; however, in the frame of the analysis we will only focus on the electrical work done on the EC material and assume that the cooling energy of the EC system is equivalent to the cooling energy of the EC material. Let us discuss the thermodynamic cycle for the EC cooling system shown in Figure 4.30 that consists of four processes.

1^{st} process: The EC element is in contact with the HHX and the electric field is increased from the $E_1 = 0$ to the $E_2 > E_1$ under adiabatic conditions, hence, the material is polarized and it heats up due to the EC effect, but no heat is transferred from the EC material to

its surroundings. According to Eq. (1.16) some work is done on the system during this step.[19]

If the EC material does not display the $P-E$ hysteresis losses, i.e., the area between the polarization and depolarization curves in the $P(E)$ diagram, further denoted as losses, and if other possible origins of the internal entropy generation are neglected, no entropy is generated during this process. Because the total entropy of the system remains constant the process is isentropic, and it is represented with a vertical line on the $T(S)$ diagram (Figure 4.31, process 1-2a). On the other hand, if the EC material exhibits losses, some entropy, denoted as ΔS_H, is generated by application of E_2 (see Figure 4.31, process 1-2).

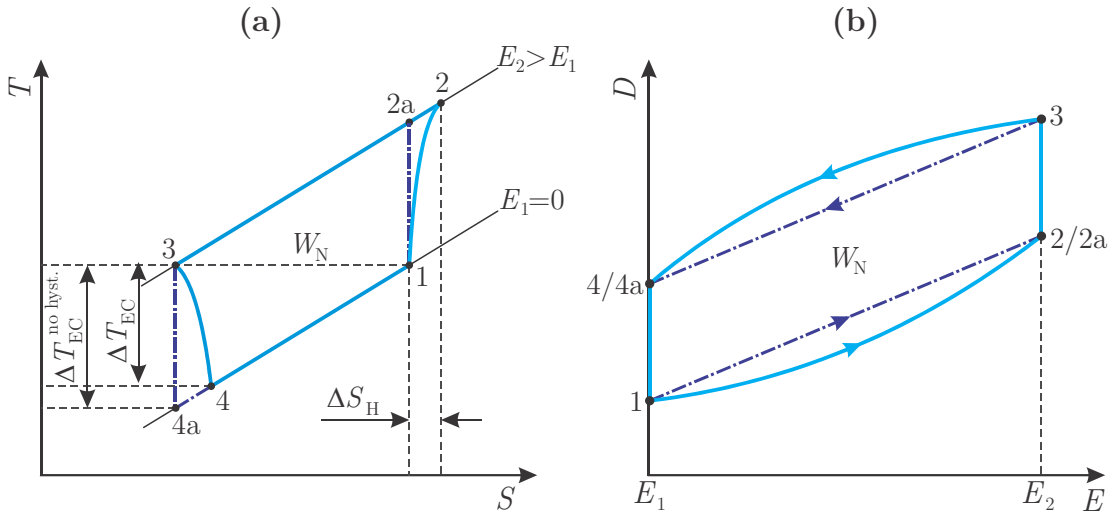


Figure 4.31: Schematic representation of the thermodynamic cycle to which the EC material is subjected in the EC cooling system from Figure 4.30. (a) $T-S$ diagram. (b) $D-E$ diagram. W_N – net work density.

2nd process: The heat is transferred from the EC material to the heat sink at a constant electric field E_2 and the temperature of the EC material relaxes back to the initial temperature (Figure 4.31, stage 2/2a-3). The polarization of the EC material is a function of temperature, hence, it increases as the temperature of the EC material decreases[20] (for example see Figure 4.9 b). Because the dielectric displacement D increases as well, some work is done on the system. Furthermore, since during the process 2/2a-3 the electric field is applied to the EC material, a leakage current, if it is present, generates the detrimental Joule heating and additionally contributes to the work done during the second process. For this reason the electrical resistivity of the EC material should be as high as possible.

3rd process: The EC material is moved from the HHX to the CHX. Note that the work needed to move the EC element and other possible irreversibilities like friction during this movement are neglected. In the third process (Figure 4.31, process 3-4/4a) the EC material is in contact with the CHX and the electric field decreases back to $E_1 = 0$ under adiabatic conditions. If the EC material displays losses, some entropy is generated by the removal of the electric field, and the material cools down by ΔT_{EC}, in analogy with the first process. On the other hand, if the material does not exhibit any losses, the total entropy of the system remains unchanged and the EC material cools down by $\Delta T_{EC}^{no\ hyst.}$ as the electric field is removed.

[19] Note that for the materials with $\varepsilon' \gg 1$ such as ferroelectrics and relaxors the $P \approx D$.

[20] It is assumed that in the studied temperature interval the EC material does not exhibit any phase transition.

4^{th} process: The heat is transferred from the heat source to the EC material, and the EC material heats up to the initial temperature, see Figure 4.31, process 4/4a-1. In contrast to the second process, the polarization P (and dielectric displacement D) of the material decreases. Note that the fourth process occurs at $E_1 = 0$; therefore, despite the change in D, no work is performed by the system according to Eq. (1.16). In addition, no leakage current flows.

The net work done on the system is equal to the work performed on the EC material, which was subjected to a thermodynamic cycle. If the leakage current is negligibly small the net work density (W_N) is expressed as:

$$W_N = \int_{E_1}^{E_2} E\, dD = W_{1-2/2a} + W_{2/2a-3} + W_{3-4/4a}. \tag{4.1}$$

By applying the first law of thermodynamics to the system, the following expression is obtained:

$$W_N = -(Q_{2/2a-3} + Q_{4/4a-1}), \tag{4.2}$$

where $Q_{2/2a-3}$ is the heat density transferred from the system to the heat sink and $Q_{4/4a-1}$ is the heat density transferred from the heat source to the system. By considering Eq. (4.1) and (4.2) it can be seen that in the first two processes of the thermodynamic cycle, i.e., $W_{1-2/2a}$ and $W_{2/2a-3}$, the work is done on the system, and in the third process, i.e., $W_{3-4/4a}$, the work is done by the system (depolarization of the EC capacitor). Here, it should be noted that in a real application, the work that is done by the system in the third process represents some potential electric energy that could be recovered during the depolarization of the EC material. In fact this is the electric energy that has been used for charging the EC material. For such purposes a special electric circuit should be employed, such as shown in [127], where 82 % of the electric energy was recovered.

Since some energy losses in such a circuit are inevitable, we introduce a degree of electric-energy recovery (n), which indicates the amount of the available electric energy during the discharge of the EC material, which has been successfully recovered. By considering the electric-energy recovery, Eq. (4.1) can be rewritten as:

$$W_{N,R} = W_{1-2/2a} + W_{2/2a-3} + \frac{n}{100} \times W_{3-4/4a}, \tag{4.3}$$

where $W_{N,R}$ is the net work density done on the system, when n of the electric-energy has been recovered. The combination of Eq. (4.1), (4.2) and (4.3) gives the following expression:

$$W_{N,R} = -(Q_{2/2a-3} + Q_{4/4a-1}) - W_{3-4/4a} \times \left(1 - \frac{n}{100}\right). \tag{4.4}$$

In order to determine the $W_{N,R}$, we define the Q_{2-3}, Q_{4-1} and $W_{3-4/4a}$. Next, the heat density crossing the boundary of the system is defined as:

$$Q_{2/2a-3} = c_E \times \rho \times (T_3 - T_{2/2a}), \text{and} \tag{4.5}$$

$$Q_{4/4a-1} = c_E \times \rho \times (T_1 - T_{4/4a}). \tag{4.6}$$

According to Figure 4.31 and Eq. (1.19) the $W_{3-4/4a}$ is expressed as:

$$W_{3-4/4a} = \int_{E_2}^{E_1} EdD \tag{4.7}$$

As can be seen from Eq. (4.5)–(4.7) the $W_{3-4/4a}$ is determined from the data of the $D(E)$, while the Q_{2-3} and Q_{4-1} are calculated from the specific heat capacity at zero electric field c_E, density ρ and the temperature of the material in intermediate steps of the thermodynamic cycle. According to Figure 4.31 the temperature of the intermediate stage of the thermodynamic cycle is determined by knowing the ΔT_{EC} and $\Delta T_{EC}^{no\ hyst.}$ for a random initial temperature T. Note that the ΔT_{EC} is the experimentally determined value, while the $\Delta T_{EC}^{no\ hyst.}$ represents the ″ideal″ EC temperature change, which would have been reached for the material with no losses.

The $\Delta T_{EC}^{no\ hyst.}$ can be determined as follows. With regard to Figure 4.31 (a), the dipolar entropy density change is written as:

$$\Delta S_P = \Delta S_{1-4a} = \Delta S_{1-4} + \Delta S_H. \tag{4.8}$$

By applying the second law of thermodynamics the ΔS_P of the EC material is expressed via the measured ΔT_{EC} [128]:

$$\Delta S_P = c_E \times \rho \times \ln\left(\frac{T}{T - \Delta T_{EC}}\right) + \Delta S_H, \tag{4.9}$$

where T is the initial temperature.

The ΔS_H is calculated from the $P(E)$ data as described in ref. [129]:

$$\Delta S_H = \int \frac{P_{IRR} \times dE}{2T}, \tag{4.10}$$

where P_{IRR} is the irreversible polarization function. Now, the $\Delta T_{EC}^{no\ hyst.}$ of the EC material at any initial temperature T is determined as:

$$\Delta T_{EC}^{no\ hyst.} = T \times \left(e^{\frac{\Delta S_H - \Delta S_P}{c_E}} - 1\right). \tag{4.11}$$

The efficiency of a cooling system is often described by the coefficient of performance (COP), which is defined as the ratio between the heat density that is transferred from the heat source to the system (Q_C), and the work density W done on the system to transfer this heat [59], [130]:

$$COP = \frac{|Q_c|}{|W|}. \tag{4.12}$$

Eq. (4.12) reveals that the less the W that is required to achieve a given transfer, the greater the COP and the more efficient the refrigerator. Because the Q_C is transferred from the heat source to the system, and the W is done on the system, the energy density transferred from the system to the heat sink is $|Q_H| = |Q_C| + |W|$ [59]. By applying Eq. (4.12) on the system in Figure 4.31 the COP is expressed as:

$$COP = \frac{Q_{4/4a-1}}{W_{N,R}}. \tag{4.13}$$

In order to compare the COP of the system under investigation, calculated according to Eq. (4.13), with the coefficient of performance of the Carnot heat pump (COP_C)[21], we define the exergy efficiency ξ as [130]:

$$\xi = \frac{COP}{COP_C} \times 100, \tag{4.14}$$

4.4.2 Energy Efficiency of the EC Cooling System Employing PMN-100xPT (x=0, 0.1 and 0.35)

The equations from the first part are applied to the study of the energy efficiency of an EC cooling system employing the PMN-100xPT ceramics with x = 0, 0.1 and 0.35. The PMN is a prototype relaxor material, PMN-35PT is an MPB ferroelectric composition, and the PMN-10PT is a material that is especially interesting for an EC cooling application that operates near T_{room}. The respective materials exhibit different $P-E$ characteristics, see Figure 4.32. The P_s of PMN, PMN-10PT and PMN-35PT are ~16 µC/cm^2, ~30 µC/cm^2 and ~38 µC/cm^2 at 20 kV/cm, respectively. From the different $P-E$ dependences it follows that different amounts of energies are needed in order to charge the respective EC capacitors. Moreover, since the losses represent the electric energy that cannot be recovered, it is expected that the losses could have a great impact on the energy efficiency of the studied materials.

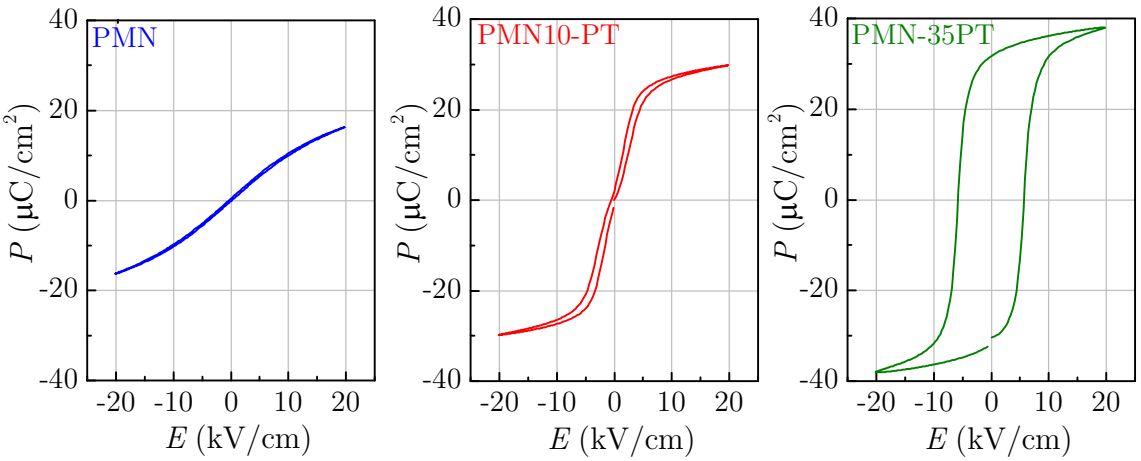


Figure 4.32: The $P-E$ hysteresis loops for the PMN, PMN-10PT and PMN-35PT ceramics, measured at 27 °C, 1 kHZ and 20 kV/cm.

The PMN-100xPT samples were prepared by mechanochemical synthesis and sintering as described in Section 3.2.12. The $P-E$ measurements were performed under conditions corresponding to the process 1-2/2a and the process 3-4/4a in Figure 4.31, i.e., by application of a unipolar electric signal. The results of the $P-E$ obtained at 27 °C and ~55 kV/cm are shown in Figure 4.33.

[21] It is assumed that the Carnot heat pump works between the temperatures at which the heat is exchanged between the system and the heat source and sink, respectively.

The polarization and depolarization curves of the PMN ceramic coincide, meaning that this material does not display any losses. The P_s approaches 25 µC/cm^2. On the other hand, the PMN-10PT ceramic displays a slightly wider $P-E$ hysteresis loop than PMN; however, the saturated polarization reaches a substantially higher value of ~33 µC/cm^2. In agreement with the highest dielectric permittivity among the studied materials (see Figure 1.10), the PMN-35PT ceramic exhibits the highest P_s of ~52 µC/cm^2 and also the widest $P-E$ hysteresis loop.

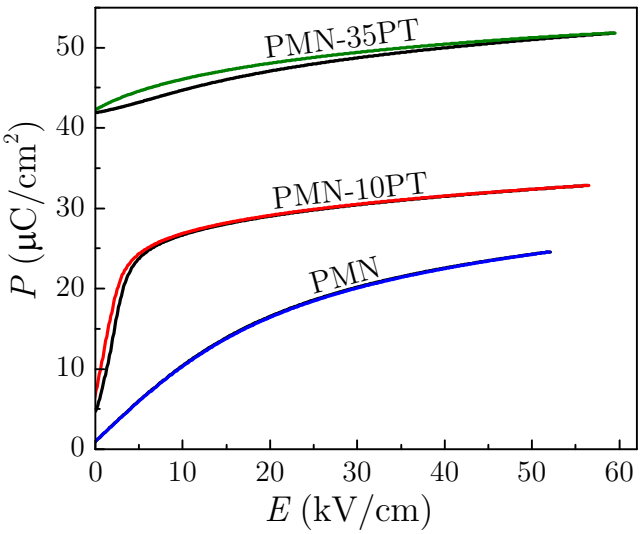


Figure 4.33: $P-E$ curves for the PMN, PMN-10PT and PMN-35PT ceramics. The measurements were performed at 27 °C and ~55 kV/cm and a unipolar and triangular electric signal with rise and fall times of 50 ms was used (see Figure 3.4). Ten or more cycles were applied to the sample so that repeatable results were obtained.

For the energy-efficiency analysis the heat sink was set at 27 °C. It was assumed that the specific heat capacity c_E, the dipolar entropy change ΔS_P and the entropy generation due to the losses ΔS_H of the studied PMN-PT compositions are constant in the studied temperature range in which the system operates. This is a good approximation for PMN-PT materials, as in the vicinity of T_{room} the phase transitions are not expected [27], [62], [111], [131]. The c_E values at zero electric field and at 27 °C were calculated from the DSC measurements (see Appendix B), and the ΔT_{EC} at ~55 kV/cm and 27 °C were extracted from the direct EC measurements, performed in a high-resolution calorimeter, see Section 3.2.12.

The results of the energy-efficiency analysis for the PMN, PMN-10PT and PMN-35PT ceramics are presented in Figure 4.34, where the ratio ξ is presented as a function of the degree of the electric-energy recovery, n. In order to investigate the influence of the losses on the efficiency of the system, the analyses were performed by neglecting the $P-E$ losses ($\Delta S_H = 0$) and by taking them into account. In the latter case the ΔS_H was calculated from the experimental data in Figure 4.33 and using Eq. (4.10).

Let us first focus on the results of the first case, when no electric energy is recovered ($n = 0$) and when the losses are neglected ($\Delta S_H = 0$). The ξ is equal to 3.8 % for PMN, 2.8 % for PMN-10PT and 1.0 % for PMN-35PT, see Table 4.7. In another case, when $n = 0$ but the hysteresis loses are taken into account, the ξ reaches slightly lower values in comparison to the first case. The ξ for the PMN was 3.8 %, for the PMN-10PT it was 2.7 %, and for the PMN-35PT it was 0.9 %.

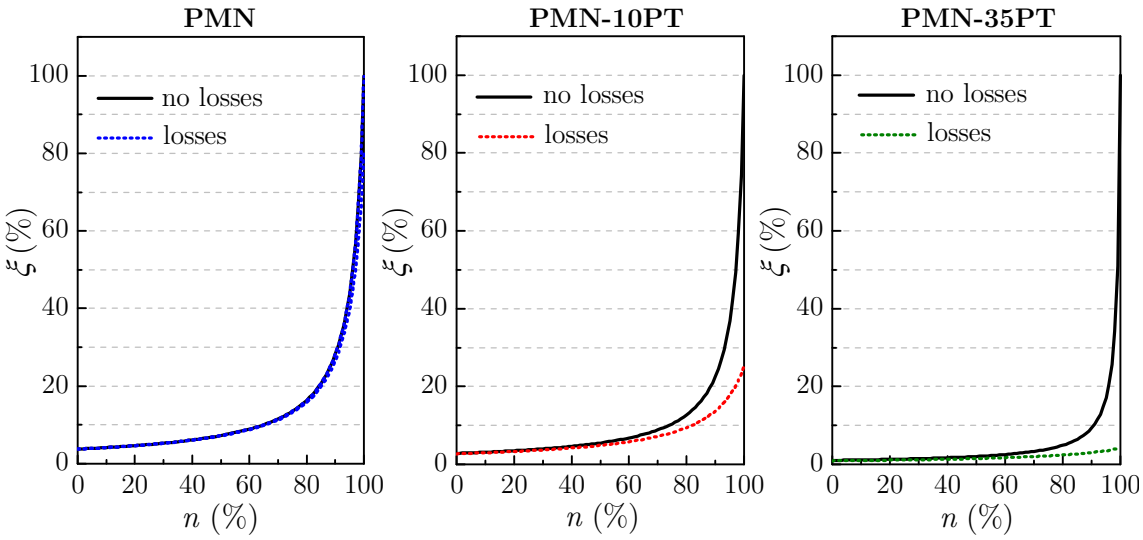


Figure 4.34: The exergy efficiency ξ of the system under investigation as a function of the degree of electric-energy recovery n for the PMN, PMN-10PT and PMN-35PT ceramics. The solid and dashed lines represent the analysis by neglecting or taking into account the $P-E$ hysteresis losses, respectively.[22]

By assuming a realistic degree of the electric-energy recovery ($n = 80$) and neglecting the losses the efficiency is significantly increased in all cases. Namely, the ξ reaches 16.4 % in case of PMN, 12.7 % in case of PMN-10PT and 4.9 % in case of PMN-35PT. This means that by recovering of the 80 % of the electric energy, the energy efficiency is improved for approximately a factor of five. This is in a good agreement with calculations by Moya et al. [36], who also reported a fivefold energy-efficiency improvement if the 80 % of the electric energy is recovered. However, the authors did not provide any details. Note that an even higher degree of the recovered electric energy ($n = 90$) would result in an energy-efficiency improvement of about 8 times, but we found no literature data on a technology that would allow such a degree of energy recovery.

Table 4.7: The exergy efficieny ξ of the EC cooling system under investigation, when losses are neglected ($\Delta S_H = 0$) and taken into account ($\Delta S_H \neq 0$). n – degree of the recovered energy. The arrow indicates the increase of ξ.

Composition	ξ(%)			
	$\Delta S_H = 0$ $n = 0$	$\Delta S_H \neq 0$ $n = 0$	$\Delta S_H = 0$ $n = 80$ %	$\Delta S_H \neq 0$ $n = 80$ %
PMN	3.8	3.8	16.4	15.8
PMN-10PT	2.8	2.7	12.7	9.4
PMN-35PT	1.0	0.9	4.9	2.4

By comparing the $\xi(n)$ curves that account for or neglect the losses for a selected composition (Figure 4.33) a great impact of the losses on ξ can be observed. In PMN, which possesses negligibly small losses the $\xi(n)$ curves almost coincide and the ξ significantly increases at high n, irrespective of whether the losses are considered. Therefore, by considering the losses and $n = 80$ the ξ of PMN is 15.8 %, which still

[22] The results of the energy-efficiency analysis, shown in Figure 4.34 were obtained by computer modeling, which was performed by Uroš Plaznik (University of Ljubljana, Faculty of mechanical engineering, Laboratory for refrigeration and district energy) [97], [139].

represents an efficiency improvement by a factor of about five. On the other hand, in the case of PMN-10PT and especially of PMN-35PT, by considering the losses the ξ does not increase so much at high n, see Figure 4.33. For example, if the losses are taken into account and $n = 80$ the ξ of PMN-10PT and PMN-35PT is 9.4 % and 2.4 %, which correspond to an improvement by a factor of ~3 and only ~2 in comparison with $\xi(n = 0)$, respectively. Note that when the losses were neglected, a fivefold energy-efficiency improvement was achieved at $n = 80$, irrespective of the studied material.

4.4.3 Summary

The PMN-35PT material possesses a promising ΔT_{EC} (see Table 1.2); however, due to its large $P - E$ losses it exhibits the lowest energy-efficiency within the studied materials. Furthermore, if the electric energy is recovered, the exergy efficiency ξ of PMN-35PT increases only slightly. On the other hand, PMN is the most energy-efficient candidate for the EC cooling applications due to its very slim $P - E$ hysteresis loop and a moderate energy that is needed for its polarization. The latter leads to low losses; therefore, performing a high degree of the energy-electric recovery in PMN and also in PMN-10PT results to a substantially enhanced energy efficiency – by a factor of about five and three if a realistic degree, i.e., 80 % of the energy is recovered, respectively. Hence, we can conclude that an EC material with a slim $P - E$ hysteresis loop and a high degree of electric-energy recovery is needed to create the basis for an efficient cooling system.

Chapter 5

Summary, Conclusions and Outlook

In the dissertation we report and discuss the results of a study on the relation between the microstructural descriptors, i.e., density, grain size, chemical homogeneity, and the electrocaloric (EC) effect of the relaxor-ferroelectric $0.9Pb(Mg_{1/3}Nb_{2/3})O_3$-$0.1PbTiO_3$ (PMN-10PT) ceramic. The ceramic powders were synthesized by two routes, mechanochemical synthesis and the frequently employed two-step columbite route. The bulk ceramic samples were prepared by atmospheric sintering, and characterized in terms of materials, dielectric and EC properties. In the following parts the studies of the ceramics prepared by the two routes are summarized and compared. Finally, in the last part the energy efficiency of an EC cooling system is discussed from the point of view of polarization-electric field hysteretic losses, which may be tuned by the choice of the material composition. The efficiency of such a cooling system is further increased by implanting the electric-energy recovery, i.e., energy needed to induce the EC effect.

In the first part we studied the influence of the grain size of the PMN-10PT ceramics on the EC response. The selected powder synthesis route, i.e., the mechanochemical synthesis via high-energy milling of the reagent oxides, resulted in a mixture of poorly crystallized perovskite and amorphous phases. The 96 h of high-energy milling contributed to contamination of the powder with tungsten due to the wear of the milling media. Additional attrition milling effectively narrowed the particle size distribution and reduced the median particle size to 0.31 µm, but also introduced traces of zirconium from the milling balls.

Single-phase perovskite ceramics were obtained by sintering the powder compacts with different thermal budgets, at temperatures of 1150 °C, 1200 °C and 1250 °C for times from 2 h to 16 h. The samples had relative densities (RD) of 97–98 % with the exception of the sample sintered with the largest thermal budget (1250 °C, 16 h), where the RD was 95.4 %.

All the samples had homogeneous microstructures without any secondary phases, with the average grain sizes between 2.8 µm and 9.4 µm. HR-TEM of the 3.6- and 9.4-µm-grain-sized samples confirmed that the grain boundaries were clean. The WDXS analysis revealed a slight lead deficiency in the ceramic sample with the coarsest grains, in agreement with its slightly lower RD, which was attributed to the sublimation of lead oxide upon extended heating at 1250 °C; while the chemical composition of the samples prepared with a lower thermal budget corresponded to the nominal composition.

The ceramic samples displayed a typical dielectric relaxor behavior, in agreement with earlier studies [78], [82]. The maximum dielectric permittivity (ε'_{max}) of ~30,000 at 1 kHz was determined for all the samples, which is a few thousands higher than the previously reported data [78], [81], [108]. Such a high value is attributed to the high level of chemical homogeneity introduced by the mechanochemical synthesis.

The dc electric field induced a ferroelectric phase, which was observed as a strong suppression of the frequency dispersion of the dielectric permittivity ε'. Simultaneously, its value drastically decreased and the dielectric anomaly experienced an upward temperature shift. For example, the ε'_{max} decreased from ~30,000 to ~3,100 as the field increased from 0 kV/cm to 25 kV/cm and the maximum shifted from 47 °C to 115 °C. As shown by Rožič et al. [88] the EC temperature change ΔT_{EC} reaches its peak value at the relaxor-to-ferroelectric phase-transition temperature, which typically takes place in the middle of the low-temperature slope of the dispersive dynamic dielectric permittivity peak. The latter relationship thus allows us to estimate the temperature of the maximum ΔT_{EC} only by measuring the $\varepsilon'(T)$ at a selected electric field. Furthermore, when considering the design of an EC cooling device, the upward shift of the ΔT_{EC} with the electric field should be taken into account.

The saturated polarization P_s increased with increasing grain size, reaching the peak value at 5.8 µm, and with a further increase of the grain size it decreases. Consequently, the largest EC coefficient $\Delta T_{EC}/E$~2.3×10^{-7} °Cm/V is obtained in the ceramic with 5.8-µm grains. Such a value is more than 10 % higher than the values obtained for the samples with finer or coarser grains. The trend of decreasing P_s in the coarse-grained ceramics is related to the lower density of the respective samples.

The dielectric breakdown strength E_b decreases with increasing grain size. The coarse-grained ceramics (>3.6 µm) did not survive the electric fields above 115 kV/cm, while the fine-grained ceramics (≤3.6 µm) withstood the largest electric field amplitude of 160 kV/cm without any dielectric breakdown or any noticeable Joule heating. The largest EC temperature change of 3.45 °C was thus obtained in the ceramic with 3.6-µm-sized grains and was attributed to the interplay between a high dielectric breakdown strength and a high saturated polarization. The obtained ΔT_{EC} exceeds the previously reported values for the PMN-PT ceramics, see Figure 5.1, and even for other Pb-based perovskites, i.e. $Pb(Zr,Ti)O_3$ [32], [33]. Moreover, such a high value is obtained far away from any multi-critical point of the material [110].

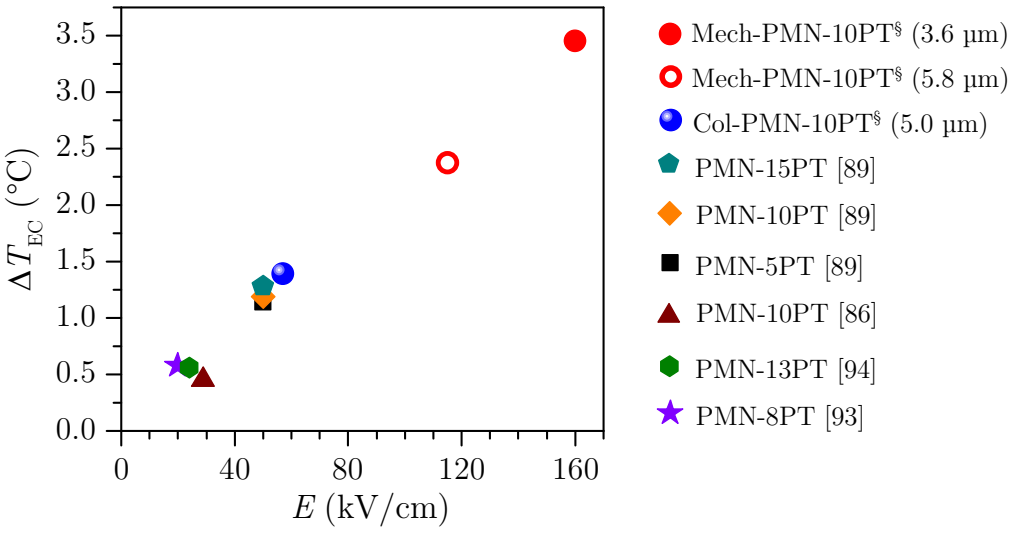


Figure 5.1: The measured ΔT_{EC} versus electric field amplitude. The data are the results of this work§ and some earlier studies on PMN-10PT or PMN-100xPT with similar compositions. Note that the measurements were performed at different temperatures. The grain sizes are included whenever reported.

The PMN-10PT ceramics were also prepared from the powder synthesized by the two-step columbite route. The respective powder was fine, with the median particle size of 0.25 µm, and it consisted of the perovskite phase with traces of $PbTiO_3$ (PT) and pyrochlore. Traces of zirconium were detected due to the wear of the milling balls. After sintering at 1200 °C for 2 h the ceramic had 96.3 % RD and a uniform microstructure with the mean grain size of 5.0 ± 2.6 µm.

The columbite-derived material, further denoted as Col, displayed a typical relaxor-like frequency dispersion of $\varepsilon'(T)$ with the maximum dielectric permittivity ε'_{max} equal to ~28,000 at 47 °C and 1 kHz. The direct EC measurements confirmed the absence of Joule heating. The largest directly measured ΔT_{EC} of 1.39 °C was reached at 57 kV/cm and 97 °C, but at slightly higher fields the dielectric breakdown occurred. The $\Delta T_{EC}/E$ was 2.4×10-7 °Cm/V, which is in a good agreement with a recent study of the columbite-derived PMN-10PT [89]. The electric field amplitude of ~60 kV/cm obtained for the Col material is still considerably higher than the ones applied in previous EC studies of the PMN-10PT ceramics or solid solutions with similar compositions, which were in all cases prepared by the columbite route [86], [89], [93], [112].

But our mechanochemically derived material with a comparable density and grain size, further denoted as Mech, survived an about two times higher electric field until the breakdown, even as high as 160 kV/cm, which consequently resulted in much higher EC temperature changes than in the case of the Col ceramic. In the next part we compared the two materials in order to elucidate the origin of such differences. The microstructures were, in both cases, uniform; however, a detailed WDXS analysis revealed that although both samples had stoichiometric compositions, i.e., the Pb/(Mg,Nb,Ti) molar ratios were ~1.005, the Mech sample exhibited a significantly lower compositional deviation than the Col.

The Mech ceramic had an about 10 % higher peak dielectric permittivity than the Col (~28,000). Furthermore, the Mech ceramic exhibited a slightly slimmer polarization-electric field ($P-E$) loop and a slightly higher saturated polarization than the Col. The piezo-response mode atomic force microscope investigations showed that the domain size in the Mech sample is markedly finer than in the latter one.

Joule heating was not detected during the direct EC measurements in either sample. The EC coefficients, $\Delta T_{EC}/E$, of the two samples were comparable. However, due to the almost two times higher dielectric breakdown strength of the Mech than the Col, the former ceramics reached a ΔT_{EC} of 2.37 °C at 115 kV/cm, i.e., an about 1 °C larger ΔT_{EC} than in the Col sample. The observed differences could be tentatively explained as a consequence of a higher level of chemical homogeneity of the Mech material, introduced by mechanochemical synthesis [109], [113]. The impurities introduced via the wear of the milling media could additionally contribute to different dielectric properties.

In the last part of the thesis we studied the energy efficiency of an EC cooling system in terms of the effect of the $P-E$ hysteresis losses (further denoted as losses) of the EC material. In addition, we considered the influence of the electric-energy recovery, i.e., the recovery of the electric energy that is needed to induce the EC effect. The respective part was performed in collaboration with Uroš Plaznik, Prof. Dr. Alojz Poredoš and Assoc. Prof. Dr. Andrej Kitanovski from the University of Ljubljana, Faculty of Mechanical Engineering, Laboratory for Refrigeration and District Energy. The results were published in a common paper [97].

For the purposes of the analysis, the (1-x)$Pb(Mg_{1/3}Nb_{2/3})O_3$-x$PbTiO_3$ (PMN-100xPT) with x = 0, 0.1 and 0.35 ceramics were characterized. PMN is considered as a prototype relaxor material, while the compositions with a large amount of PT, such as PMN-35PT, behave as ferroelectrics [10].

The $P-E$ measurements corresponding to the thermodynamic process in the EC cycle showed that the polarization values as well as the losses increase with the amount of PT. The losses of PMN are negligibly low due to the relaxor character of the material, and they progressively increase with increasing PT content.

The electric-energy efficiency analysis revealed that if no electric energy is recovered the energy efficiency of the EC system employing the investigated ceramics does not exceed 3.8 % of the efficiency of a Carnot heat pump (ξ), irrespective of the composition and also whether the losses are neglected. However, if a realistic value, such as 80 %, of the electric energy is recovered and the losses are taken into account, the energy efficiency of the studied system can be improved by a factor of up to five. In this case the ξ reaches 15.8 %, 9.4 % and 2.4 % for PMN, PMN-10PT and PMN-35PT, respectively. The results indicate that the relaxor compositions are much more efficient than the PMN-35PT, especially when a high degree of electric-energy recovery is performed, as a consequence of their low losses.

Based on the presented results we demonstrated that a high degree of electric-energy recovery can importantly improve the energy efficiency of the EC cooling system. However, an EC material with a relaxor nature, i.e., a material with a slim $P-E$ loop such as PMN-100xPT with x$\leq$0.1, should be employed in order to keep the dielectric losses as small as possible and thus achieve a high energy efficiency for the EC cooling system.

Appendix A

Dielectric Breakdown Phenomena

A.1 Dielectric Breakdown Experiment

The dielectric breakdown strength E_b of a selected material is experimentally determined under well-controlled laboratory conditions on a series of samples at a selected temperature. A sample of a known shape is connected to a voltage source and immersed in transformer oil to avoid surface discharge or flashover behavior [5], [50], [132], [133]. The breakdown experiment is carried out by steadily increasing the voltage applied to the sample. A typical current-voltage characteristic of a ceramic material is shown in Figure A.1. When the applied voltage is low, a small current flows through the material. By increasing the voltage, the region of the saturated current is reached, as shown in Figure A.1. In this region a leakage current flows. With a further increase of the voltage to the breakdown voltage V_b an abrupt rise of the current is observed and consequently the breakdown of the material occurs. During the dielectric breakdown the sample discharges, which is sometimes coupled with a spark and an explosive sound [50].

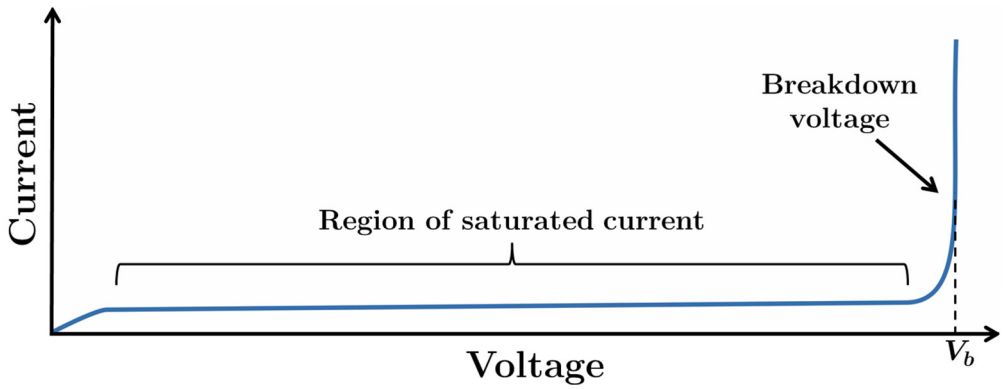


Figure A.1: Typical current-voltage characteristics of dielectric materials. After [50].

Figure A.2 shows the ~50-µm-thick PMN-10PT bulk ceramic sample after breakdown. In Figure A.2 (a) the crater, i.e., the location where the breakdown occurred, can be seen as a black spot. Figure A.2 (b) and (c) show the surface and cross-section of the crater in PMN-10PT material recorded with the FE-SEM. In the literature it is suggested that the crater in a material is caused by the flow of a breakdown current [132], [133]. The formation of conduction channels is believed to be caused by localized melting and a solidification process [50], [133].

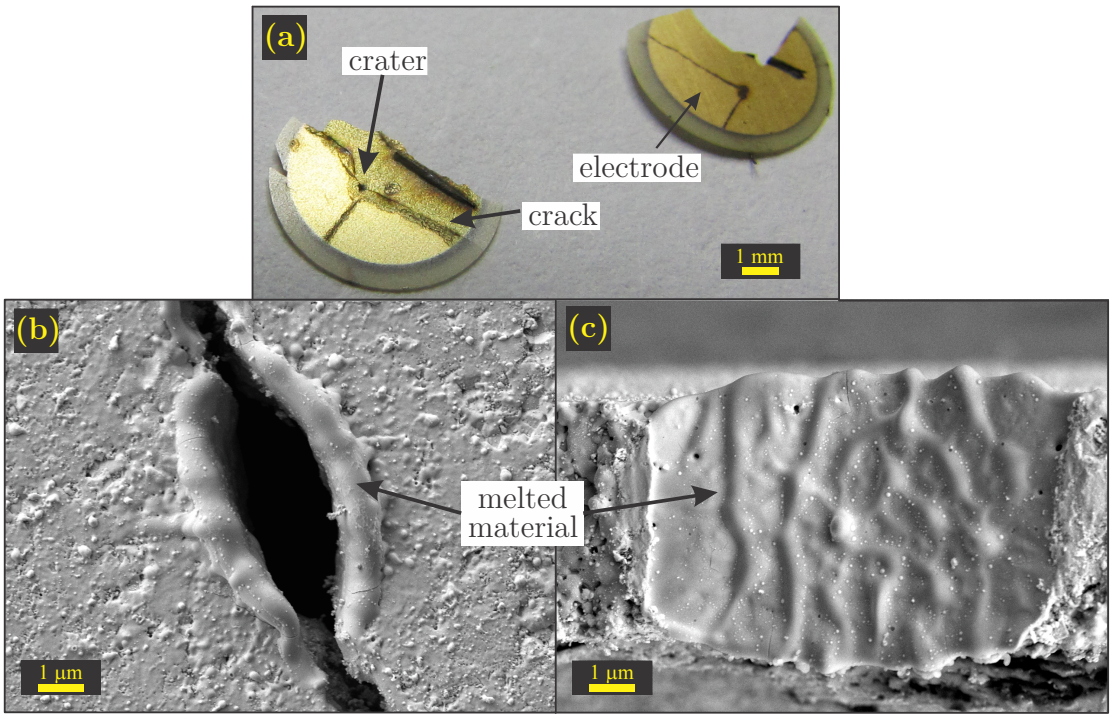


Figure A.2: (a) PMN-10PT ceramic sample partially covered with a Cr/Au electrode after breakdown at 115 kV/cm. (b) Surface and (c) cross-section of the crater in the PMN-10PT material after dielectric breakdown.

A.2 Mechanisms of Dielectric Breakdown Phenomena

A.2.1 Intrinsic Breakdown

The intrinsic breakdown, also known as the electronic breakdown, is characterized by a short breakdown time, around 10^{-7}–10^{-8} s [134] and a dielectric breakdown strength between 10^{6} V/cm and 10^{7} V/cm [46], [135]. The intrinsic breakdown strength depends only on temperature and not on the specimen size and electrode material.

The intrinsic breakdown of a material can be explained as follows. A strong enough electric field can accelerate the electrons in the conductive band to such a level that they have a high enough kinetic energy to generate new electrons by interactions with other atoms in solids. The newly generated electrons can again generate new electrons, which may result in an avalanche of electrons concentrated over a narrow area, causing a breakdown [46], [135].

The process is temperature dependent. At low temperatures, between the lowest reported measurement temperature of -150 °C and room temperature, the intrinsic breakdown strength of crystalline materials increases with increasing temperature, corresponding to an increase of the lattice vibrations and a resulting increase in electron scattering by the lattice. A higher field strength is required to accelerate the electrons to a point at which an electron avalanche is initiated. As the temperature increases, the intrinsic breakdown strength passes through a maximum at approximately room temperature, but decreases again above room temperature, where the thermal breakdown is the predominating mechanism [46], [135].

A.2.2 Thermal Breakdown

The breakdown process can be described by the thermal properties of dielectrics and is the most common failure mode in ceramic insulators [46], [136]. Failures are generally attributed to the local heating, due to a high electric field, and the resulting local conductivity. The increased conductivity causes channeling of the current and a dielectric breakdown of the material [135]. In addition the thermal gradients can cause cracks, which develop around the local hot spot, which can lead to the discharge breakdown as explained in the next subsection. The thermal dielectric strength is typically two orders of magnitude lower than the intrinsic dielectric strength [46]. The power generated in the sample by an ac current is given by [46]:

$$w_{ac} = \nu V^2 C tan\delta, \tag{A.1}$$

where ν is the frequency of the applied electric signal, V is the voltage amplitude and C is the capacitance of the dielectric material. The heat dissipated from the material is given by [46]:

$$q = A\alpha(T_{sur} - T_{ambient}), \tag{A.2}$$

where q is the heat flow from the sample to the ambient, A is the surface area of the sample, α is the heat-transfer coefficient, T_{sur} is the surface temperature and $T_{ambient}$ is the ambient temperature. To avoid the heat accumulation and thermal breakdown, the dissipated heat must be equal to the heat generated in the material [46].

The heat generated in the sample depends on ν and V as well as on the material parameters ε' and $tan\delta$, while the dissipated heat depends on the shape and temperature of the sample and the ambient temperature as well as on the material parameter α.

A.2.3 Discharge Breakdown

The discharge breakdown, also known as the ionization breakdown, occurs in inhomogeneous ceramics, mainly through the mechanism of partial gas discharges, resulting from the presence of pores or cracks in the ceramic [46]. It has been suggested that the failure might be a direct consequence of the heat generation by the discharge of gases within the pore [132]. Consequently, the discharge can lead to local heating, ionization and consequently to the generation of a cascade of charges, which transmit heat to the surrounding material. The resulting temperature gradients and the development of the thermal stress lead to high dielectric losses and a locally high conduction [46]. Estimates of the rise in temperature in the material immediately adjacent to a discharging pore range from a few degrees Celsius for a low-permittivity ceramic (like alumina) to about 1000 °C for high-permittivity ferroelectric ceramics (such as PMN-PT) [136]. Furthermore, the stresses can generate cracks, leading to further ionization and breakdown, similar as that described for the thermal breakdown.

A.3 Factors Affecting Dielectric Breakdown Strength

A.3.1 Influence of the Microstructure on the Dielectric Breakdown Strength

The sintering temperature and time markedly influence the grain size and porosity of the material and consequently also affect the dielectric breakdown strength.

A.3.1.1 Influence of the Grain Size on the Dielectric Breakdown Strength

Experimental data [46], [49]–[53] for ceramics with grain sizes from 0.5 µm to 41 µm show that the smaller the average grain size of a material the higher the E_b. This relationship can be explained by the fact that more grain boundaries represent a longer path of least resistance for the tunneling current, which requires a higher voltage for the dielectric breakdown to occur [54]. In Figure A.3 the average grain size GS vs. E_b in $BaTiO_3$ ceramics is shown. The data can be fitted using the relation:

$$E_b \propto GS^{-a}, \tag{A.3}$$

Where a is the fitting parameter, determined from the slope, and is in this case approximately 0.5.

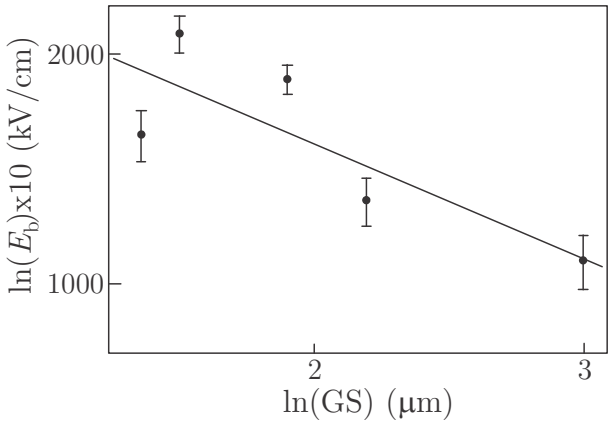


Figure A.3: Average grain size (GS) vs. dielectric breakdown strength E_b for $BaTiO_3$ ceramics. After [52].

A.3.1.2 Influence of the Porosity on the Dielectric Breakdown Strength

The discharge breakdown mechanism is strongly related to porosity, as described in the previous section. The entrapped gases inside the pores can lead to ionization at high fields, particularly under high-humidity conditions. This in turn can lead to a high current flow, local heating, cracking and thermal breakdown [46]. The effect of porosity on the dielectric breakdown strength for PZT [23] was studied by Gerson et al. [55]. They prepared PZT ceramics with controlled porosity by incorporating small polymer spheres in the ceramic powder. The polymer spheres were decomposed in a "burnout" process at 500°C, and did not affect the densification of the surrounding ceramic, which occurred at temperatures above 1200°C. The effect of the amount of pores on E_b is shown in Figure A.4 (a). It can be seen that with increasing porosity content, the E_b markedly decreases.

The effect of the porosity on E_b calculated for different pore sizes is shown in Figure A.4 (b). It can be seen that the slopes of the theoretical curves vary appreciably with the diameter of the pores. By increasing the pore content, the E_b decreases less for the ceramics with smaller pores in comparison to the ceramics with larger ones [55]. Therefore, in PZT ceramics the amount and size of the pores should be minimized to increase its dielectric breakdown strength.

[23] Composition of PZT was not given.

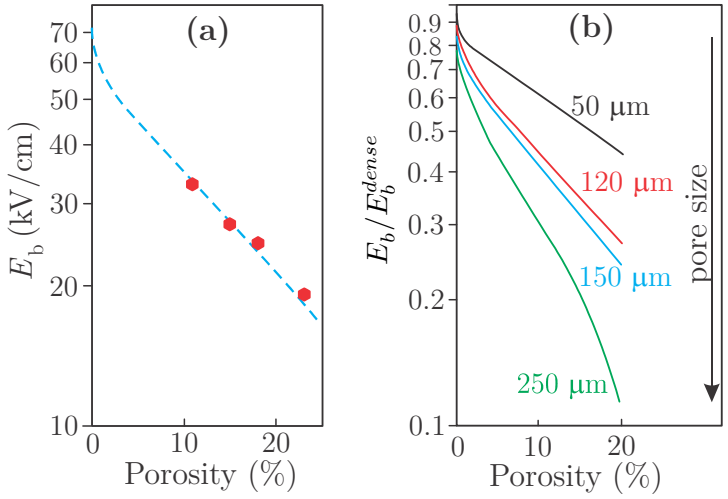


Figure A.4: (a) The effect of the amount of pores on E_b for PZT ceramics. Cross marks represent experimental data, while the dashed curve is a theoretical prediction for the material that contains 120-µm pores. (b) The effect of the amount of pores on E_b calculated for different pore sizes, where $E_b^{dense}$is the dielectric breakdown strength of the completely dense ceramics. After [55].

A.3.1.3 Influence of the Sample Geometry on the Dielectric Breakdown Strength

With increasing bulk ceramic sample thickness, the breakdown voltage V_b increases; however, at the same time its dielectric breakdown strength E_b decreases [5], [55], see Figure A.5 (a). Namely, for thinner samples, the probability of the occurrence of a critical defect at a given stress is lower than in thicker samples [55], [136].

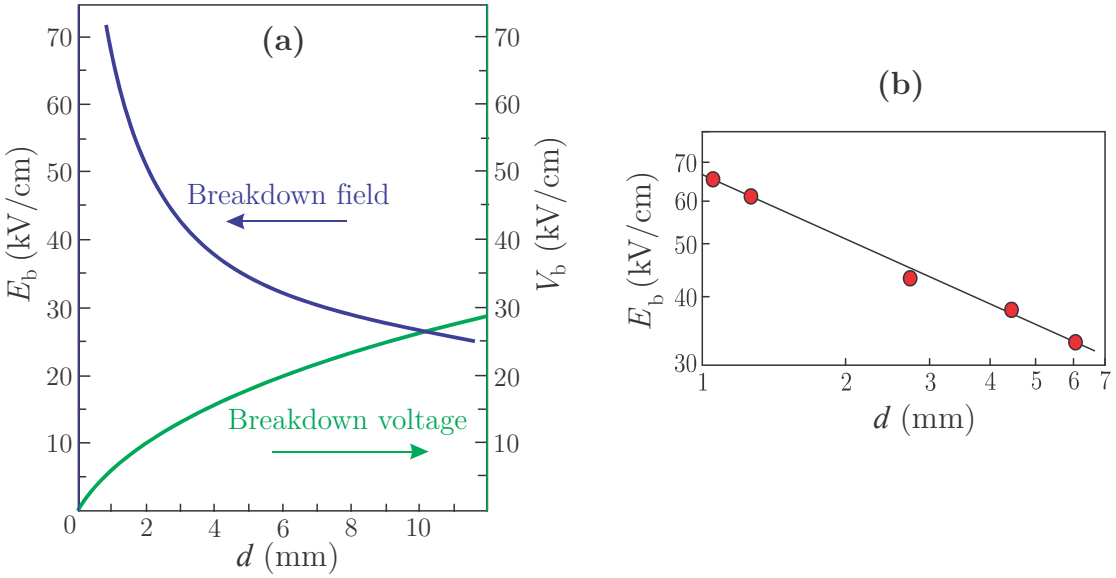


Figure A.5: (a) Dielectric breakdown strength E_b and breakdown voltage V_b vs. thickness d for PZT ceramics. After [5]. (b) Dielectric breakdown strength E_b vs. thickness d for PZT ceramics. Note the logarithmic scales. Cross marks represent experimental data, while the black line represents the best fit of the experimental data. After [55].

In Figure A.5 (b) a log-log plot of the dielectric breakdown strength vs. thickness for a PZT bulk material with 95 % of theoretical density and pores of about 5–10 µm is shown. The data can be fitted by the relation [55]:

$$E_b \propto d^{-a}, \tag{A.4}$$

where d is the sample thickness and a is the fitting parameter. The data in Figure A.5 are only given for the thickness range from mm to cm. The question is, whether the relation is valid also for thinner samples.

The E_b does not depend only on the thickness, but also on the shape of a bulk ceramic specimen. In Figure A.6 two geometries of the sample are shown [132]. In the first case (Figure A.6 a) the electrodes do not cover the whole surface of the sample and consequently a higher electric field at the step edges of the electrode can cause a premature breakdown, when a high voltage is applied [137]. In the second case (Figure A.6 b) the shape of the sample is designed in such a way that it is possible to control the breakdown area in the material. Here, the breakdown failure occurs in the center of the electrode, where the sample is the thinnest and the electric field is the highest. With such an electrode configuration the influence of the boundary conditions is diminished.

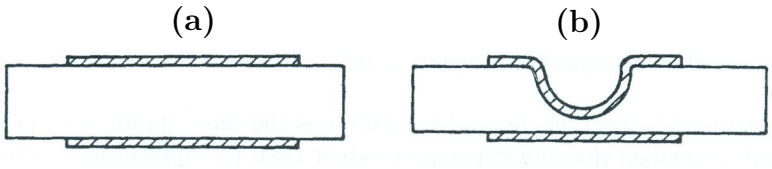


Figure A.6: Cross-sections of disk specimens for measurements of the dielectric strength; (a) standard flat disc with electrodes and (b) electrode on a recessed sample. After [136].

A.3.1.4 Influence of the Working Temperature on the Dielectric Breakdown Strength

Higher operating temperatures decrease the dielectric breakdown strength E_b due to the higher conduction in the materials, as explained in the section on the thermal breakdown mechanism [46], [53]. This is shown in Figure A.7 for $BaTiO_3$ ceramics [53].

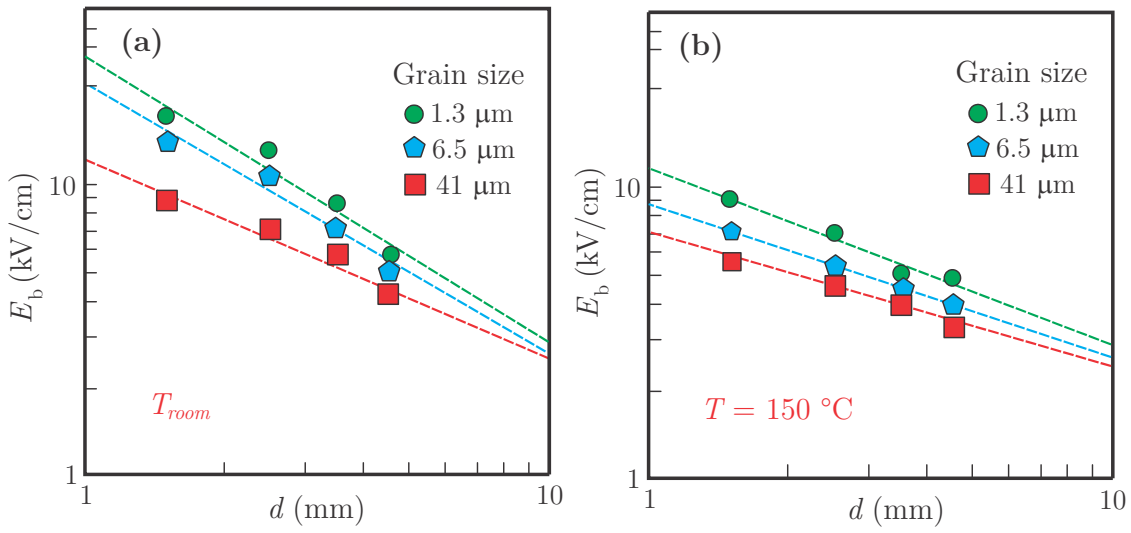


Figure A.7: Thickness dependence of the dielectric breakdown strength for $BaTiO_3$ ceramics at (a) T_{room} and (b) 150 °C. After [53].

In this work the influences of the grain size and thickness of $BaTiO_3$ samples were also studied. As can be seen in Figure A.7, the smaller the average grain size the higher the dielectric strength at a given temperature is [46], [49], [50], [53]. Such a dependence was already shown in Figure A.5. Moreover, the thickness dependence of E_b is in accordance with the results obtained for PZT ceramics (see Figure A.5), i.e., the E_b decreases with increasing sample thickness.

Appendix B

Specific Heat Capacity of the PMN-100xPT Ceramics

The PMN-100xPT ceramics with x = 0, 0.1 and 0.35 were prepared from mechanochemically synthesized powders and sintered at 1200 °C for 2 h. The details of the sample preparation for the PMN-10PT can be found in Section 3.1.1.1, and for the PMN and PMN-35PT in [138], respectively. The specific heat capacity c_E for the selected composition was calculated from the DSC curves as described in Section 3.2.6.

The c_E as a function of temperature for selected PMN-PT compositions is presented in Figure B.1. At 35 °C the c_E is between 0.323 J/g°C and 0.326 J/g°C for all the samples. The specific heat capacity of PMN and PMN-10PT increases continuously with temperature. In PMN such a slow increase of c_E is observed to be approximately 220 °C, while above this temperature it is almost constant. In PMN-10PT, the plateau is reached at a lower temperature, i.e., at ~120 °C. In PMN-35PT the behavior is different, i.e., a clear anomaly in c_E is observed at ~153 °C, which is related to the phase transition of the tetragonal phase to the high temperature cubic phase. This is in a good agreement with the dielectric anomaly of this material (~160 °C at 10 kHz; cf. Figure 1.10). No anomalies in c_E have been detected in PMN and PMN-10PT ceramics within our temperature range. For these ceramics the dielectric permittivity anomalies occur at ~-15 C and ~40°C at 10 kHz, cf. Figure 1.10, which is below or close to the lower limit of our measurement range [138].

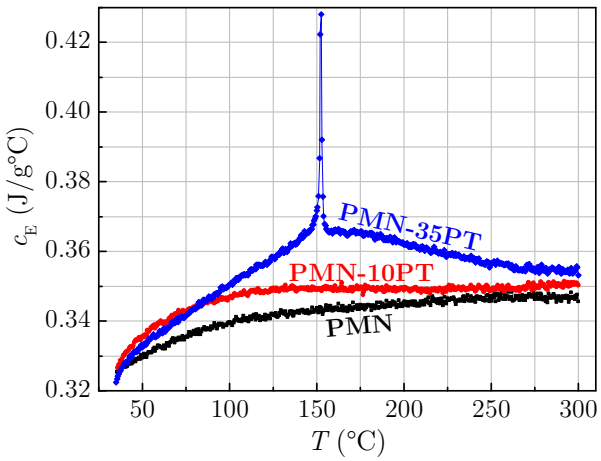


Figure B.1: Temperature dependence of the specific heat capacity c_E of the PMN-100xPT (x = 0, 0.1 and 0.35) ceramics. After [138].

References

[1] R. Waser, U. Böttger, and S. Tiedke, Eds., *Polar oxides*, 1st ed. Weinheim, Germany: Wiley-VCH Verlag GmbH & Co. KGaA, 2004.

[2] D. Damjanovic, "Ferroelectric, dielectric and piezoelectric properties of ferroelectric thin films and ceramics," *Reports on Progress in Physics*, vol. 61, no. 9, pp. 1267–1324, 1998.

[3] J. D. Jackson, *Classical Electrodynamics*, 3rd ed. New Jersey, USA: John Wiley & Sons, Inc., 1999.

[4] J. W. McPherson and H. C. Mogul, "Underlying physics of the thermochemical E model in describing low-field time-dependent dielectric breakdown in SiO_2 thin films," *Journal of Applied Physics*, vol. 84, no. 3, pp. 1513–1532, 1998.

[5] B. Jaffe, W. R. Cook, and H. L. Jaffe, *Piezoelectric ceramics*, 1st ed. London, United Kingdom: Academic Press Inc., 1971.

[6] J. Shieh, J. H. Yeh, Y. C. Shu, and J. H. Yen, "Hysteresis behaviors of barium titanate single crystals based on the operation of multiple 90° switching systems," *Materials Science and Engineering: B*, vol. 161, no. 1–3, pp. 50–54, 2009.

[7] K. Kinoshita, "Grain-size effects on dielectric properties in barium titanate ceramics," *Journal of Applied Physics*, vol. 47, no. 1, pp. 371–373, 1976.

[8] Z.-G. Ye, Y. Bing, J. Gao, A. A. Bokov, P. Stephens, B. Noheda, and G. Shirane, "Development of ferroelectric order in relaxor (1-x)$Pb(Mg_{1/3}Nb_{2/3})O_3$-x$PbTiO_3$," *Physical Review B*, vol. 67, no. 10, pp. 104104–1–8, 2003.

[9] L. E. Cross, "Relaxor ferroelectrics," *Ferroelectrics*, vol. 76, no. 1, pp. 241–267, 1987.

[10] R. A. Cowley, S. N. Gvasaliya, S. G. Lushnikov, B. Roessli, and G. M. Rotaru, "Relaxing with relaxors: a review of relaxor ferroelectrics," *Advances in Physics*, vol. 60, no. 2, pp. 229–327, 2011.

[11] A. A. Bokov and Z.-G. Ye, "Recent progress in relaxor ferroelectrics with perovskite structure," *Journal of Materials Science*, vol. 41, no. 1, pp. 31–52, 2006.

[12] C. G. F. Stenger and A. J. Burggraaf, "Order–disorder reactions in the ferroelectric perovskites $Pb(Sc_{1/2}Nb_{1/2})O_3$ and $Pb(Sc_{1/2}Ta_{1/2})O_3$," *Physica Status Solidi A*, vol. 61, no. 1, pp. 275–285, 1980.

[13] C. Malibert, B. Dkhil, J. M. Kiat, D. Durand, J. J. Berar, and A. Spasojevic-de Bire, "Order and disorder in the relaxor ferroelectric perovskite $PbSc_{1/2}Nb_{1/2}O_3$ (PSN): comparison with simple perovskite $BaTiO_3$ and $PbTiO_3$," *Journal of Physics: Condensed Matter*, vol. 9, pp. 7485–7500, 1997.

[14] M. Zhu, C. Chen, J. Tang, Y. Hou, H. Wang, H. Yan, W. Zhang, J. Chen, and W.

Zhang, "Effects of ordering degree on the dielectric and ferroelectric behaviors of relaxor ferroelectric $Pb(Sc_{1/2}Nb_{1/2})O_3$ ceramics," *Journal of Applied Physics*, vol. 103, no. 8, pp. 084124–1–6, 2008.

[15] C. Boulesteix, F. Varnier, A. Llebaria, and E. Husson, "Numerical determination of the local ordering of $PbMg_{1/3}Nb_{2/3}O_3$ (PMN) from high resolution electron microscopy images," *Journal of Solid State Chemistry*, vol. 108, no. 1, pp. 141–147, 1994.

[16] P. K. Davies and M. A. Akbas, "Chemical order in PMN-related relaxors: structure, stability, modification, and impact on properties," *Journal of Physics and Chemistry of Solids*, vol. 61, no. 2, pp. 159–166, 2000.

[17] G. Burns and B. A. Scott, "Index of refraction in 'dirty' displacive ferroelectrics," *Solid State Communications*, vol. 13, no. 3, pp. 423–426, 1973.

[18] V. Bovtun, J. Petzelt, V. Porokhonskyy, S. Kamba, and Y. Yakimenko, "Structure of the dielectric spectrum of relaxor ferroelectrics," *Journal of the European Ceramic Society*, vol. 21, no. 10–11, pp. 1307–1311, 2001.

[19] S. A. Gridnev, A. A. Glazunov, and A. N. Tsotsorin, "Temperature evolution of the local order parameter in relaxor ferroelectrics (1-x)PMN-xPZT," *Physica Status Solidi A*, vol. 202, no. 11, pp. R122–R124, 2005.

[20] V. Bobnar, C. Filipič, A. Levstik, and Z. Kutnjak, "High-temperature dielectric response of (1-x)$Pb(Mg_{1/3}Nb_{2/3})O_3$-x$PbTiO_3$: Does Burns temperature exist in ferroelectric relaxors?," *Journal of Applied Physics*, vol. 107, no. 8, pp. 084104–1–4, 2010.

[21] R. Pirc and R. Blinc, "Spherical random-bond-random-field model of relaxor ferroelectrics," *Physical Review B*, vol. 60, no. 19, pp. 13470–13478, 1999.

[22] Archive of the Electronic Ceramics department - K5, Jožef Stefan Institute, Ljubljana, Slovenia.

[23] A. Levstik, Z. Kutnjak, C. Filipič, and R. Pirc, "Glassy freezing in relaxor ferroelectric lead magnesium niobate," *Physical Review B*, vol. 57, no. 18, pp. 204–211, 1998.

[24] H. Arndt, F. Sauerbier, G. Schmidt, and L. A. Shebanov, "Field-induced phase transition in $Pb(Mg_{1/3}Nb_{2/3})O_3$ single crystals," *Ferroelectrics*, vol. 79, no. 1, pp. 145–148, 1988.

[25] R. Sommer, N. K. Yushin, and J. J. van der Klink, "Polar metastability and an electric-field-induced phase transition in the disordered perovskite $Pb(Mg_{1/3}Nb_{2/3})O_3$," *Physical Review B*, vol. 48, no. 18, pp. 13230–13237, 1993.

[26] O. Bidault, M. Licheron, E. Husson, and A. Morell, "The onset of an electric field-induced ferroelectric-like phase in the perovskite," *Journal of Physics: Condensed Matter*, vol. 8, no. 42, pp. 8017–8026, 1996.

[27] Z. Kutnjak, B. Vodopivec, and R. Blinc, "Anisotropy of electric field freezing of the relaxor ferroelectric $Pb(Mg_{1/3}Nb_{2/3})O_3$," *Physical Review B*, vol. 77, no. 5, pp. 054102–1–5, 2008.

[28] Z. Kutnjak and R. Blinc, "Electric field induced critical points and polarization

rotations in relaxor ferroelectrics," *Physical Review B*, vol. 76, no. 10, pp. 104102–1–8, 2007.

[29] F. Jona and G. Shirane, *Ferroelectric crystals*, 1st ed. Frankfurt, Germany: Pergamon Press Inc., 1962.

[30] M. E. Lines and A. M. Glass, *Principles and applications of ferroelectrics and related materials*, 1st ed. Oxford, United Kingdom: Oxford University Press, 1977.

[31] J. F. Scott, "Electrocaloric materials," *Annual Review of Materials Research*, vol. 41, no. 1, pp. 229–240, 2011.

[32] M. Valant, "Electrocaloric materials for future solid-state refrigeration technologies," *Progress in Materials Science*, vol. 57, no. 6, pp. 980–1009, 2012.

[33] X. Moya, S. Kar-Narayan, and N. D. Mathur, "Caloric materials near ferroic phase transitions," *Nature Materials*, vol. 13, no. 5, pp. 439–450, 2014.

[34] T. Correia and Q. Zhang, Eds., *Electrocaloric materials: New generation of coolers*, 1st ed. Berlin, Heidelberg, Germany: Springer-Verlag Berlin Heidelberg, 2014.

[35] Z. Kutnjak, B. Rožič, and R. Pirc, "Electrocaloric effect: theory, measurements, and applications," in *Wiley Encyclopedia of Electrical and Electronics Engineering*, New Jersey, USA: John Wiley & Sons, 2015.

[36] X. Moya, E. Defay, V. Heine, and N. D. Mathur, "Too cool to work," *Nature Physics*, vol. 11, no. 3, pp. 202–205, 2015.

[37] U. Plaznik, A. Kitanovski, B. Rožič, B. Malič, H. Uršič, S. Drnovšek, J. Cilenšek, M. Vrabelj, A. Poredoš, and Z. Kutnjak, "Bulk relaxor ferroelectric ceramics as a working body for an electrocaloric cooling device," *Applied Physics Letters*, vol. 106, pp. 043903–1–4, 2015.

[38] M. Ožbolt, A. Kitanovski, J. Tušek, and A. Poredoš, "Electrocaloric refrigeration: Thermodynamics, state of the art and future perspectives," *International Journal of Refrigeration*, vol. 40, pp. 174–188, 2014.

[39] H. Gu, B. Craven, X. Qian, X. Li, A. Cheng, and Q. M. Zhang, "Simulation of chip-size electrocaloric refrigerator with high cooling-power density," *Applied Physics Letters*, vol. 102, no. 11, pp. 112901–1–5, 2013.

[40] H. Gu, X.-S. Qian, H.-J. Ye, and Q. M. Zhang, "An electrocaloric refrigerator without external regenerator," *Applied Physics Letters*, vol. 105, no. 16, pp. 162905–1–4, 2014.

[41] D. Guo, J. Gao, Y.-J. Yu, S. Santhanam, A. Slippey, G. K. Fedder, A. J. H. McGaughey, and S.-C. Yao, "Design and modeling of a fluid-based micro-scale electrocaloric refrigeration system," *International Journal of Heat and Mass Transfer*, vol. 72, pp. 559–564, 2014.

[42] R. I. Epstein and K. J. Malloy, "Electrocaloric devices based on thin-film heat switches," *Journal of Applied Physics*, vol. 106, no. 2009, pp. 1–7, 2009.

[43] H. Gu, X. Qian, X. Li, B. Craven, W. Zhu, A. Cheng, S. C. Yao, and Q. M. Zhang, "A chip scale electrocaloric effect based cooling device," *Applied Physics Letters*, vol. 102, no. 12, pp. 122904–1–4, 2013.

[44] Z. Kutnjak and B. Rožič, "Indirect and direct measurements of the electrocaloric

effect," in *Electrocaloric Materials: New Generation of Coolers*, T. Correia and Q. Zhang, Eds. Berlin, Heidelberg, Germany: Springer-Verlag Berlin Heidelberg, 2014, pp. 147–182.

[45] S. G. Lu, B. Rožič, Q. M. Zhang, Z. Kutnjak, R. Pirc, M. Lin, X. Li and L. Gorny, "Comparison of directly and indirectly measured electrocaloric effect in relaxor ferroelectric polymers," *Applied Physics Letters*, vol. 97, no. 20, pp. 202901-1-3, 2010.

[46] C. R. Buchanan, Ed., *Ceramic materials for electronics*, 3rd ed. New York, USA: CRC Press, 2004.

[47] M. Valant, A.-K. Axelsson, F. L. Goupil and N. M. Alford, "Electrocaloric temperature change constrained by the dielectric strength," *Materials Chemistry and Physics*, vol. 136, pp. 277-280, 2012.

[48] J. McPherson, J. Kim, A. Shanware, H. Mogul, and J. Rodriguez, "Proposed universal relationship between dielectric breakdown and dielectric constant," in *Proceedings of the International Electron Devices Meeting IEDM '02, San Francisco, California: IEEE*, 2002, pp. 633–636.

[49] Q. Zhang, J. Zhai, B. Shen, and X. Yao, "Dielectric tunable properties of high dielectric breakdown $Ba_{0.5}Sr_{0.5}TiO_3$-$Zn_2P_2O_7$ composite ceramics," *Ceramics International*, vol. 38, pp. S53–S56, 2012.

[50] I. O. Owate and R. Freer, "ac breakdown characteristics of ceramic materials," *Journal of Applied Physics*, vol. 72, no. 6, pp. 2418–2422, 1992.

[51] M. Touzin, D. Goeuriot, C. Guerret-Piécourt, D. Juvé, and H.-J. Fitting, "Alumina based ceramics for high-voltage insulation," *Journal of the European Ceramic Society*, vol. 30, no. 4, pp. 805–817, 2010.

[52] T. Tunkasiri and G. Rujijanagul, "Dielectric strength of fine grained barium titanate ceramics," *Journal of Materials Science Letters*, vol. 15, no. 20, pp. 1767–1769, 1996.

[53] H. Y. Lee, K. H. Cho, and H.-D. Nam, "Grain size and temperature dependence of electrical breakdown in $BaTiO_3$ ceramic," *Ferroelectrics*, vol. 334, no. 1, pp. 165–169, 2006.

[54] X. Xu and G. E. Hilmas, "Effects of $Ba_6Ti_{17}O_{40}$ on the dielectric properties of Nb-doped $BaTiO_3$ ceramics," *Journal of the American Ceramic Society*, vol. 89, no. 20850, pp. 2496–2501, 2006.

[55] R. Gerson and T. C. Marshall, "Dielectric breakdown of porous ceramics," *Journal of Applied Physics*, vol. 30, no. 11, pp. 1650–1653, 1959.

[56] R. D. Lide, Ed., *CRC Handbook of chemistry and physics*, 86th ed. New York, USA: CRC Press, Taylor & Francis Group, 2005.

[57] A. S. Mischenko, Q. Zhang, J. F. Scott, R. W. Whatmore, and N. D. Mathur, "Giant electrocaloric effect in thin-film $PbZr_{0.95}Ti_{0.05}O_3$," *Science*, vol. 311, no. 5765, pp. 1270–1271, 2006.

[58] E. Defay, S. Crossley, S. Kar-Narayan, X. Moya, and N. D. Mathur, "The electrocaloric efficiency of ceramic and polymer films," *Advanced Materials*, vol. 25, pp. 3337–3342, 2013.

[59] P. Atkins and J. de Paula, *Atkins' physical chemistry*, 8th ed. Oxford, United Kingdom: Oxford University Press, 2010.

[60] H. Ouchi, K. Nagano, and S. Hayakawa, "Piezoelectric properties of $Pb(Mg_{1/3}Nb_{2/3})O_3$-$PbTiO_3$-$PbZrO_3$ solid solution ceramics," *Journal of the American Ceramic Society*, vol. 48, no. 12, pp. 630–635, 1965.

[61] S. W. Choi, R. T. R. Shrout, S. J. Jang, and A. S. Bhalla, "Dielectric and pyroelectric properties in the $Pb(Mg_{1/3}Nb_{2/3})O_3$-$PbTiO_3$ system," *Ferroelectrics*, vol. 100, no. 1, pp. 29–38, 1989.

[62] J. Kelly, M. Leonard, C. Tantigate, and A. Safari, "Effect of composition on the electromechanical properties of (1-x)$Pb(Mg_{1/3}Nb_{2/3})O_3$-x$PbTiO_3$ ceramics," *Journal of the American Ceramic Society*, vol. 80, no. 4, pp. 957–964, 1997.

[63] O. Noblanc, P. Gaucher, and G. Calvarin, "Structural and dielectric studies of $Pb(Mg_{1/3}Nb_{2/3})O_3$–$PbTiO_3$ ferroelectric solid solutions around the morphotropic boundary," *Journal of Applied Physics*, vol. 79, no. 8, pp. 4291–4297, 1996.

[64] W. Cao and L. E. Cross, "Distribution functions of coexisting phases in a complete solid solution system," *Journal of Applied Physics*, vol. 73, no. 7, pp. 3250–3255, 1993.

[65] B. Noheda, D. E. Cox, G. Shirane, J. Gao, and Z.-G. Ye, "Phase diagram of the ferroelectric relaxor (1-x)$PbMg_{1/3}Nb_{2/3}O_3$-x$PbTiO_3$," *Physical Review B*, vol. 66, no. 5, pp. 054104–1–10, 2002.

[66] J.-M. Kiat, Y. Uesu, B. Dkhil, M. Matsuda, C. Malibert, and G. Calvarin, "Monoclinic structure of unpoled morphotropic high piezoelectric PMN-PT and PZN-PT compounds," *Physical Review B*, vol. 65, pp. 064106–1, 2002.

[67] R. Jiménez, B. Jiménez, J. Carreaud, J. M. Kiat, B. Dkhil, J. Holc, M. Kosec, and M. Algueró, "Transition between the ferroelectric and relaxor states in 0.8$Pb(Mg_{1/3}Nb_{2/3})O_3$-0.2$PbTiO_3$ ceramics," *Physical Review B*, vol. 74, no. 18, pp. 184106–1–8, 2006.

[68] J.-M. Kiat and B. Dkhil, "From the structure of relaxors to the structure of MPB systems," in *Handbook of Advanced Dielectric, Piezoelectric and Ferroelectric Materials*, 1st ed., Z.-G. Ye, Ed. New York, USA: Elsevier, 2008, pp. 391–446.

[69] M. Algueró, J. Ricote, P. Ramos, R. Jiménez, J. Carreaud, J.-M. Kiat, B. Dkhil, J. Holc, and M. Kosec, "Size effects on the macroscopic properties of the relaxor ferroelectric $Pb(Mg_{1/3}Nb_{2/3})O_3$-$PbTiO_3$," in *Handbook of Advanced Dielectric, Piezoelectric and Ferroelectric Materials*, 1st ed., Z.-G. Ye, Ed. New York, USA: Elsevier, 2008, pp. 447–471.

[70] P. Papet, J. P. Dougherty, and T. R. Shrout, "Particle and grain size effects on the dielectric behavior of the relaxor ferroelectric $Pb(Mg_{1/3}Nb_{2/3})O_3$," *Journal of Materials Research*, vol. 5, no. 12, pp. 2902–2909, 1990.

[71] C. A. Randall, A. D. Hilton, D. J. Barber, and T. R. Shrout, "Extrinsic contributions to the grain size dependence of relaxor ferroelectric $Pb(Mg_{1/3}Nb_{2/3})O_3$: $PbTiO_3$ ceramics," *Journal of Materials Research*, vol. 8, no. 04, pp. 880–884, 1993.

[72] E. R. Leite, A. M. Scotch, A. Khan, T. Li, H. M. Chan, M. P. Harmer, S.-F. Liu,

and S.-E. Park, "Chemical heterogeneity in PMN-35PT ceramics and effects on dielectric and piezoelectric properties," *Journal of the American Ceramic Society*, vol. 85, no. 12, pp. 3018–3024, 2002.

[73] J. Carreaud, P. Gemeiner, J. M. Kiat, B. Dkhil, C. Bogicevic, T. Rojac, and B. Malič, "Size-driven relaxation and polar states in $PbMg_{1/3}Nb_{2/3}O_3$-based system," *Physical Review B*, vol. 72, no. 17, pp. 174115–1–6, 2005.

[74] M. Algueró, J. Ricote, R. Jiménez, P. Ramos, J. Carreaud, B. Dkhil, J. M. Kiat, J. Holc, and M. Kosec, "Size effect in morphotropic phase boundary $Pb(Mg_{1/3}Nb_{2/3})O_3$-$PbTiO_3$," *Applied Physics Letters*, vol. 91, no. 11, pp. 112905–1–3, 2007.

[75] T. R. Shrout and S. L. Swartz, "Dielectric properties of pyrochlore lead magnesium niobate," *Materials Research Bulletin*, vol. 18, no. 6, pp. 663–667, 1983.

[76] M. Inada, "Analysis of the formation process of the piezoelectric PCM ceramics," *Japanese National Technical Reports*, vol. 27, no. 1, pp. 95–102, 1977.

[77] S. L. Swartz and T. R. Shrout, "Fabrication of perovskite lead magnesium niobate," *Materials Research Bulletin*, vol. 17, no. 10, pp. 1245–1250, 1982.

[78] S. L. Swartz, T. R. Shrout, W. A. Schulze, and L. E. Cross, "Dielectric properties of lead-magnesium niobate ceramics," *Journal of the American Ceramic Society*, vol. 67, no. 5, pp. 311–314, 1984.

[79] L. Lü and M. O. Lai, *Mechanical Alloying*, 1st ed., vol. 30. Norwell, USA: Kluwer Academic Publishers, 1997.

[80] T. Rojac and M. Kosec, "Mechanochemical synthesis of complex ceramic oxides," in *High-Energy Ball Milling*, 1st ed., M. Sopicka-Lizer, Ed. Padstow, United Kingdom: Elsevier, 2010, pp. 113–148.

[81] J. Baek, T. Isobe, and M. Senna, "Synthesis of pyrochlore-free $0.9Pb(Mg_{1/3}Nb_{2/3})O_3$-$0.1PbTiO_3$ ceramics via a soft mechanochemical route," *Journal of the American Ceramic Society*, vol. 81, no. 192422, pp. 973–981, 1997.

[82] J. Wang, D. M. Wan, J. M. Xue, and W. B. Ng, "Mechanochemical synthesis of $0.9Pb(Mg_{1/3}Nb_{2/3})O_3$-$0.1PbTiO_3$ from mixes oxides," *Advanced Materials*, vol. 11, no. 3, pp. 210–213, 1999.

[83] J. Wang, J. M. Xue, D. M. Wan, and B. K. Gan, "Mechanically activating nucleation and growth of complex perovskites," *Journal of Solid State Chemistry*, vol. 154, no. 2, pp. 321–328, 2000.

[84] D. Kuščer, J. Holc, M. Kosec, and A. Meden, "Mechano-synthesis of lead-magnesium-niobate ceramics," *Journal of the American Ceramic Society*, vol. 89, no. 10, pp. 3081–3088, 2006.

[85] D. Kuščer, J. Holc, and M. Kosec, "Formation of $0.65Pb(Mg_{1/3}Nb_{2/3})O_3$-$0.35PbTiO_3$ using a high-energy milling process," *Journal of the American Ceramic Society*, vol. 90, no. 1, pp. 29–35, 2007.

[86] L. Shebanovs, K. Borman, W. N. Lawless, and A. Kalvane, "Electrocaloric effect in some perovskite ferroelectric ceramics and multilayer capacitors," *Ferroelectrics*, vol. 273, no. 1, pp. 137–142, 2002.

[87] B. Rozič, B. Malič, H. Ursič, J. Holc, M. Kosec, and Z. Kutnjak, "Direct

measurements of the electrocaloric effect in bulk $PbMg_{1/3}Nb_{2/3}O_3$ (PMN) ceramics," *Ferroelectrics*, vol. 421, no. September 2013, pp. 103–107, 2011.

[88] B. Rožič, M. Kosec, H. Uršič, J. Holc, B. Malič, Q. M. Zhang, R. Blinc, R. Pirc, and Z. Kutnjak, "Influence of the critical point on the electrocaloric response of relaxor ferroelectrics," *Journal of Applied Physics*, vol. 110, no. 6, pp. 064118–1–5, 2011.

[89] J. Peräntie, H. N. Tailor, J. Hagberg, H. Jantunen, and Z.-G. Ye, "Electrocaloric properties in relaxor ferroelectric (1-x)$Pb(Mg_{1/3}Nb_{2/3})O_3$-x$PbTiO_3$ system," *Journal of Applied Physics*, vol. 114, no. 17, pp. 174105–1–6, 2013.

[90] L. Luo, H. Chen, Y. Zhu, W. Li, H. Luo, and Y. Zhang, "Pyroelectric and electrocaloric effect of $\langle 111 \rangle$ -oriented 0.9PMN–0.1PT single crystal," *Journal of Alloys and Compounds*, vol. 509, no. 32, pp. 8149–8152, 2011.

[91] B. Rozič, H. Uršič, J. Holc, M. Kosec, and Z. Kutnjak, "Direct measurements of the electrocaloric effect in substrate-free PMN-0.35PT thick films on a platinum layer," *Integrated Ferroelectrics*, vol. 140, no. 1, pp. 161–165, 2012.

[92] B. Rožič, H. Ursič, M. Vrabelj, J. Holc, B. Malič, and Z. Kutnjak, "Electrocaloric response in substrate-free PMN-0.30PT thick films," *Ferroelectrics*, vol. 465, no. 1, pp. 1–6, 2014.

[93] C. Molin, M. Sanlialp, V. V Shvartsman, D. C. Lupascu, P. Neumeister, A. Schoenecker, and S. Gebhardt, "Effect of dopants on the electrocaloric effect of 0.92$Pb(Mg_{1/3}Nb_{2/3})O_3$-0.08$PbTiO_3$ ceramics," *Journal of the European Ceramic Society*, vol. 35, no. 7, pp. 2065–2071, 2015.

[94] J. Hagberg, A. Uusimäki, and H. Jantunen, "Electrocaloric characteristics in reactive sintered 0.78$Pb(Mg_{1/3}Nb_{2/3})O_3$-0.13$PbTiO_3$," *Applied Physics Letters*, vol. 92, no. 13, pp. 132909–1–3, 2008.

[95] G. Sebald, L. Seveyrat, D. Guyomar, L. Lebrun, B. Guiffard, and S. Pruvost, "Electrocaloric and pyroelectric properties of 0.75$Pb(Mg_{1/3}Nb_{2/3})O_3$-0.25$PbTiO_3$ single crystals," *Journal of Applied Physics*, vol. 100, no. 12, pp. 124112–1–6, 2006.

[96] J. Peräntie, J. Hagberg, A. Uusimäki, and H. Jantunen, "Electric-field-induced dielectric and temperature changes in a <011>-oriented $Pb(Mg_{1/3}Nb_{2/3})O_3$-$PbTiO_3$ single crystal," *Physical Review B*, vol. 82, no. 13, pp. 134119–1–8, 2010.

[97] U. Plaznik, M. Vrabelj, Z. Kutnjak, B. Malič, A. Poredoš, and A. Kitanovski, "Electrocaloric cooling: The importance of electric-energy recovery and heat regeneration," *Europhysics Letters*, vol. 111, no. 5, pp. 57009–1–6, 2015.

[98] T. M. Correia, J. S. Young, R. W. Whatmore, J. F. Scott, N. D. Mathur, and Q. Zhang, "Investigation of the electrocaloric effect in a $PbMg_{2/3}Nb_{1/3}O_3$-$PbTiO_3$ relaxor thin film," *Applied Physics Letters*, vol. 95, no. 18, pp. 182904–1–3, 2009.

[99] A. S. Mischenko, Q. Zhang, R. W. Whatmore, J. F. Scott, and N. D. Mathur, "Giant electrocaloric effect in the thin film relaxor ferroelectric 0.9$PbMg_{1/3}Nb_{2/3}O_3$-0.1$PbTiO_3$ near room temperature," *Applied Physics Letters*, vol. 89, no. 24, pp. 242912–1–3, 2006.

[100] Z. Feng, D. Shi, R. Zeng, and S. Dou, "Large electrocaloric effect of highly (100)-oriented 0.68$PbMg_{1/3}Nb_{2/3}O_3$-0.32$PbTiO_3$ thin films with a $Pb(Zr_{0.3}Ti_{0.7})O_3/PbO_x$

buffer layer," *Thin Solid Films*, vol. 519, no. 16, pp. 5433–5436, 2011.

[101] Z. Feng, D. Shi, and S. Dou, "Large electrocaloric effect in highly (001)-oriented $0.67PbMg_{1/3}Nb_{2/3}O_3$-$0.33PbTiO_3$ thin films," *Solid State Communications*, vol. 151, no. 2, pp. 123–126, 2011.

[102] D. Saranya, A. R. Chaudhuri, J. Parui, and S. B. Krupanidhi, "Electrocaloric effect of PMN-PT thin films near morphotropic phase boundary," *Bulletin of Materials Science*, vol. 32, no. 3, pp. 259–262, 2009.

[103] D. A. Ditmars, S. Ishihara, S. S. Chang, G. Bernstein, and E. D. West, "Enthalpy and heat-capacity standard reference material: synthetic sapphire (alpha-Al_2O_3) from 10 to 2250 K," *Journal of Research of the National Bureau of Standards*, vol. 87, no. 2, pp. 159–163, 1982.

[104] D. Wilcox, B. Dove, D. McDavid, and D. Greer, "UTHSCSA Image tool for Windows version 3.0." University of Texas Health Science Center, San Antonio, USA, 2002.

[105] W. H. Walton, "Feret's statistical diameter as a measure of particle size," *Nature*, vol. 162, no. 4113, pp. 329–330, 1948.

[106] L. B. Kong, J. Ma, W. Zhu, and O. K. Tan, "Preparation of PMN-PT ceramics via a high-energy ball milling process," *Journal of Alloys and Compounds*, vol. 336, pp. 242–246, 2002.

[107] K. T. Zawilski, M. C. C. Custodio, R. C. DeMattei, S.-G. Lee, R. G. Monteiro, H. Odagawa, and R. S. Feigelson, "Segregation during the vertical Bridgman growth of lead magnesium niobate-lead titanate single crystals," *Journal of Crystal Growth*, vol. 258, no. 3–4, pp. 353–367, 2003.

[108] J.-H. Park, B.-K. Kim, and J. S. Park, "Electrostrictive coefficients of $0.9Pb(Mg_{1/3}Nb_{2/3})O_3$-$0.1PbTiO_3$ relaxor ferroelectric ceramics in the ferroelectricity-dominated temperature range," *Journal of the American Ceramic Society*, vol. 79, no. 2, pp. 430–434, 1996.

[109] M. Algueró, A. Moure, L. Pardo, J. Holc, and M. Kosec, "Processing by mechanosynthesis and properties of piezoelectric $Pb(Mg_{1/3}Nb_{2/3})O_3$–$PbTiO_3$ with different compositions," *Acta Materialia*, vol. 54, no. 2, pp. 501–511, 2006.

[110] Z. Kutnjak, J. Petzelt, and R. Blinc, "The giant electromechanical response in ferroelectric relaxors as a critical phenomenon," *Nature*, vol. 441, no. 7096, pp. 956–959, 2006.

[111] E. V. Colla, N. K. Yushin, and D. Viehland, "Dielectric properties of $(PMN)_{(1-x)}(PT)_x$ single crystals for various electrical and thermal histories," *Journal of Applied Physics*, vol. 83, no. 6, pp. 3298–3304, 1998.

[112] R. Zhang, S. Peng, D. Xiao, Y. Wang, B. Yang, J. Zhu, P. Yu, and W. Zhang, "Preparation and characterization of (1-x)$Pb(Mg_{1/3}Nb_{2/3})O_3$-x$PbTiO_3$ electrocaloric ceramics," *Crystal Research and Technology*, vol. 33, no. 5, pp. 827–832, 1998.

[113] H. Uršič, A. Benčan, G. Dražič, G. Esteves, J. L. Jones, T.-M. Usher, T. Rojac, S. Drnovšek, M. Deluca, J. Jouin, V. Bobnar, G. Trefalt, J. Holc, and B. Malič, "Unusual structural-disorder stability of mechanochemically derived-

$Pb(Sc_{0.5}Nb_{0.5})O_3$," *Journal of Materials Chemistry C*, vol. 3, no. 39, pp. 10309–10315, 2015.

[114] W. Huebner, W. Xue, and P. W. Lu, "Effect of tungsten additions on the field-induced piezoelectric properties of $Pb(Mg_{1/3}Nb_{2/3})O_3$-$PbTiO_3$ ceramics," in *Proceedings of the Tenth IEEE International Symposium on Applications of Ferroelectrics, East Brunswick, New Jersey: IEEE*, 1996, vol. 2, pp. 703–706.

[115] W. Z. Zhu, M. Yan, A. L. Kholkin, P. Q. Mantas, and J. L. Baptista, "Effect of tungsten doping on the dielectric response of PZN-PT-BT ceramics with the morphotropic phase boundary composition," *Journal of the European Ceramic Society*, vol. 22, no. 3, pp. 375–381, 2002.

[116] A. Benčan, B. Malič, S. Drnovšek, J. Tellier, T. Rojac, J. Pavlič, M. Kosec, K. G. Webber, J. Rödel, and D. Damjanovič, "Structure and the electrical properties of $Pb(Zr,Ti)O_3$ - zirconia composites," *Journal of the American Ceramic Society*, vol. 95, no. 2, pp. 651–657, 2012.

[117] D. Damjanovic, "Hysteresis in piezoelectric and ferroelectric materials," in *The Science of Hysteresis*, G. Bertotti and I. D. Mayergoyz, Eds. London, United Kingdom: Academic Press Inc., 2006, pp. 337–465.

[118] K. Carl and K. H. Härdtl, "Electrical after-effects in $Pb(Ti,Zr)O_3$ ceramics," *Ferroelectrics*, vol. 17, no. 1, pp. 473–486, 1977.

[119] F. Chu, N. Setter, and A. K. Tagantsev, "The spontaneous relaxor-ferroelectric transition of $Pb(Sc_{0.5}Ta_{0.5})O_3$," *Journal of Applied Physics*, vol. 74, no. 8, pp. 5129–5134, 1993.

[120] F. Chu, I. M. Reaney, and N. Setter, "Spontaneous (zero-field) relaxor-to-ferroelectric-phase transition in disordered $Pb(Sc_{1/2}Nb_{1/2})O_3$," *Journal of Applied Physics*, vol. 77, no. 4, pp. 1671–1676, 1995.

[121] T. Rojac, M. Kosec, B. Budic, N. Setter, and D. Damjanovic, "Strong ferroelectric domain-wall pinning in $BiFeO_3$ ceramics," *Journal of Applied Physics*, vol. 108, no. 7, pp. 0–8, 2010.

[122] G. Xu, D. Viehland, J. F. Li, P. M. Gehring, and G. Shirane, "Evidence of decoupled lattice distortion and ferroelectric polarization in the relaxor system PMN-xPT," *Physical Review B*, vol. 68, no. 21, pp. 212410–1–4, 2003.

[123] V. V. Shvartsman and A. L. Kholkin, "Evolution of nanodomains in $0.9PbMg_{1/3}Nb_{2/3}O_3$-$0.1PbTiO_3$ single crystals," *Journal of Applied Physics*, vol. 101, no. 6, pp. 064108–1–5, 2007.

[124] B. J. Rodriguez, S. Jesse, A. N. Morozovska, S. V. Svechnikov, D. A. Kiselev, A. L. Kholkin, A. A. Bokov, Z.-G. Ye, and S. V. Kalinin, "Real space mapping of polarization dynamics and hysteresis loop formation in relaxor-ferroelectric $PbMg_{1/3}Nb_{2/3}O_3$–$PbTiO_3$ solid solutions," *Journal of Applied Physics*, vol. 108, no. 4, pp. 042006–1–11, 2010.

[125] J. Park, J. Park, J. Park, B. Kim, and Y. Kim, "Piezoelectric properties in PMN-PT relaxor ferroelectrics with MnO_2 addition," *Journal of the European Ceramic Society*, vol. 21, pp. 1383–1386, 2001.

[126] X. Li, X. Zhao, B. Ren, H. Luo, W. Ge, Z. Jiang, and S. Zhang, "Microstructure and dielectric relaxation of dipolar defects in Mn-doped (1−x)Pb($Mg_{1/3}Nb_{2/3}$)O_3–x$PbTiO_3$ single crystals," *Scripta Materialia*, vol. 69, no. 5, pp. 377–380, 2013.

[127] D. Campolo, M. Sitti, and R. S. Fearing, "Efficient charge recovery method for driving piezoelectric actuators with quasi-square waves," *IEEE Transactions on Ultrasonics, Ferroelectrics, and Frequency Control*, vol. 50, no. 3, pp. 237–244, 2003.

[128] R. Pirc, Z. Kutnjak, R. Blinc, and Q. M. Zhang, "Upper bounds on the electrocaloric effect in polar solids," *Applied Physics Letters*, vol. 98, no. 2, pp. 021909–1–3, 2011.

[129] W. Brey, G. Nellis, and S. Klein, "Thermodynamic modeling of magnetic hysteresis in AMRR cycles," *International Journal of Refrigeration*, vol. 47, pp. 85–97, 2014.

[130] A. Kitanovski, J. Tušek, U. Tomc, U. Plaznik, M. Ožbolt, and A. Poredoš, *Magnetocaloric energy conversion: From theory to applications*, 1st ed. Cham, Switzerland: Springer International Publishing, 2015.

[131] G. Trefalt, B. Malič, J. Holc, H. Uršič, and M. Kosec, "Synthesis of 0.65Pb($Mg_{1/3}Nb_{2/3}$)O_3-0.35$PbTiO_3$ by controlled agglomeration of precursor particles," *Journal of the American Ceramic Society*, vol. 95, no. 6, pp. 1858–1865, 2012.

[132] C. Neusel, H. Jelitto, D. Schmidt, R. Janssen, F. Felten, and G. A. Schneider, "Dielectric breakdown of alumina single crystals," *Journal of the European Ceramic Society*, vol. 32, no. 5, pp. 1053–1057, 2012.

[133] J. Liebault, J. Vallayer, D. Goeuriot, D. Treheux, and F. Thevenot, "How the trapping of charges can explain the dielectric breakdown performance of alumina ceramics," *Journal of the European Ceramic Society*, vol. 21, no. 3, pp. 389–397, 2001.

[134] K. C. Kao, *Dielectric phenomena in solids*, 1st ed. San Diego, USA: Elsevier Academic Press, 2004.

[135] W. D. Kingery, H. K. Bowen, and D. R. Uhlmann, *Introduction to ceramics*, 2nd ed. New York, USA: John Wiley & Sons, 1976.

[136] A. J. Moulson and J. M. Herbert, *Electroceramics: materials, properties, applications*, 2nd ed. Chichester, United Kingdom: John Wiley & Sons, 2003.

[137] S. Gevorgian, *Ferroelectrics in microwave devices, circuits and systems*, 1st ed. London, United Kingdom: Springer Verlag, 2009.

[138] H. Uršič, M. Vrabelj, L. Fulanović, A. Bradeško, S. Drnovšek, and B. Malič, "Specific heat capacity and thermal conductivity of the electrocaloric (1-x)Pb($Mg_{1/3}Nb_{2/3}O_3$-x$PbTiO_3$ ceramics between room temperature and 300 °C," *Informacije MIDEM*, vol. 45, no. 4, pp. 260–265, 2015.

[139] U. Plaznik, "Parametrična analiza delovanja aktivnega elektrokaloričnega regeneratorja," Doktorska disertacija, Laboratorij za hlajenje in daljinsko energetiko, Fakulteta za strojništvo, Univerza v Ljubljani, Ljubljana, 2016.

Bibliography

Scientific Articles Related to the Thesis

U. Plaznik, A. Kitanovski, B. Rožič, B. Malič, H. Uršič, S. Drnovšek, J. Cilenšek, M. Vrabelj, A. Poredoš and Z. Kutnjak, "Bulk relaxor ferroelectric ceramics as a working body for an electrocaloric cooling device," *Applied Physics Letters*, vol. 106, no. 04, p. 043903, 2015.

U. Plaznik, M. Vrabelj, Z. Kutnjak, B. Malič, A. Poredoš and A. Kitanovski, "Electrocaloric cooling: The importance of electric-energy recovery and heat regeneration," *Europhysics Letters*, vol. 111, no. 5, p. 57009, 2015.

H. Uršič, M. Vrabelj, L. Fulanović, Andraž Bradeško, S. Drnovšek and B. Malič, "Specific heat capacity and thermal conductivity of the electrocaloric (1-x)$Pb(Mg_{1/3}Nb_{2/3})O_3$-x$PbTiO_3$ ceramics between the room temperature and 300 °C," *Informacije MIDEM*, vol. 45, no. 4, pp. 260-265, 2015.

M. Vrabelj, H. Uršič. Z. Kutnjak, B. Rožič, S. Drnovšek, A. Benčan, V. Bobnar, L. Fulanović and B. Malič, "Large electrocaloric effect in grain-size-engineered 0.9$Pb(Mg_{1/3}Nb_{2/3})O_3$-$PbTiO_3$," *Journal of the European Ceramic Society*, vol. 36, no. 1, pp. 75-80, 2016.

Other Scientific Articles

B. Rožič, H. Uršič, M. Vrabelj, J. Holc, B. Malič and Z. Kutnjak, "Electrocaloric response in substrate-free PMN-0.30PT thick films," *Ferroelectrics*, vol. 465, no. 1, pp. 1-6, 2014.

B. Bertoncelj, K. Vojisavljević, M. Vrabelj and B. Malič, "Thermal properties of polymer-matrix composites reinforced with E-glass fibers," *Informacije MIDEM*, vol. 45, no. 3, pp. 216-221, 2015.

H. Uršič, L. Fulanović, M. Vrabelj, Z. Kutnjak, B. Rožič, S. Drnovšek and Z. Kutnjak, "Electrocaloric properties of 0.7$Pb(Mg_{1/3}Nb_{2/3})O_3$-0.3$PbTiO_3$ ceramics with different grain sizes," *Advances in Applied Ceramics*, vol. 102, no. 2, pp. 77-80, 2016.

H. Uršič, V. Bobnar, B. Malič, C. Filipič, M. Vrabelj, S. Drnovšek, Y.-H. Jo, M. Wencka and Z. Kutnjak, "Multicaloric material as a link between electrocaloric and magnetocaloric refrigeration," *Scientific Reports*, vol. 6, pp. 26629-1-5, 2016.

Published Scientific Conference Contributions

M. Vrabelj, H. Uršič, B. Rožič, Z. Kutnjak, S. Drnovšek and B. Malič, "Electrocaloric properties of 0.7$Pb(Mg_{1/3}Nb_{2/3})O_3$-0.3$PbTiO_3$ ceramics," in *Proceedings* of the *International Ultrasonic Symposium (IUS), Joint IEEE-International Symposium on the Applications of Ferroelectrics (ISAF) and Piezoresponse Force Microscopy and*

Nanoscale Phenomena in Polar Materials (PFM), Joint International Frequency Control Symposium (IFCS), and European Frequency and Time Forum (EFTF), Prague, Czech Republic: 2013 Joint UFFC, EFTF and PFM Symposium, 2013.

M. Vrabelj, H. Uršič, B. Rožič, Z. Kutnjak, S. Drnovšek and B. Malič, "Electrocaloric properties of $0.7Pb(Mg_{1/3}Nb_{2/3})O_3$-$0.3PbTiO_3$ ceramics prepared from mechanochemically activated powder," in *Proceedings of the 49th International Conference on Microelectronics, Devices and Materials & the Workshop on Digital Electronic Systems*, Kranjska Gora, Slovenia: MIDEM – Society for Microelectronics, Electronic Components and Materials, 2013.

M. Vrabelj, H. Uršič, B. Rožič, Z. Kutnjak, S. Drnovšek and B. Malič, "Influence of the microstructure of $0.9Pb(Mg_{1/3}Nb_{2/3})O_3$-$PbTiO_3$ ceramics on the electrocaloric effect," in *Proceedings of the 50th International Conference on Microelectronics, Devices and Materials & the Workshop on Digital Electronic Systems*, Ljubljana, Slovenia: MIDEM – Society for Microelectronics, Electronic Components and Materials, 2014.

L. Fulanović, M. Vrabelj, S. Drnovšek, H. Uršič, D. Kuščer, K. Makarovič, Z. Kutnjak, V. Bobnar, and B. Malič, "Characterization of $0.9Pb(Mg_{1/3}Nb_{2/3})O_3$-$0.1PbTiO_3$ electrocaloric elements prepared by tape casting," in *Proceedings of the 50th International Conference on Microelectronics, Devices and Materials & the Workshop on Digital Electronic Systems*, Bled, Slovenia: MIDEM – Society for Microelectronics, Electronic Components and Materials, 2015.

Published Scientific Conference Contribution Abstracts – Invited Talks

B. Malič, H. Uršič, J. Koruza, M. Vrabelj, B. Rožič and Z. Kutnjak, "Processing and microstructure of lead-based and lead-free complex perovskites in bulk, thick and thin film form for electrocaloric applications," in *European Conference on Materials and Technologies for Sustainable Growth*, Bled, Slovenia: University of Nova Gorica, 2013.

Z. Kutnjak, U. Plaznik, A. Kitanovski, H. Uršič, M. Vrabelj, B. Malič and B. Rožič, "Relaxor ferroelectric ceramics as a working body for an electrocaloric cooling devices," in *Electronic Materials and Applications 2016*, Orlando, Florida: The American Ceramic Society, 2016.

U. Plaznik, B. Rožič, A. Kitanovski, H. Uršič, M. Vrabelj, B. Malič and Z Kutnjak, "Bulk relaxor ferroelectric ceramics as working elements in an electrocaloric cooling device," in *Energy Materials Nanotechnology: EMN Meeting on Ceramics*, Hong Kong, China, 2016.

Published Scientific Conference Contribution Abstracts

B. Rožič, Z. Kutnjak, G. Cordoyiannis, M. Trček, H. Uršič, J. Koruza, M. Vrabelj, B. Malič, R. Pirc, and S. G. and Lu, Q. M. Zhang "New cooling technologies based on the electrocalorics," in *International Ultrasonic Symposium (IUS), Joint IEEE-International Symposium on the Applications of Ferroelectrics (ISAF) and Piezoresponse Force Microscopy and Nanoscale Phenomena in Polar Materials (PFM), Joint International Frequency Control Symposium (IFCS), and European Frequency and Time Forum (EFTF)*, Prague, Czech Republic: 2013 Joint UFFC, EFTF and PFM Symposium, 2013.

M. Vrabelj, H. Uršič, B. Rožič, Z. Kutnjak and B. Malič, "Study of the electrocaloric properties of $Pb(Mg_{1/3}Nb_{2/3})O_3$-$PbTiO_3$," in *7th Young researchers' Day*, Ljubljana, Slovenia: Jožef Stefan Institute, 2013.

M. Vrabelj, H. Uršič, B. Rožič, Z. Kutnjak, S. Drnovšek and B. Malič, "Multifunctional 0.65PMN-0.35PT/Pt thick-film actuators," in *Workshop of all Working Groups: "Advances in Ferroelectric and Multiferroics" of the MP0904 COST Action: Single- and Multiphase Ferroics and Multiferroics with Restricted Geometries*, Prague, Czech Republic: Academy of Sciences of the Czech Republic, 2013.

B. Malič, M. Vrabelj, H. Uršič, J. Koruza, B. Rožič, and Z. Kutnjak, "Electrocaloric effect in lead-free relaxors: an environment-friendly alternative to lead-based counterparts?" in: *4th Edition of Electroceramics Conference*, Bucharest, Romania: National institute of Materials Physics, 2014.

M. Vrabelj, H. Uršič, B. Rožič, S. Drnovšek, Z. Kutnjak and B. Malič, "Electrocaloric properties of $0.9Pb(Mg_{1/3}Nb_{2/3})O_3$-$0.1PbTiO_3$ ceramics with different grain sizes," in *4th Edition of Electroceramics Conference*, Bucharest, Romania: National institute of Materials Physics, 2014.

M. Vrabelj, H. Uršič, B. Rožič, S. Drnovšek, Z. Kutnjak, N. Horchidan, M. V. Pop, L. Mitoseriu and B. Malič, "Dielectric and electrocaloric properties of $(100\text{-}x)Pb(Mg_{1/3}Nb_{2/3})O_3$-$xPbTiO_3$ ceramics," in *4th Edition of Electroceramics Conference*, Bucharest, Romania: National institute of Materials Physics, 2014.

M. Vrabelj, H. Uršič, S. Drnovšek, N. Horchidan, M. V. Pop, L. Mitoseriu and B. Malič, "Dielectric characterization of $(100\text{-}x)Pb(Mg_{1/3}Nb_{2/3})O_3$-$xPbTiO_3$ ceramics," in *COST MP0904 Single- and Multiphase Ferroics and multiferroics with restricted geometries (SIMUFER): Closing conference and final management committee meeting*, Genoa, Italy: Institute for Energetics and Interphases, 2014.

M. Vrabelj, H. Uršič, S. Drnovšek, N. Horchidan, M. V. Pop, L. Mitoseriu and B. Malič, "Dielectric properties of $(100\text{-}x)Pb(Mg_{1/3}Nb_{2/3})O_3$-$xPbTiO_3$," in *8th Young Researcher's Day*, Ljubljana, Slovenia: Jožef Stefan Institute, 2014.

B. Malič, M. Vrabelj, L. Fulanović, H. Uršič, S. Drnovšek, A. Benčan, B. Rožič, V. Bobnar and Z. Kutnjak, "Relation between the microstructure and the electrocaloric effect of relaxor ferroelectric $Pb(Mg_{1/3}Nb_{2/3})O_3$-$PbTiO_3$ ceramics," in *IEE International Symposium on Applications of Ferroelectric (ISAF), International Symposium on Integrated Functionalities (ISIF), and Piezoresponce Force Microscopy (PMP)*, Singapore: 2015 joint ISAF-ISIF-PFM conference, 2015.

M. Vrabelj, H. Uršič, Z. Kutnjak, B. Rožič, S. Drnovšek, L. Fulanović and B. Malič, "Electrocaloric properties of $0.9Pb(Mg_{1/3}Nb_{2/3})O_3$-$0.1PbTiO_3$ bulk ceramics," in *9th Young Researcher's Day*, Ljubljana, Slovenia: Jožef Stefan Institute, 2014.

L. Fulanović, H. Uršič, M. Vrabelj, Z. Kutnjak, B. Rožič, S. Drnovšek and B. Malič, "Effect of the grain size on the electrocaloric properties of $0.7Pb(Mg_{1/3}Nb_{2/3})O_3$-$0.3PbTiO_3$ bulk ceramics," in *9th Young Researcher's Day*, Ljubljana, Slovenia: Jožef Stefan Institute, 2014.

A. Bradeško, M. Vrabelj, M. Santo-Zarnik, Z. Kutnjak, B. Malič and T. Rojac, "Design of a stacked $(1\text{-}x)Pb(Mg_{1/3}Nb_{2/3})O_3$-$xPbTiO_3$ electrocaloric cooler," in *50th International Conference on Microelectronics, Devices and Materials & the Workshop on Digital Electronic Systems*, Bled, Slovenia: MIDEM – Society for Microelectronics, Electronic Components and Materials, 2015.

M. Vrabelj, H. Uršič, Z. Kutnjak, S. Drnovšek, L. Fulanović and B. Malič, "Influence of Mn-addition on electrocaloric properties of $0.9Pb(Mg_{1/3}Nb_{2/3})O_3$-$0.1PbTiO_3$ bulk

ceramics," in *13th International Symposium on Electric and Magnetic Fields*, Porto, Portugal: EMF 2015, 2015.

M. Vrabelj H. Uršič, B. Rožič, Z. Kutnjak, S. Drnovšek and B. Malič, "Influence of Mn-doping on electrocaloric properties of $0.9Pb(Mg_{1/3}Nb_{2/3})O_3$-$0.1PbTiO_3$ ceramics," in *Piezo 2015: Electroceramics for End-Users VIII*, Maribor, Slovenia: Piezo 2015, 2015.

L. Fulanović, H. Uršič, M. Vrabelj, Z. Kutnjak, B. Rožič, S. Drnovšek and B. Malič, "Influence of the microstructure on the electrocaloric properties of $0.7Pb(Mg_{1/3}Nb_{2/3})O_3$-$0.3PbTiO_3$ bulk ceramics," in *Piezo 2015: Electroceramics for End-Users VIII*, Maribor, Slovenia: Piezo 2015, 2015.

M. Vrabelj, H. Uršič, Z. Kutnjak, B. Rožič, S. Drnovšek, A. Benčan, V. Bobnar, L. Fulanović and B. Malič, "Electrocaloric effect in $0.9Pb(Mg_{1/3}Nb_{2/3})O_3$-$0.1PbTiO_3$ bulk ceramics with grain sizes in micron range," in *23th International Conference on Materials and Technology*, Portorož, Slovenia: Inštitut za kovinske material in tehnologije, 2015.

L. Fulanović, M. Vrabelj, S. Drnovšek, H. Uršič, D. Kuščer, K. Makarovič, Z. Kutnjak, V. Bobnar and B. Malič, " Characterization of $0.9Pb(Mg_{1/3}Nb_{2/3})O_3$-$0.1PbTiO_3$ electrocaloric multilayered structures prepared by tape casting," in *11th Students' Meeting and Application of Ceramics and ESR Workshop COST IC1208*, Novi Sad, Serbia: Faculty of Technology, University of Novi Sad, 2015.

Z. Kutnjak, U. Plaznik, A. Kitanovski, B. Rožič, B. Malič, H. Uršič, M. Vrabelj and Q. M. Zhang, "Relaxor ceramics for new dielectric cooling technology," in *Technical meeting and exhibition: MS & T15, Materials Science & Technology 2015*, Columbus, USA: The American Ceramic Society, 2015.

Invited Lecture at Foreign University

M. Vrabelj, H. Uršič, Z. Kutnjak, B. Rožič, S. Drnovšek, and B. Malič, "Processing, dielectric and electrocaloric characterization of $0.7Pb(Mg_{1/3}Nb_{2/3})O_3$-$0.3PbTiO_3$ ceramics," Iasi, Romania: Alexandru Ioan Cuza, University of Iasi, 2013.

Biography

I was born on the 2nd of July 1988 in Maribor. After finishing the Gymnasium in Maribor in 2007 I decided to enrol to the Faculty of chemistry and chemical engineering at the University of Maribor. In 2008 I started receiving the "Jožef Stefan" Institute scholarship and participated as student help in different projects at the Electronic Ceramics Department – K5 of the Institute. I graduated in July 2012 with the diploma thesis entitled "Preparation and characterization of glass-ceramics composite for application in LTCC technology", which was also carried out at the Electronic Ceramics Department, under the supervision of Prof. Dr. Miha Drofenik and Prof. Dr. Marija Kosec. In October 2012 I started to work as a Young researcher at the ″Jožef Stefan″ Institute and got enrolled to the Nanosciences and Nanotechnologies postgraduate programme at the Jožef Stefan International Postgraduate School. My work at the Institute was mainly related to the synthesis, sintering and dielectric and electrocaloric characterization of lead based ferroelectric ceramics.

Attendance to workshops:
- Characterization of the materials, Centre of Excellence NAMASTE, Hotel Rogla, Rogla, Slovenia, 7.-8.11.2011.
- Akademsko podjetništvo, Center za prenos tehnologij in inovacij, Institut Jožef Stefan, Ljubljana, Slovenija, 6.12.2012.
- Characterization of materials, Centre of Excellence NAMASTE, Jožef Stefan Institute, Ljubljana, Slovenia, 28.-29.11.2013.
- Fundamentals of vacuum techniques, Slovenian Society for Vacuum Technique, Jožef Stefan Institute, Ljubljana, Slovenia, 12.-13.1.2015.
- High temperature piezoelectrics: Materials and measurement workshop, METCO, Hotel Bellevue, Maribor, Slovenia, 25.1.2015.
- EDS/WDXS X-ray microanalysis, European Microbeam Analysis Society, Jožef Stefan Institute, Ljubljana, Slovenia, 3.5.2015.